# Theory of quantum transport at the molecular scale

# Mohammed Eid Alshammari Ph.D. Thesis in Physics

Department of Physics, Lancaster University, UK



This Thesis is submitted in partial fulfilment of the requirements for the degree of Doctor of Philosophy

2025

**Declaration** 

I hereby declare that the thesis is my own work and effort and that it has not previously been

presented in substantially the same form for a higher degree elsewhere. Other sources of

information have been used and recognised. This thesis documents work carried at Lancaster

University, UK, between April 2021 and January 2025, under the supervision of Prof. Colin

J. Lambert and Songjun Hou, supported by the Ministry of Education Saudi Arabia and

Aljouf University, KSA.

Mohammed Alshammari

January 2025

2

# Acknowledgement

My great thanks to ALLAH for his mercy and blessing. I could not have achieved what I have done without ALLAH.

I would like to thank Prof. Colin John Lambert for his excellent supervision and advice. This thesis could never have been done without his guidance and support. Additionally, I would like to thank Dr. Songjun Hou for his focused time, guidance, and helpful comments. Without him, none of this work would have been completed. I would like to thank my sponsor, the Ministry of Education-KSA, and my university in Saudi Arabia, Aljouf University, for providing me with this fantastic chance to pursue a Ph.D. in the United Kingdom. I would like to thank the collaborating experimental groups. I would like to thank everybody in Colin's group, including colleagues and friends. would like to thank my family for their constant care, love, and support: my mother, sister and brothers. I also express my deepest gratitude to my supportive wife and my son Malek for giving me courage and hope throughout my study.

# **Abstract**

Molecular electronics is a valuable tool for studying nanoscale thermoelectricity and discover ing new organic thermoelectric materials that are both low-cost and environmentally friendly. This thesis describes the theoretical methods used to support this procedure, beginning with chapters 2 and 3, respectively. I have described the essential equations and methodologies that drive my work, such as the Schrodinger equation, density functional theory (DFT), and the SIESTA programs, which is in charge of implementing DFT and solving the underlying equations. In addition, I explain the single particle transport theory, which is based on the Hamiltonian and Green's functions, and provide some examples of how it might be applied.

Chapter 4. Therefore, I investigated the transport characteristics of a HATNA series of single-molecule junctions, which includes molecules that, upon reduction by hydrogen, change between high and low conductance states, at least in the SAMs. This dynamic molecular switch can supply all basic logic gates due to its time-domain and voltage-dependent plasticity, which mimics synaptic behaviour and Pavlovian learning.

Chapter 5. This chapter covers the transport features of stable organic radicals for electrical devices, which are caused by their half-filled orbitals approaching Fermi energy. Also, observe the systematic changes that occur when the hydrogen is removed from the OH groups to generate radicals, and how this affects electrical conductivity.

# **Table of Contents**

Acknowledgment	3
Abstract	4
List of Figures	8
List of Tables.	11
List of abbreviations	12
Chapter 1	13
1.1 Thermopower and Molecular Electronics	13
1.2 Magic ratio theory	16
1.3 Thesis Outline	24
1.4 Bibliography	25
Chapter 2	29
2.1 Density Functional Theory	29
2.2 introduction.	29
2.3 The Variational Principle and Schrödinger Equation	30
2.4 The Hohenberg-Kohn Theorems	34
2.5 Kohn-Sham Method and Self-Consistent Field SFC	36
2.6. The Exchange-Correlation Potential	41
2.7. Local Density Approximation (LDA)	41
2.8. Generalized Gradient Approximation (GGA)	
2.9. SIESTA	45
2.10. Bibliography	46
Chapter 3	51

3.1 Single particle transport theory
3.2 Introduction51
3.3 The Landauer Formula
3.4 Thermoelectric Coefficients
3.5 Theory of electron transport60
3.6 Scattering Theory62
3.6.1 One dimensional (1-D) linear crystalline lattice
3.6.2 Semi-infinite one-dimensional lattice
3.6.3 Scattered in one dimension (1-D)
3.6.4 One-dimensional (1-D) Scattering Using Green's Functions
3.7 Bibliography
Chapter 4
Exploring Quantum Interference in Hexaazatrinaphthylene (HATNA) Molecules78
4.1 Motivation
4.2 Introduction
4.3. Studied Molecules80
4.4. Transmission coefficient T(E)
4.5. Frontier orbitals
4.6. DFT calculations82
4.7. Conclusions
4.8. Bibliography94

Chapter 599
Single-Molecule Conductance Enhancement in Stable Diradical Molecules99
5.1 Introduction
5.2 Studied molecules
5.3 Results and discussion
5.4 Conclusion
5.6. Bibliography122
Chapter 6
6.1 Conclusion
6.2 Future work
6.3. Bibliography

# **List of Figures**

<b>Figure 1.1</b> shows a simple bipartite lattice, such as benzene, together with the size of its magic number. (1,2) : first connectivity; (1,4) the second connectivity
Figure 1.2: Representation of the researched Anthanthrene core. There are tw connectivities
for 1: (1,5'-Red) and 2: (2',7'-Black)
Figure 1.3 shows a representation of the analysed anthracene core. Two connectivities:
(2', 6) (black), and (3, 7') (red)21
Figure 2.1: a schematic illustration of the self-consistent DFT cycle
<b>Figure 3.1</b> : A contact-linked mesoscopic scatterer. Where $\mu_L$ and $\mu_R$ represent the chemical potential in the left and right lead, respectively
Figure 3.2 shows a representation of the transport mechanism. It shows the combination of
mathematical and physical structure. This mechanism has two categories of probability, R
and T61
Figure 3.3: A tight-binding model of a (1-D) periodic lattice with energy sites and hopping
elements is used to label our atoms
Figure 3.4. represents the retarded Green's function. This includes an infinite lattice in a
single dimension. By exciting the point at $z = z'$ , the wave propagates in both the left and
right directions65
Figure 3.5 shows a tight-binding model for a semi-infinite one-dimensional lattice. This
system consists of energy site $\varepsilon_0$ and hopping components ( $\gamma$ )
<b>Figure 3.6</b> shows a tight binding model of two semi-infinite leads with one site energy $\varepsilon_0$
and couplings $-\gamma$ , connected through a hopping element $-\alpha$ 71
<b>Figure 4.1</b> . Molecules study in chapter4: two H, four H and six H80

Figure 4.2. Schematic of energy level change after reducing by adding two H, four H
and six H82
<b>Figure 4.3</b> . (a) the geometries of 0H and 2H-1 within junction. (b) Transmission curves of 0H and 2H-1
<b>Figure 4.4</b> . Wavefunctions of 0H and 0H without and with anchors84
<b>Figure 4.5</b> . The wavefunction of 2H-1 and 2H-1 with anchors
<b>Figure 4.6</b> . (a) the geometries of 0H and 2H-2 within junction. (b) Transmission curves of 0H and 2H-2
<b>Figure 4.7</b> . The wavefunction of 2H-2 and 2H-2 with and without anchors87
<b>Figure 4.8</b> . (a) the geometries of 0H and 4H-1 within junction. (b) Transmission curves of 0H and 4H-1
<b>Figure 4.9</b> . Wavefunctions of 4H-1 and 4H-1 with anchors
Figure 4.10. (a) the geometries of 0H and 4H-2 within junction. (b) Transmission curves of
0H and 4H-289
<b>Figure 4.11</b> . Wavefunctions of 4H-2 and 4H-2 without and with anchors90
<b>Figure 4.12</b> . (a) the geometries of 0H and 6H within junction. (b) Transmission curves of 0H and 6H
<b>Figure 4.13</b> . Wavefunctions of 6H without and with anchors91
Figure 5.1: Studied Diradical molecules and their corresponding neutral molecules. (CQI-H-
neutral-CQI-H-singlet-CQI-H-triplet)
Figure 5.2: Studied Diradical molecules and their corresponding neutral molecules. (CQI-L-
radical-CQI-L1-radical-CQI-L-singlet-CQI-L-triplet)101
Figure 5.3: Schematic shows two spin states for diradical molecules
Figure 5.4: (a) the geometries of CQI-H-radical and CQI-H-singlet within junction. (b)their
transmission curves
Figure 5.5: CQI-H-radical and CQI-H-singlet room temperature conductance for stable
radical10

Figure 5.6: (a) the geometries of CQI-H-radical and CQI-H-triplet within junction. (b) their
transmission curves
Figure 5.7: CQI-H-radical and CQI-H-triplet room temperature conductance for stable
radical
<b>Figure 5.8</b> : (a) the spin density for CQI-H-singlet within junction. (b) the spin density for CQI-H-triplet within junction
Figure 5.9: Frontier molecular orbitals of CQI-H-radical studied molecule with its
eigenvalues obtained from DFT, where red represents positive and blue indicates negative
regions of the wave functions
<b>Figure 5.10</b> : Frontier molecular orbitals of CQI-H-singlet studied molecule with its eigenvalues
<b>Figure 5.11</b> : Frontier molecular orbitals of CQI-H-triplet studied molecule with its eigenvalues
<b>Figure 5.12</b> :(a) the geometries of CQI-L-radical and CQI-L1-radical within junction. (b) their transmission curves
Figure 5.13: CQI-L-radical and CQI-L1-radical room temperature conductance for stable
radical112
<b>Figure 5.14</b> :(a) the geometries of CQI-L-radical and CQI-L-singlet within junction. (b) their transmission curves
Figure 5.15: CQI-L-radical and CQI-L-singlet room temperature conductance for stable
radical
<b>Figure 5.16:(</b> a) the geometries of CQI-L-radical and CQI-L-triplet within junction. (b) their transmission curves
Figure 5.17: CQI-L-radical and CQI-L-triplet room temperature conductance for stable
radical116
Figure 5.18: Frontier molecular orbitals of CQI-L-radical studied molecule with its
eigenvalues
Figure 5.19: Frontier molecular orbitals of CQI-L1-radical studied molecule with its

<b>Figure 5.20</b> : Frontier molecular orbitals of CQI-L-singlet studied molecule with its eigenvalues
<b>Figure 5.21</b> : Frontier molecular orbitals of CQI-L-triplet studied molecule with its eigenvalues
List of Tables
Table 1.1: Magic numbers for the benzene ring
Table 1.2: connectivity table
Table 1.3 shows the magic numbers for the Anthanthrene core
Table 1.4: The connectivity table $C_{ij}$ for the anthracene core $(C_{10}H_8)$ 22
Table 1.5: The magic number table $M_{ij}$ for the anthracene core $(C_{10}H_8)$ 22
Table 1.6 shows the magic ratio from the earlier Anthracene study23
Table 4.1. HOMO LUMO gaps for the molecules mentioned before92

## List of abbreviations

ME Molecular electronics

STM Scanning Tunnelling Microscopy

MCBJ Mechanically Controllable Break-Junction

QI Quantum Interference

CQI Constructive Quantum Interference

DQI Destructive Quantum Interference

**HOMO Highest Occupied Molecular Orbital** 

LUMO Lowest Unoccupied Molecular Orbital

**DFT Density Functional Theory** 

SIESTA Spanish Initiative for Electronic Simulations with Thousands of Atoms

LDA Local Density Approximation

GGA Generalized Gradient Approximation

T(E) Transmission coefficient

S Seebeck Coefficient

SAM Self-Assembled Monolayer

LCAOB Linear Combination of Atomic Orbital Basis

STM-BJ Scanning Tunnelling Microscopy Break Junctions

MRR Magic Ratio Rule

DOS Density of States

DZ Double-ξ basis set

DZP Double- ξ polarized basis set

HATNA Hexaazatrinaphthylene

SOMO singly occupied molecular orbital

SUMO singly unoccupied molecular orbital

# Chapter 1

#### 1.1 Thermopower and Molecular Electronics

Molecular electronics is the study of molecular building blocks used to create electrical components or devices [1]. These electronic elements, such as self-assembled monolayer (SAM) [2] and single-molecule [3] junctions, have the potential to deliver: logic gates [4], sensors [5,6], memory [7], and thermoelectric energy with ultralow power requirements and a device footprint of less than 10nm. They are also interesting a testbeds for room-temperature quantum features on a molecular scale, such as quantum interference [8] and thermoelectricity [9, 10]. Aviram and Ratner suggested the first molecular rectifier back in 1974 [11]. Since then a large number of molecules have been studied by changing their chemical structure, some of which function as fundamental electrical elementary devices, such as rectifiers [12], conducting wires [13-14], and negative differential resistance devices [15]. Molecular electronics faces crucial difficulties, such wiring molecules to electrodes using specific intermolecular interactions to create molecular devices. As a result, a complete understanding of electron transport between nearby molecules is required.

This thesis will primarily use theoretical and experimental methods to investigate electrode/molecule/electrode systems. These systems can be experimentally evaluated using two types of equipment: scanning tunnelling microscopy break junctions (STM-BJ) [16] and mechanically controllable break junctions (MCBJ) [17]. Such techniques have been utilised and improved to contact single molecules, graphene-based junctions [18], and silicone-based junctions [19]. On the other hand, structural problems in 2D hexagonal materials, as predicted several years ago [20], indicate that their application as electrodes is still in its infancy. For some time now, gold break junctions have been the preferred technique of contact. Because

of these limits, many methods of controlling electron transport have been created, including mechanical gating [21] and electrochemical gating [22].

Single-molecule electronic devices have many problems, which are summarised as follows:

- 1- The molecules used in the study had a length of about 1-2 nm. Furthermore, electrodes separated by 1-2 nm, which are usually made of noble metals, are beyond the capabilities of traditional top-down lithographic processes.
- 2- The molecule's small dimensions are investigated, as direct manipulation of the molecule in the nanogap is usually impossible. To position the molecule between electrodes, a chemical contact between the molecule and the electrode is required.
- 3- Because electrodes are significantly larger than molecules, it is difficult to place only one molecule in each functional device.

In addition to these three issues, there are several other key challenges, such as device stability, homogeneity, yield, and scalability.

Additionally, there has been an important improvement in our knowledge of the thermoelectrical characteristics of single-molecule junctions [23], partly due to the observation of high Seebeck coefficient S of order 161μVK<sup>-1</sup>) for PEDOT: PSS organic films [24]. The sign of the S in fullerenes and nanotubes has recently been discovered to vary due to pressure, strain, and intermolecular interactions [25]. Many of the quantum interaction effects discovered and expected in single-molecule junctions are now being scaled up to self-assembled monolayers (SAM) [26–27], ending in the development of novel thin-film materials with room-temperature quantum effects affecting transport characteristics. As a result, these achievements suggest that the area of single-molecule electronics has a bright future in generating novel functional materials. As examples, references [58-59] provide recent investigations into the Seebeck coefficient S of anthracene molecules.

The Seebeck coefficient S for anthracene molecules (with 2SMe anchor groups) and connectivities 9,10, and 1,5 were negative with values -20 and -33.0  $\frac{\mu V}{K}$ , respectively. This group measured S for the same molecule, but with different anchors (ie with 2SAc anchor groups), with the same connectivities and obtained a positive S + 12.5 and  $+16.3 \frac{\mu V}{K}$ , respectively [26-27].

SAM is a significant part of molecular-scale electronics. Currently, there are three major global designs for generating ensemble molecular junctions for large-area electrical measurements: First, metal leads can be formed directly using electron beam/thermal evaporation or electrochemical deposition. Secondly, electrically conducting polymers/nanomaterials can be used as electrodes and thirdly liquid metals can be used as electrode materials.

To create ensemble molecular connections utilising several cutting-edge techniques, there are multiple techniques available, including liquid metal contact, lift-and-float, nanopore and nanowell, on-wire lithography, nanoimprint lithography, crossbar or crosswire, self-aligned lithography, buffer interlayer-based junctions, and on-edge molecular junctions.

In this section, we try to show a simple method for calculating the value of electrical conductance that results from constructive quantum interference in molecules. When a single molecule is attached to metallic leads, electrons passing through the molecule from one electrode to the other can remain phase-coherent even at room temperature [28, 29]. As a result, there has been a great deal of discussion of quantum interference (QI). This QI can be used to determining the electrical conductance of individual molecules [30-31]. Thus, both experiment and theory have focused on describing the conditions for the formation of two distinct examples of QI, namely constructive or destructive interference. Constructive quantum interference (CQI) happens when the delocalized energy level of the molecule coincides. In contrast, destructive quantum interference (DQI) happens when it coincides

with the energy of a bound state on a pendant moiety [32, 33]. Because the electrode Fermi energy is often located in the HOMO and LUMO (H-L) gap, molecules inside a junction rarely show CQI resonances unless the energy levels are controlled by electrostatic, electrochemical, or mechanical gating. As a result, research have considered the two conditions CQI and DQI as they are specified or placed at the core of the H-L gap [31,34-37].

## 1.2 Magic ratio theory

One method of describing the connectivity dependence of QI is to utilise a magic ratio rule (MRR) based on 'magic number' tables. When one electrode is connected to site i and the other to site i' of the same molecule, the molecule is assigned the "magic integer"  $M_{ii}$ . Here I shall give a comprehensive introduction to this theory, which can help to guide the synthesis of new molecules. Magic integers (MIs) can represent the complexity of interference patterns produced by electrons at the centre of the HOMO-LUMO gap. Magic ratio rules (MRR) can also be used to calculate the conductance ratio. MRR says that "the ratio of conductances of two molecules is equal to the squares of the ratios of their magic integers." When analysing the conductances of the aromatic core but using various contacts, the MI's signals are irrelevant. The MRR can be regarded as an exact formula for conductance ratios of tightbinding representations of molecules; this is valid in the weak coupling limit, when the Fermi energy is placed between the H-L gap. In this situation, the magnitude of the H-L gap has no effect, and it is unaffected by contact asymmetries between the leads and the molecule. The MRR is particularly simple for a tight-binding, bipartite lattice of similar sites with identical couplings, when the  $E_F$  is at the centre of the H-L gap and the number of odd sites matches the number of even sites. In this situation, a simple tight-binding Hamiltonian system uses -1 for nearest neighbour couplings and zero for on-site energies.

In general, the mid-gap concept describes how the transmission coefficient at the gap centre is calculated when the energy of electrons travelling through the core molecule coincides

with the middle of the HOMO-LUMO gap. This indicates how important and valuable it is to first consider connectivity when fabricating single-molecule junctions with good electrical characteristics. In the case of binding molecules to electrodes, high conductivity is preferred. However, a low conductance is necessary to prevent leakage currents when attached to an electrostatic gate. The MRR shows that connectivities with both high and low MIs can be generated using the same molecule.

The analysis of the complete magic number table for a molecular core helps us to figure out the impact of connection on electrical conductance. As a result, the electrical conductance is proportional to the item in the magic number table denoted by *i*. The following is the most basic application of the magic ratio theory, based on the work Magic Ratios for Connectivities-Driven Electrical Conductance of Graphene-like Molecule by Y. Geng and others (9 authors) [38].

Example 1: We want to use the magic ratio theory on a bipartite lattice (benzene ring) with six atoms [38]. To apply this concept, two connectivities must be selected in the same molecule, such as (1,4) and (1,2) in Figure 1.1.

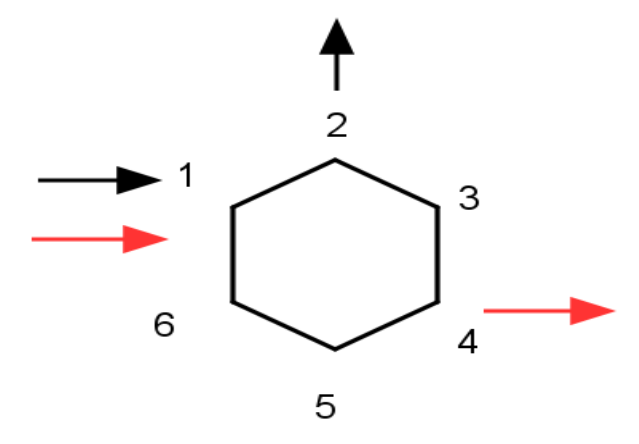


Figure 1.1 shows a simple bipartite lattice, such as benzene, together with the size of its magic number. (1,2): first connectivity; (1,4) the second connectivity

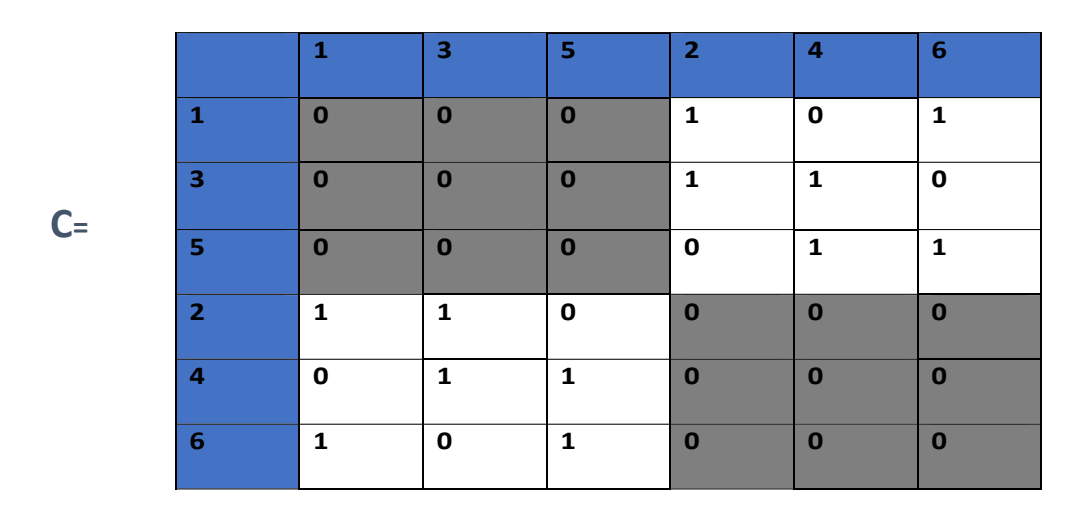


Table 1.1: Magic numbers for the benzene ring.

		1	3	5	2	4	6
	1	0	0	0	1	-1	1
M=	3	0	0	0	1	1	-1
	5	0	0	0	-1	1	1
	2	1	1	-1	0	0	0
	4	-1	1	1	0	0	0
	6	1	-1	1	0	0	0

Table 1.2: connectivity table

Table 1.2 shows that the electrical conductance is proportional to  $(M_{ij})^2$ , where i and j represent the entrance and exit points.

In our example, i and j are (1,2) for the first connectivity and (1,3) for the second connectivity. As a result, the magic ratio rule (MMR) for the two connectivities (1,2) and (1,4) predicts that the ratio of the conductance  $\frac{G_{1,2}}{G_{1,3}}$  corresponding to the two connectivities can be calculated as:

MRR = 
$$\frac{G_{1,2}}{G_{1,3}} = \frac{(1)^2}{(0)^2} = \infty$$
. In practice, this means that the MRR predicts that  $G_{1,2} \gg G_{1,3}$ .

The following example compares the theory and experiment with the magic ratio theory described in this publication [38]. Here, an anthanthrene core has been chosen for investigation. As shown in Figure 1.2, the two connectivities are (1,5') and (7,2') in this example.

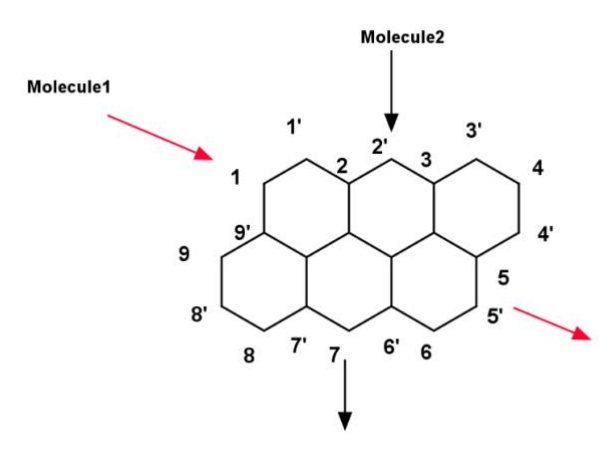


Figure 1.2: Representation of the researched Anthanthrene core. There are two connectivities for 1: (1,5'-Red) and 2: (2',7'-Black).

		1′	2'	3'	4'	5'	6'	7'	8′	9′	10′	11'
	1	-9	7	-4	4	-1	1	-1	1	-1	2	-3
	2	-1	-7	4	-4	1	-1	1	-1	1	-2	3
M=	3	1	-3	-4	4	-1	1	-1	1	-1	2	-3
	4	-1	3	-6	-4	1	-1	1	-1	1	-2	3
	5	1	-3	6	-6	-1	1	-1	1	-1	2	-3
	7	3	-9	8	-8	7	-7	-3	3	-3	6	1
	8	-6	8	-6	6	-4	4	-4	-6	6	-2	-2
	9	6	-8	6	-6	4	-4	4	-4	-6	2	2
	10	3	1	-2	2	-3	3	-3	3	-3	-4	1
	11	-2	6	-2	2	2	-2	2	-2	2	-4	4

Table 1.3 shows the magic numbers for the anthanthrene core.

From the above table, the MRR predicts the following conductance ratio corresponding to the two connectivities

MRR = 
$$\frac{G_{7,2'}}{G_{1.5'}} = \frac{(-9)^2}{(-1)^2} = 81$$
, (Theoretical value)

Experimentally, it was found that [38]

$$\frac{G_{7,2'}}{G_{1.5'}} = \frac{10^{-4.8}}{10^{-6.7}} = 79$$

Which is in remarkable agreement with the MRR prediction.

# Magic ratio principles for the symmetric anthracene molecule.

In the following example, I discuss the magic ratio concept for an anthracene core, which were measured in [26-27]. The same molecule is used, with two different connectivities. denoted (2,6) and (3',7), as shown in Figure 1.3.

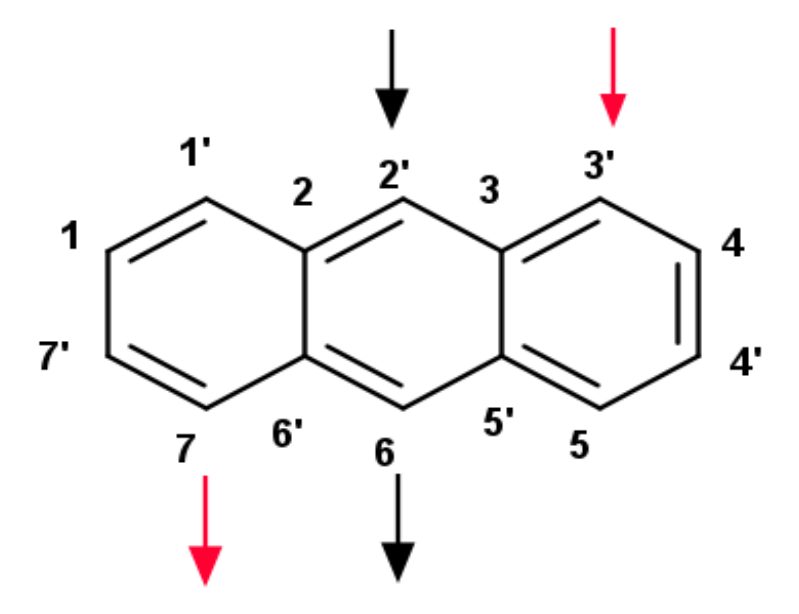


Figure 1.3 shows a representation of the analysed anthracene core. Two connectivities: (2′, 6) (black), and (3, 7′) (red).

Three fused benzene rings make up the polycyclic aromatic hydrocarbon known as the anthracene core, which is seen in Figure 1.3. Two categories of connectivities within the core can be seen in the figure; one is indicated in red and the other in black. Although the actual picture is not shown here, it usually shows the locations and paths of bonds in the chemical system, emphasising the distinct patterns of connectedness.

	1	2	3	4	5	6	7
1′	1	1	0	0	0	0	0
2'	0	1	1	0	0	0	0
3'	0	0	1	1	0	0	0
4'	0	0	0	1	1	0	0
5′	0	0	1	0	1	1	0
6′	0	1	0	0	0	1	1
7′	0	0	0	0	0	0	1

Table 1.4: The connectivity table  $C_{ij}$  for the anthracene core  $(C_{10}H_8)$ .

The connectivity pattern of the anthracene core appears in Table 1.4, indicating which atoms are connected to one another. In order to help understand the molecular structure and the connections between the atoms in the anthracene, the table uses '1' to denote a bond and '0' for no link.

7 1 2 3 4 5 6 1' -3 2 1 -1 -1 1 -1 1 2' -1 -2 -1 1 -1 1 3′ 1 -2 -1 1 -1 1 -1 M= 4' -1 2 -3 -1 1 -1 1 **5**′ -2 3 1 -3 -1 1 -1 6' -2 4 -2 2 -2 -2 2 7′ 3 1 -2 -1 1 -1 -3

Table 1.5: The magic number table  $M_{ij}$  for the anthracene core ( $C_{10}H_8$ ).

In this case, the MRR predicts the following conductance ratio

MRR = 
$$\frac{G_{2',6}}{G_{3',7}} = \frac{(4)^2}{(1)^2} = 16.$$

For comparison with experiment, the table below shows experimental results for two studies of anthracene, with two different anchor groups

Anthracene	Theory (DFT) $\frac{G}{G_0}$	DFT Theory ratios	Experiment $\frac{G}{G_0}$	Experimen tal ratios	Ref
2 SMe(1, 9)	1.66e – 4	15.8	7.01e – 5	10.19	
2 SMe(1, 5)	1.05e – 5		6.88 e-6		
2 SAc (1,9)	1.59e — 4	15.9	1.28e – 4	14.22	[26,27]
2SAc (1,5)	1e – 5	10.9	9 e-6	11.22	
2 Py (1,9)	0.9e – 4	15.7			
2 Py (1,5)	0.57 e-5	10.,			

Table 1.6 shows the magic ratio from the earlier anthracene study.

#### 1.3 Thesis Outline

In this thesis, the theoretical studies introduce the electrical properties of two-terminal molecular junctions, with gold electrodes, which generate gold |molecule| gold structures. Theoretical methods include density functional theory (DFT) and tight binding models (TBMs). Thus, Chapter 2 presents theoretical concepts of DFT and the implementation used in this work, primarily via the SIESTA code. The second tool is the quantum transporter code GOLLUM. In Chapter 3, I provide solutions to Green's functions for infinite and semiinfinite 1D chains, as well as the transmission coefficient equations used as the theoretical basis for this code. The charge transport at the single-molecule level is also studied. Recently, there has been a lot of interest in using quantum interference effects to speed up charge transmission. In Chapter 4, I study the hexaazatrinaphthylene (HATNA) molecules, which has been shown to have memristive properties. However, the mechanism involved is unknown and therefore to elucidate the origin of memristive switching events, I studied the transport properties of a series of HATNA molecules. In Chapter 5, I study the influence of quantum interference, which includes both constructive and destructive quantum interference, providing another dimension to manipulating electron transport through molecules. As recognised by the MRR, depending on the connection, molecules exhibiting CQI can have different conductance inside the same molecule. This chapter discusses two different CQIs based on thiophene dimers.

## 1.4 Bibliography

- [1] Scheer, E., 'Visions for a molecular future', *Nature Nanotechnology*, vol. 2013, pp. 385–389, Jun. 2013, doi: 10.1038/nnano.2013.101.
- [2] J. C. Love, L. A. Estroff, J. K. Kriebel, R. G. Nuzzo, and G. M. Whitesides, 'Self-assembled monolayers of thiolates on metals as a form of nanotechnology', *Chem Rev*, vol. 105, no. 4, pp. 1103–1169, Apr. 2005, doi: 10.1021/cr0300789.
- [3] C. M. Finch, S. Sirichantaropass, S. W. Bailey, I. M. Grace, V. M. Garcia-Suarez, C. J. Lambert, ataraman, 'Conformation dependence of molecular conductance: chemistry versus geometry', *J. Phys. Condens. Matt.* vol. 20 022203, Dec. 2008, doi: 10.1088/0953-8984/20/02/022203
- [4] S. Sangtarash, *C. Huang*, H. Sadeghi, G. Sorohhov, J. Hauser, T. Wandlowski, and C.J. Lambert, 'Searching the Hearts of Graphene-like Molecules for Simplicity, Sensitivity, and Logic', *J Am Chem Soc*, vol. 137, no. 35, pp. 11425–11431, Sep. 2015,
- [5] H. Sadeghi *L. Algaragholy, T.Pope*, S. Bailey, D. Visontai, D. Manrique, and C.J. Lambert, 'Graphene Sculpturene Nanopores for DNA Nucleobase Sensing', *J. Phys. Chem. B*, vol. 118, no. 24, pp. 6908–6914, Jun. 2014, doi: 10.1021/jp5034917.
- [6] H. Sadeghi, S. Bailey, and C. J. Lambert, 'Silicene-based DNA nucleobase sensing', *Applied Physics Letters*, vol. 104, no. 10, p. 103104, Mar. 2014, doi: 10.1063/1.4868123.
- [7] T. Prodromakis, C. Toumazou, and L. Chua, 'Two centuries of memristors', *Nature materials*, vol. 11, pp. 478–81, May 2012, doi: 10.1038/nmat3338.
- [8] C. J. Lambert, 'Basic concepts of quantum interference and electron transport in single-molecule electronics', *Chem. Soc. Rev.*, vol. 44, no. 4, pp. 875–888, Feb. 2015, doi: 10.1039/C4CS00203B.
- [9] H. Sadeghi, S. Sangtarash, and C. J. Lambert, 'Oligoyne Molecular Junctions for Efficient Room Temperature Thermoelectric Power Generation', *Nano Lett.*, vol. 15, no. 11, pp. 7467–7472, Nov. 2015, doi: 10.1021/acs.nanolett.5b03033.
- [10] H. Sadeghi, S. Sangtarash, and C. J. Lambert, 'Enhanced Thermoelectric Efficiency of Porous Silicene Nanoribbons', *Sci Rep*, vol. 5, no. 1, p. 9514, Mar. 2015, doi: 10.1038/srep09514.
- [11] A. Aviram and M. A. Ratner, 'Molecular rectifiers', *Chemical Physics Letters*, vol. 29, no. 2, pp. 277–283, Nov. 1974, doi: 10.1016/0009-2614(74)85031-1.
- [12] A. Batra P. Darancet, Q. Cen, J.S., Meisner, J.R. Widawsky, J.B. Neaton, and L. Venkataraman., 'Tuning rectification in single-molecular diodes', *Nano Lett*, vol. 13, no. 12, pp. 6233–6237, 2013, doi: 10.1021/nl403698m.

- [13] L. Lafferentz, F. Ample, H. Yu, S. Hecht, C. Joachim, and L. Grill, 'Conductance of a Single Conjugated Polymer as a Continuous Function of Its Length', *Science*, vol. 323, no. 5918, pp. 1193–1197, Feb. 2009, doi: 10.1126/science.1168255.
- [14] W. B. Davis, W. A. Svec, M. A. Ratner, and M. R. Wasielewski, 'Molecular-wire behaviour in p-phenylenevinylene oligomers', *Nature*, vol. 396, no. 6706, pp. 60–63, Nov. 1998, doi: 10.1038/23912.
- [15] J. Chen, W. Wang, M. A. Reed, A. M. Rawlett, D. W. Price, and J. M. Tour, 'Room-temperature negative differential resistance in nanoscale molecular junctions', *Applied Physics Letters*, vol. 77, no. 8, pp. 1224–1226, Aug. 2000, doi: 10.1063/1.1289650.
- [16] C. Li, I. Pobelov, T. Wandlowski, A. Bagrets, A. Arnold, and F. Evers, 'Charge transport in single Au / alkanedithiol / Au junctions: coordination geometries and conformational degrees of freedom', *J Am Chem Soc*, vol. 130, no. 1, pp. 318–326, Jan. 2008, doi: 10.1021/ja0762386.
- [17] W. Hong, *D.Z.Marique*, *P. Moreno-Garcia*, *M. Gulcur*, *A.Mishchenko*, *C.J. Lambert and T. Wandlowski*, 'Single molecular conductance of tolanes: experimental and theoretical study on the junction evolution dependent on the anchoring group', *J Am Chem Soc*, vol. 134, no. 4, pp. 2292–2304, Feb. 2012, doi: 10.1021/ja209844r.
- [18] H. Sadeghi, S. Sangtarash, and C. J. Lambert, 'Enhancing the thermoelectric figure of merit in engineered graphene nanoribbons', *Beilstein J. Nanotechnol.*, vol. 6, no. 1, pp. 1176–1182, May 2015, doi: 10.3762/bjnano.6.119.
- [19] H. Sadeghi, S. Bailey, and C. J. Lambert, 'Silicene-based DNA nucleobase sensing', *Applied Physics Letters*, vol. 104, no. 10, p. 103104, Mar. 2014, doi: 10.1063/1.4868123.
- [20] J. Warner, 'Detailed Atomic Structure of Defects in 2D Materials: From Graphene to Transition Metal Dichalcogenides', *Microscopy and Microanalysis*, vol. 21, pp. 573–574, Aug. 2015, doi: 10.1017/S1431927615003669.
- [21] L. Rincón-García, A. K. Ismael, C. Evangeli, I. Grace, G. Rubio-Bollinger, K. Porfyrakis, and C.J. Lambert, 'Molecular design and control of fullerene-based bithermoelectric materials', *Nature Mater*, vol. 15, no. 3, pp. 289–293, Mar. 2016, doi: 10.1038/nmat4487.
- [22] Y. Li, M. Baghernejad, A. G. Qusiy, D. Zsolt Manrique, G. Zhang, J. Hamill, and C. Lambert, 'Three-State Single-Molecule Naphthalenediimide Switch: Integration of a Pendant Redox Unit for Conductance Tuning', *Angew Chem Int Ed Engl*, vol. 54, no. 46, pp. 13586–13589, Nov. 2015, doi: 10.1002/anie.201506458.
- [23] G. Yzambart, L. Rincon-Garcia, A. A. Al-Jobory, A. K. Ismael, G. Rubio-Bollinger, C. J. Lambert, and M. R. Bryce, 'Thermoelectric Properties of 2,7-Dipyridylfluorene Derivatives in Single-Molecule Junctions', *J Phys Chem C Nanomater Interfaces*, vol. 122, no. 48, pp. 27198–27204, Dec. 2018, doi: 10.1021/acs.jpcc.8b08488.
- [24] N. Massonnet, A. Carella, O. Jaudouin, P. Rannou, G. Laval, C. Celle, and J. P. Simonato 'Improvement of the Seebeck coefficient of PEDOT:PSS by chemical reduction combined with a novel method for its transfer using free-standing thin films', *J. Mater. Chem. C*, vol. 2, no. 7, pp. 1278–1283, Jan. 2014, doi: 10.1039/C3TC31674B.

- [25] L. Rincón-García, A. K. Ismael, C. Evangeli, I. Grace, G. Rubio-Bollinger, K. Porfyrakis, and C.J. Lambert, 'Molecular design and control of fullerene-based bithermoelectric materials', *Nature Mater*, vol. 15, no. 3, pp. 289–293, Mar. 2016, doi: 10.1038/nmat4487.
- [26] X. Wang, T. L. Bennett, A. Ismael, L. A. Wilkinson, J. Hamill, A. J. White, and C.J. Lambert, 'Scale-Up of Room-Temperature Constructive Quantum Interference from Single Molecules to Self-Assembled Molecular-Electronic Films', *J Am Chem Soc*, vol. 142, no. 19, pp. 8555–8560, May 2020, doi: 10.1021/jacs.9b13578.
- [27] A. Ismael, X. Wang, T. L. Bennett, L. A.Wilkinson, B. J. Robinson, N. J. Long, and C. J. Lambert, 'Tuning the thermoelectrical properties of anthracene-based self-assembled monolayers', *Chem. Sci.*, vol. 11, no. 26, pp. 6836–6841, Jul. 2020, doi: 10.1039/D0SC02193H.
- [28] G. Sedghi, V. M. Garcia-Suarez, L. J. Esdaile, H. L. Anderson, C. J. Lambert, S. Martin and R. J. Nichols, 'Long-range electron tunnelling in oligo-porphyrin molecular wires', *Nat Nanotechnol*, vol. 6, no. 8, pp. 517–523, Jul. 2011, doi: 10.1038/nnano.2011.111.
- [29] X. Zhao, C. Huang, M. Gulcur, A. S. Batsanov, M. Baghernejad, W. Hong, and T. Wandlowski, 'Oligo (aryleneethynylene)s with Terminal Pyridyl Groups: Synthesis and Length Dependence of the Tunneling-to-Hopping Transition of Single-Molecule Conductances', *Chem. Mater.*, vol. 25, no. 21, pp. 4340–4347, Nov. 2013, doi: 10.1021/cm4029484.
- [30] H. Sadeghi, J. A. Mol, C. S. Lau, G. A. D. Briggs, J. Warner, and C. J. Lambert, 'Conductance enlargement in picoscale electroburnt graphene nanojunctions', *Proceedings of the National Academy of Sciences*, vol. 112, no. 9, pp. 2658–2663, Mar. 2015, doi: 10.1073/pnas.1418632112.
- [31] G. C. Solomon, J. P. Bergfield, C. A. Stafford, and M. A. Ratner, 'When "small" terms matter: Coupled interference features in the transport properties of cross-conjugated molecules', *Beilstein J. Nanotechnol.*, vol. 2, pp. 862–871, Dec. 2011, doi: 10.3762/bjnano.2.95.
- [32] J. P. Bergfield, M. A. Solis, and C. A. Stafford, 'Giant Thermoelectric Effect from Transmission Supernodes', *ACS Nano*, vol. 4, no. 9, pp. 5314–5320, Sep. 2010, doi: 10.1021/nn100490g.
- [33] A. B. Ricks, G. C. Solomon, M. T. Colvin, A. M. Scott, K. Chen, M. A. Ratner, and M. R. Wasielewski, 'Controlling Electron Transfer in Donor–Bridge–Acceptor Molecules Using Cross-Conjugated Bridges', *J. Am. Chem. Soc.*, vol. 132, no. 43, pp. 15427–15434, Nov. 2010, doi: 10.1021/ja107420a.
- [34] D. Z. Manrique, C. Huang, M. Baghernejad, X. Zhao, O. A. Al-Owaedi, H. Sadeghi, and C. J. Lambert, 'A quantum circuit rule for interference effects in single-molecule electrical junctions', *Nat Commun*, vol. 6, no. 1, p. 6389, Mar. 2015, doi: 10.1038/ncomms7389.
- [35] T. Markussen, J. Schiötz, and K. S. Thygesen, 'Electrochemical control of quantum interference in anthraquinone-based molecular switches', *The Journal of Chemical Physics*, vol. 132, no. 22, p. 224104, Jun. 2010, doi: 10.1063/1.3451265.

- [36] H. Vazquez, R. Skouta, S. Schneebeli, M. Kamenetska, R. Breslow, L. Venkataraman, and M. S. Hybertsen, 'Probing the conductance superposition law in single-molecule circuits with parallel paths', *Nat Nanotechnol*, vol. 7, no. 10, pp. 663–667, Oct. 2012, doi: 10.1038/nnano.2012.147.
- [37] S. V. Aradhya, J. S. Meisner, M. Krikorian, S. Ahn, R. Parameswaran, M. L. Steigerwald, and L. Venkataraman, 'Dissecting contact mechanics from quantum interference in single-molecule junctions of stilbene derivatives', *Nano Lett*, vol. 12, no. 3, pp. 1643–1647, Mar. 2012, doi: 10.1021/nl2045815.
- [38] Y. Geng, S. Sangtarash, C. Huang, H. Sadeghi, Y. Fu, W. Hong, and S. X. Liu, 'Magic ratios for connectivity-driven electrical conductance of graphene-like molecules', *J. Am. Chem. Soc.*, vol. 137, no. 13, pp. 4469–4476, Apr. 2015, doi: 10.1021/jacs.5b00335.
- [39] Y. Li, M. Buerkle, G. Li, A. Rostaman H. Wang, Z. Wang, D. R. Bowder, T. Miyazaki, L. Xiang Y. Asai, G. Zhou, and N. Tao, , 'Gate controlling of quantum interference and direct observation of anti-resonances in single molecule charge transport', Nat Mater, vol. 18, no. 4, pp. 357–363, Apr. 2019, doi: 10.1038/s41563-018-0280-5.
- [40] R. Hartle, M. Butzin, O. Rubio- Pons, and M. Thoss, 'Quantum Interference and Decoherence in Single-Molecule Junctions: How Vibrations Induce Electrical Current | Phys. Rev. Lett.' Accessed:[Online]. Available: https://journals.aps.org/prl/abstract/10.1103/PhysRevLett.107.046802
- [41] X. Liu, S. Sangtarash, D. Reber, D. Zhang, H. Sadeghi, J. Shi, Z. Y. Xiao, W. Hong, C. J. Lambert, and S. X. Liu, 'Gating of Quantum Interference in Molecular Junctions by Heteroatom Substitution', *Angew Chem Int Ed Engl*, vol. 56, no. 1, pp. 173–176, Jan. 2017, doi: 10.1002/anie.201609051.
- [42] R. Miao, H. Xu, M. Skripnik, L. Cui, K. Wang, K. G. L. Pedersen, M. Leijnse, F. Pualy, K. Warnmark, E. Meyhofer, P. Reddy, and H. Linke, , 'Influence of Quantum Interference on the Thermoelectric Properties of Molecular Junctions', *Nano Lett*, vol. 18, no. 9, pp. 5666–5672, Sep. 2018, doi: 10.1021/acs.nanolett.8b02207.
- [43] R. E. Sparks, V. M. Garcia-Suarez, D. Z. Manrique, C. J. Lambert, Quantum Interference in Single Molecule Electronic Systems'. [Online]. Available: https://www.researchgate.net/publication/50292233\_Quantum\_Interference\_in\_Single\_Molecule\_Electronic\_Systems
- [44] L. Bi, K. Liang, G. Czap, H. Wang Recent progress in probing atomic and molecular quantum coherence with scanning tunneling microscopy', *ResearchGate*, May 2025, doi: 10.1016/j.progsurf.2022.100696.
- [45] S. Gunasekaran, J. E. Greenwald, and L. Venkataraman, 'Visualizing Quantum Interference in Molecular Junctions', *Nano Lett*, vol. 20, no. 4, pp. 2843–2848, Apr. 2020, doi: 10.1021/acs.nanolett.0c00605.

# Chapter 2

## 2.1 Density Functional Theory

This chapter provides an overview of the mathematical principles underlying density functional theory (DFT). Additionally, it introduces the key concepts of the DFT code SIESTA, which serves as the foundation for electronic structure calculations in this thesis. The first step in studying electronic transport is to obtain and relax the Hamiltonian structure of an isolated molecule. The isolated molecule is connected to metallic electrodes for the purpose of computing its transport parameters. A detailed explanation of the calculation of transport properties is outlined in the following Chapter.

#### 2.2 Introduction

DFT is mainly used by chemists and physicists to investigate the ground state of interacting many-particle systems such as molecules, atoms, and crystals. It is a computational quantum mechanical technique that transforms one of the non-interacting fermions in an effective field into a many-body system. Similarly, the electrical properties of many interacting particle systems can be described as a function of ground-state density [1, 2]. Walter Kohn received the Nobel Prize in Chemistry in 1998, confirming the importance of DFT. He received the award for his important contributions to the development of DFT techniques. DFT is an accurate method that has been used to numerous molecular structures. In addition, a large number of publications on pertinent literature have been published [1-6], providing comprehensive explanations of the concepts of density functional theory and its applications. Density functional theory (DFT) was first introduced by the Thomas-Fermi model in the 1920s, which outlined the basic steps for utilising wave functions to derive density functionality for total energy [1, 6-8]. The Almost forty years after Dirac, Hartree, Slater, and Fock's work was

published, additional advancements were made to the Thomas Fermi model. The Hohenberg-Kohn theorems and Kohn-Sham techniques then effectively launched the DFT foundation [1, 3, 4, 7–11]. The main objective of this chapter is to provide a brief introduction to density functional theory as well as an outline of the key mathematical equations used to solve the non-relativistic many-particles time-independent Schrödinger equation TISE. This is because the function of electron density can be used to determine the parameters of a many-electron system. This chapter will present the DFT code 'SIESTA,' which has been extensively used as a theoretical tool throughout this Ph.D. research to find a technique for structural optimization.

#### 2.3 The Variational Principle and Schrödinger Equation.

The time-independent, non-relativistic Schrödinger equation in equation 2.1, presents the non-relativistic many-particle system in a methodical way:

$$H\psi_i(\vec{r}_1, \vec{r}_2, ..., \vec{r}_N, \vec{R}_1, \vec{R}_2, ..., \vec{R}_M = E_i\psi_i(\vec{r}_1, \vec{r}_2, ..., \vec{r}_N, \vec{R}_1, \vec{R}_2, ..., \vec{R}_M$$
(2.1)

H is the Hamiltonian operator of an N-electronic system, M-nuclei is the particle interaction,  $\psi_i$  is the wave-function of the system's state, and  $E_i$  (describes the numerical value energy of the state. The Hamiltonian operator (H) is defined as follows:

$$= -\frac{\hbar^{2}}{2m_{e}} \sum_{i=1}^{N} \nabla_{i}^{2} - \frac{\hbar^{2}}{2m_{n}} \sum_{n=1}^{M} \nabla_{n}^{2} - \frac{1}{4\pi\varepsilon_{o}} \sum_{i=1}^{N} \sum_{n=1}^{M} \frac{1}{|\vec{r}_{i} - \vec{R}_{n}|} Z_{n} e^{2}$$

$$+ \frac{1}{8\pi\varepsilon_{o}} \sum_{i=1}^{N} \sum_{i\neq j}^{N} \frac{e^{2}}{|\vec{r}_{i} - \vec{r}_{j}|} + \frac{1}{8\pi\varepsilon_{o}} \sum_{n=1}^{M} \sum_{n\neq n'}^{M} \frac{Z_{n} Z_{n'} e^{2}}{|\vec{R}_{n} - \vec{R}_{n'}|}$$
(2.2)

In equation 2.2, i and j represent the N-electrons, n and  $\acute{n}$  indicate a run over the M-nuclei in the system,  $m_{\rm e}$  and  $m_n$  represent the electron and nucleus masses, respectively. Furthermore, e and  $Z_n$  indicate the electron and nuclear charge in the system, respectively, whereas  $\vec{r_i}$  and  $\vec{R_n}$  represent the electron and nuclei positions in the system, respectively. The Laplacian operator is mathematically outlined in a Cartesian coordinate  $\nabla^2$  which is given by the equation below.

$$\nabla_i^2 = \frac{\partial^2}{\partial x_i^2} + \frac{\partial^2}{\partial y_i^2} + \frac{\partial^2}{\partial z_i^2}$$

According to the image provided by Eq. (2.2), the quantity  $T_e$  denotes the kinetic energy of electrons, whereas, denotes the kinetic energy of nuclei in the system. Furthermore, the following three terms define the Hamiltonian's potential part term  $U_{en}$  indicates the appealing in the system, there is electrostatic interaction between nuclei and electrons. The repulsive parts of the potential are electron-electron ( $U_{ee}$ ) and nuclear-nuclear ( $U_{nn}$ ) [1, 3, 6, 9, 13].

The Born-Oppenheimer approximation, Since the nucleus of an atom contains 99.9% of its mass and because the nuclei in the system can be thought of as fixed in comparison to the electrons, which is also known as the clamped nuclei approximation, can be used in the analysis.

This means that the nucleus of a hydrogen atom weighs around 1800 times more than the electron. If the nuclei of the treated atoms are held stable in the given situation, the resulting kinetic energy sums to zero, indicating that they no longer contribute to the whole wavefunction. As a result of the prior assumption, the Hamiltonian expression of the electron system lowers the Hamiltonian to a distinct figure, similarly, the electronic Hamiltonian  $H_{ele}$  can be represented in a fixed nuclear representation as [1, 3, 6, 13-15]:

$$\mathbf{H}_{ele} = \underbrace{\frac{T_{e}}{2m_{e}} \sum_{i=1}^{N} \nabla_{i}^{2} - \frac{1}{4\pi\varepsilon_{o}} \sum_{i=1}^{N} \sum_{n=1}^{M} \frac{1}{|\vec{r}_{i} - \vec{R}_{n}|} Z_{n} e^{2}}_{U_{ee}} + \underbrace{\frac{U_{ee}}{1} + \frac{1}{4\pi\varepsilon_{o}} \sum_{i=1}^{N} \sum_{n=1}^{M} \frac{1}{2} \sum_{i=1}^{M} \sum_{n\neq n'}^{M} \frac{Z_{n} Z_{n'} e^{2}}{|\vec{R}_{n} - \vec{R}_{n'}|}}_{(2.3)}$$

Where  $U_{nn}$  is an obtained constant for the system.

The Schrödinger equation for 'clamped-nuclei' is represented in the above system as:

$$|\psi(\vec{r}_1, \vec{r}_2, ..., \vec{r}_N)|^2 d\vec{r}_1 d\vec{r}_2 ... d\vec{r}_N$$
 (2.6)

Because the electrons are indistinguishable, the above expression represents the probability that electrons 1, 2,..., N are found in the volume elements  $d\vec{r}_1 d\vec{r}_2 \dots d\vec{r}_N$  and this probability is unchangeable if the coordinates of any two electrons (i and j) are swapped [12]:

$$|\psi(\vec{r}_{1}, \vec{r}_{2}, \dots \vec{r}_{i}, \vec{r}_{j}, \dots, \vec{r}_{N})|^{2} = |\psi(\vec{r}_{1}, \vec{r}_{2}, \dots \vec{r}_{j}, \vec{r}_{i}, \dots, \vec{r}_{N})|^{2}$$
(2.7)

Because electrons are fermions with half-spins, the value of  $\psi$  must be anti-symmetric with regard to the interchange of spatial and spin coordinates in any pair of electrons.

$$\psi(\vec{r}_1, \vec{r}_2, \dots \vec{r}_i, \vec{r}_j, \dots, \vec{r}_N) = -\psi(\vec{r}_1, \vec{r}_2, \dots \vec{r}_i, \vec{r}_j, \dots, \vec{r}_N)$$
 (2.8)

The integral of equation 2.6 over the complete range of all variables gives one as a logical conclusion of the wave-function's probability interpretation format.

This means that the chance of finding the N-electron at any point in space must be exactly one.

$$\int ... \int |\psi(\vec{r}_1, \vec{r}_2, ..., \vec{r}_N)|^2 d\vec{r}_1 d\vec{r}_2 ... d\vec{r}_N = 1$$
 (2.9)

A normalised wave-function is one that fits the conditions of equation (2.9).

Because the Schrödinger wave-equation does not have an exact solution, many theories have been made to achieve this goal, beginning with Hartree, Hartree-Fock, and many others. A large number of these theories were founded on a significant theoretical theory known as the variational principle of the wave-function, which guides analysts on how to find answers by employing suitable trial wave-functions  $\psi_{Tri}$  [1, 2, 5, 6, 12]. The previous principle is useful in studying the ground state, however it is not very useful in studying excited states. When a system is in the state  $\psi_{Tri}$ , the expected value of energy is given by the expression:

$$\langle E_{Tri} \rangle = \frac{\int \psi_{Tri} \mathbf{H} \, \psi_{Tri}^* \, d\vec{r}}{\int \psi_{Tri} \, \psi_{Tri}^* \, d\vec{r}}$$
 (2.10)

The variational concept stated in equation 2.10 indicates that the energy computes as the expectation value of the Hamiltonian operator from any  $\psi_{Tri}$  (that is an upper bound on the genuine ground-state energy  $\psi_{GS}$ . Assume that  $\psi_{Tri}$  is normalized according to equation 2.9 while  $\psi_{Tri}$  then it equals the ground state ( $\psi_{Tri} = \psi_{GS}$ ). This shows that entity  $E_{Tri}$  is equivalent to the exact ground state energy  $E_{GS}$ , additionally, we can reconfigure equation 2.10 for the ground state as:

$$\langle E_{GS} \rangle = \int \psi_{GS} \, H \, \psi_{GS}^* \, d\vec{r} \tag{2.11}$$

We can figure out from normalized  $\psi_{Tri}$  that  $E_{Tri} > E_{GS}$  or  $E_{Tri} = E_{GS}$ . As a result, the best choice for  $E_{Tri}$  is the one in which  $E_{Tri}$  is lowered [3, 4, 6].

# 2.4 The Hohenberg-Kohn Theorems.

DFT is fundamentally based on Hohenberg-Kohn theorems; in 1964, Hohenberg and Kohn verified the use of the electron density  $n(\vec{r})$  to calculate the ground state energy. These theorems can be explained by two potent assertions.

The first theory: holds that the density of any interacting many particle systems in external potential  $V_{ext}(\vec{r})$  is uniquely defined. Furthermore, this can be computed because it shows that the density  $n(\vec{r})$  is used instead of the potential as a basic function uniquely giving a description of the system, and be stated as the ground state density  $n_{GS}(\vec{r})$  that is expressly relied on to establish the potential up to an arbitrary constant [6, 10, 17, 19].

This theorem is supported by two distinct external potentials:  $V_{ext}(\vec{r})_{(1)}$  and  $V_{ext}(\vec{r})_{(2)}$ . The difference between the two is more than a constant, but they provide the same ground state density  $n_{GS}(\vec{r})$ . It is clear that the earlier two potentials correspond to different Hamiltonians,  $H_{ext}[(\vec{r})]_{(1)}$  and  $H_{ext}[(\vec{r})]_{(2)}$ , and they give rise to distinct wave-functions  $\Psi_{ext}[(\vec{r})]_{(1)}$  and  $\Psi_{ext}[(\vec{r})]_{(2)}$ .

Because the ground state of the systems is the same and we follow the variational principle, there is no wave-function that gives less energy than of  $\Psi_{ext}[(\vec{r})]$  (1) for  $H_{ext}[(\vec{r})]$  (1).

This is written as:

$$\langle E_{(1)} \rangle = \int \Psi_{(1)} H_{(1)} \Psi_{(1)}^* d\vec{r} < \int \Psi_{(2)} H_{(2)} \Psi_{(2)}^* d\vec{r}$$
 (2.12)

As a result, for non-degenerate ground states with similar ground state densities for the two Hamiltonians, equation 2.12 is given as:

$$\int \Psi_{(2)} H_{(1)} \Psi_{(2)}^* d\vec{r} 
\frac{(E_{(2)})}{= \int \Psi_{(2)} H_{(2)} \Psi_{(2)}^* d\vec{r}} 
+ \int \left\{ \left[ V_{\text{ext}} (\vec{r}) \right]_{(1)} - \left[ V_{\text{ext}} (\vec{r}) \right]_{(2)} \right\} n_{GS} (\vec{r}) d\vec{r}$$
(2.13)

By modifying the labels in equation 2.13, we get:

$$\int \Psi_{(1)} H_{(2)} \Psi_{(1)}^* d\vec{r}$$

$$\frac{(E_{(1)})}{= \int \Psi_{(1)} H_{(1)} \Psi_{(1)}^* d\vec{r}} + \int \{ [V_{\text{ext}}(\vec{r})]_{(2)} - [V_{\text{ext}}(\vec{r})]_{(1)} \} n_{GS}(\vec{r}) d\vec{r}$$
(2.14)

The results of adding equations 2.13 and 2.14 are as follows:

$$\langle E_{(1)} \rangle + \langle E_{(2)} \rangle < \langle E_{(2)} \rangle + \langle E_{(1)} \rangle \tag{2.15}$$

The equation (2.15) has a logical contradiction. As a result, the theorem has been confirmed by reduction ad absurdum. The second theorem provides a variational ansatz for getting the value for  $n(\vec{r})$ , which is used in searching for  $n(\vec{r})$  that minimizes energy. This also means that we may specify a general functional expression for the given energy  $E[n(\vec{r})]$ , by expressing it in terms of the density  $n(\vec{r})$ . The system's ground state energy  $(V(\vec{r}))$  is the global minimum value of this functional, and the density  $n(\vec{r})$  represents the density of the system. This minimizes the function and also represents the actual ground state density  $n(\vec{r})$ . Concerning the second proof, the first theorem informs us that the total energy of the system is expressed as a function of the density  $n(\vec{r})$  and is provided by:

$$E_{\text{total}} [n(\vec{r})] = \frac{F_{H-K}[n(\vec{r})]}{T_{\text{int}} [n(\vec{r})] + \underbrace{U_{\text{ee}} [n(\vec{r})]}_{\text{exeron}} + \int V_{\text{ext}} (\vec{r}) n(\vec{r}) d\vec{r}$$

$$= \text{zero, for non-interacting}$$

$$verter$$

$$verter$$

$$(2.16)$$

The first two terms of equation (2.16)  $(F_{H-K}[n(\vec{r})])$  are kinetic energy  $(T_{int})$  and electronelectron interaction energy  $(U_{ee})$  which are evaluated as the same for the entire system. As a result,  $F_{H-K}[n(\vec{r})]$  is a universal function that has been uniquely defined as the Holy Grail of density functional theory [12]. Assuming the system is in the ground state, the energy can be represented particularly by the ground state density  $n_{GS}(\vec{r})$  as:

$$\langle E_{GS} \rangle = \langle E[n_{GS}(\vec{r})] \rangle = \int \Psi_{GS} H_{GS} \Psi_{GS}^* d\vec{r}$$
 (2.17)

According to variational principle, the ground state energy that corresponds directly to the ground state density is the minimal energy, and any alternative density will essentially produce a greater energy:

$$\begin{split} \langle E_{GS} \rangle &= \langle E[n_{GS}(\vec{r})] \rangle \\ &= \int \Psi_{GS} H_{GS} \Psi_{GS}^* d\vec{r} < \int \Psi H \Psi^* d\vec{r} \\ &= \langle E[n(\vec{r})] \rangle = \langle E \rangle \end{split}$$

After evaluating the functional  $F_{H-K}[n(\vec{r})]$  we may determine the total energy to be minimized with regard to variations in the density function, as indicated in equation 2.16. It results in the exact ground state properties of the system that we are pursuing, for most practical computations, direct minimization does not provide a vivid guide to the ground state energy as supplied by the Kohn-Sham approach.

#### 2.5 Kohn-Sham Method and Self-Consistent Field SFC.

Kohn and Sham's efforts showed that the Hohenberg-Kohn theory can be applied to both interacting and non-interacting systems. Density function theory (DFT) is sceptical of providing a broadening on the interacting many particles problems. The main advantage of

the non-interactive system over the interacting system is that the ground-state energy of a non-interacting system may be found with ease. The concept was developed in 1965 by Kohn and Sham. They discovered that an effective Hamiltonian  $(H_{eff})$  of the non-interacting system can be substituted for the original Hamiltonian of the system in an effective external potential  $V_{eff}(\vec{r})$ , They also noted that the system produces the same ground state density as the original system. The Kohn Sham technique's output is regarded as ansatz, and there is no clear way for carrying out the computations. However, it is notably simpler to solve than the non-interacting problem. The Kohn-Sham technique is based on the Hohenberg-Kohn universal density [6,9,10,20]:

$$F_{H-K}[n(\vec{r})] = T_{int}[n(\vec{r})] + U_{ee}[n(\vec{r})]$$
 (2.18)

The Hohenberg-Kohn functional for non-interacting electrons in a system can be reduced to calculate only the kinetic energy. Furthermore, the energy function of the Kohn-Sham ansatz  $F_{K-S}[n(\vec{r})]$  is presented with the following mathematical computation, which differs from the computation evaluated in equation 2.16:

$$F_{K-S}[n(\vec{r})] = T_{non}[n(\vec{r})] + E_{Hart}[n(\vec{r})] + \int V_{ext}(\vec{r})n(\vec{r})d\vec{r} + E_{xc}[n(\vec{r})].$$
(2.19)

In the non-interacting system,  $T_{\text{non}}$  represents its kinetic energy, which is different from  $T_{\text{int}}$  for the interaction system as found in equation 2.16. On the other hand,  $E_{\text{Hart}}$  represents the classical electrostatic energy, also known as the classical self-interaction energy of the electron gas, and is associated with the density  $n(\vec{r})$  in the system. The exchange-correlation energy functional in the system is denoted by the term  $E_{xc}$  and is provided by:

$$E_{xc}[n(\vec{r})] = F_{H-K}[n(\vec{r}) - \frac{1}{2} \int \frac{n(\vec{r}_1)n(\vec{r}_2)}{|\vec{r}_1 - \vec{r}_2|} d\vec{r}_1 d\vec{r}_2 -$$

$$T_{\text{non}}[n(\vec{r})]$$
(2.20)

The first three terms in equation 2.19 can be easily transformed into a functional form. On the other hand, this is provided generally without a specific functional form for the  $E_{xc}$ . Over the past few years, many attempts have been made to thoroughly investigate the possibility of improving the computation of  $E_{xc}$ . Currently, the functional properties of a wide variety of solid-state systems and molecules may be studied and predicted. In addition, the functional derivatives of the last three variables in equation 2.19 are used to create the effective single particle potential  $V_{eff}(\vec{r})$ 

$$V_{eff}(\vec{r}) = V_{ext}(\vec{r}) + \frac{\partial E_{Hart}[n(\vec{r})]}{\partial n(\vec{r})} + \frac{\partial E_{xc}[n(\vec{r})]}{\partial n(\vec{r})}$$
(2.21)

In addition, we can use this potential to obtain the single particle's Hamiltonian logically:

$$H_{K-S} = T_{non} + V_{eff} \tag{2.22}$$

For this Hamiltonian, the Schrödinger equation may be obtained by:

$$[T_{non} + V_{eff}]\Psi_{K-S} = E\Psi_{K-S}$$
 (2.23)

The expression defined by equation 2.23 is known as the Kohn-Sham equation. The ground state density  $n_{GS}^{K-S}(\vec{r})$  corresponds to the ground state wave-function  $\Psi_{GS}^{K-S}$  whose evaluation minimises the Kohn-Sham functional subject to the orthonormalization requirements  $\langle \Psi_i \mid \Psi_j \rangle = \delta_{ij}$ , as established by a self-consistent calculation. Density functional theory (DFT) makes extensive use of a self-consistent field approach; for example, it is assumed that  $E_{\text{Hart}}$  " and  $E_{xc}$  can be precisely calculated. The primary challenge currently is that  $V_{eff}$  cannot be estimated until the most suitable ground state density is identified; the actual density cannot be determined from the Kohn-Sham wave-functions until equation 2.23 is

solved to obtain the actual value of  $V_{eff}$  for a given system. As a result, the circular problem can be efficiently determined by carrying out a self-consistent cycle, as seen in Figure 2.1.

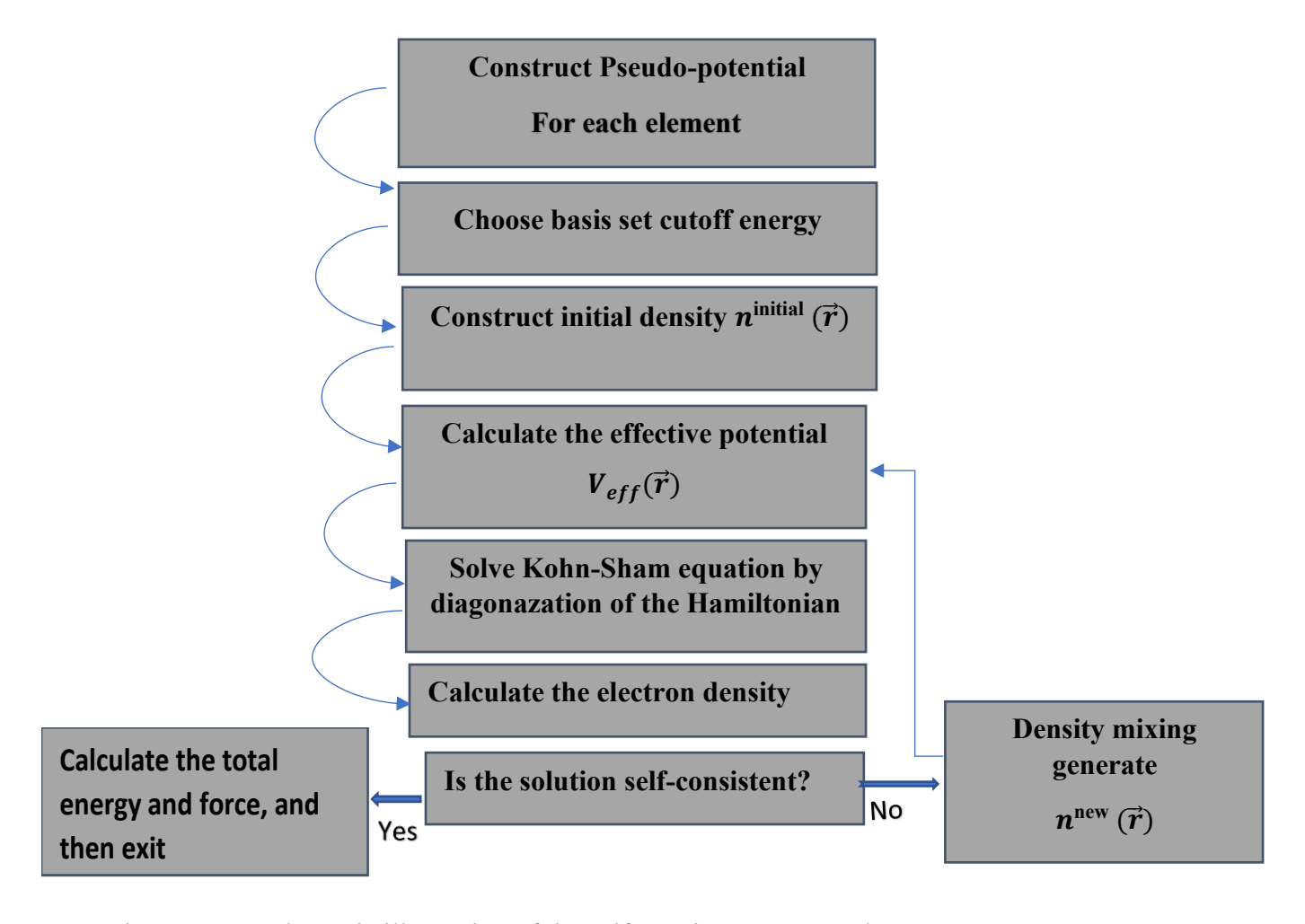


Figure 2.1: a schematic illustration of the self-consistent DFT cycle.

According to figure 2.1, the first stage in the study is to create the pseudo-potential, which reflects the electrostatic interaction between valence electrons, nuclei, and core electrons in a system. The next stage is to create the necessary basis set to be plugged in, choosing a kinetic energy cutoff; this phase is specifically meant to expand density functional values.

Obviously, if the density of the system is known, the energy functional may be fully computed. An initial estimate is defined as a trial electronic density  $n^{\text{initial}}(\vec{r})$ . As a result, the initial guess can be used to determine the following amount:

$$G = E_{\text{Hart}} \left[ n^{\text{initial}} \left( \vec{r} \right) \right] + E_{xc} \left[ n^{\text{initial}} \left( \vec{r} \right) \right]$$
 (2.24)

The effective potential  $V_{eff}$  and the parameters  $\frac{\partial G}{\partial n^{\text{initial}}(\vec{r})}$  are determined. The effective  $V_{eff}$  potential is used to solve Kohn-Sham equation 2.23, which gives an outline for a solution to the electron Hamiltonian. The Hamiltonian is obtained, and then diagonalized to get the eigenfunctions and the new electron density,  $n^{\text{new}}(\vec{r})$ . The term  $n^{\text{new}}(\vec{r})$  is closer to true ground state and has been validated. If the new updated electron density  $n^{\mathrm{new}}\left(\vec{r}\right)$  is discovered to agree numerically with the starting density  $n^{\text{initial}}(\vec{r})$  used to construct the Hamiltonian at the start of the SCF cycle, where one ends at the conclusion of the loop, then this will satisfy the condition of self-consistency. After that, we stop the operations and compute all of the required converged quantities, such as the electronic band structure, density of states, and total energy. On the other hand, if the new density  $n^{\text{new}}(\vec{r})$  differs from the original density  $n^{\text{initial}}(\vec{r})$ , a new input density must be created, starting a new SCF cycle. It then follows once more that in order to compute the density and confirm its selfconsistency, a new density-dependent Hamiltonian must be constructed [3, 17, 23]. By using the Kohn-Sham technique, it is clear that a complex system with several bodies may be accurately mapped onto a set of basic non-interacting equations, provided that the exchange correlation functional is known. It should be noted that the exchange-correlation functional is not specifically defined, that require the use of approximate values.

### 2.6. The Exchange-Correlation Potential.

The DFT is a fairly reliable and proven method for analysis, although it still requires an estimate for the kinetic energy functional and the exchange-correlation functional in terms of density for the system being studied. A significant amount of effort has been directed into finding reliable expressions for these kinds of functionals. The most commonly utilised exchange-correlation functional approximations are the more complex Generalised Gradient Approximation (GGA), which incorporates the derivative of the density, and the Local Density Approximation (LDA), which is primarily dependent on the density. This GGA is semi-local because it includes environmental information.

### 2.7. Local Density Approximation (LDA).

According to Kohn-Sham theory, the functional  $E_{xc}$  parameter could be determined in a homogeneous electron gas to approximate the many body particle problem in a less complicated system [11].

Kohn-Sham's research shown that the functional  $E_{xc}$  at point  $\vec{r}$  may be represented as acting in a uniform density by slowly but systematically changing the system's density. In addition, the  $E_{xc}$  functional is given by a uniform electron gas  $E_{xc}^{\text{homo}}$   $[n(\vec{r})]$  with a density  $n(\vec{r})$ .

In general, systems that have been dominated by electron-electron interactions cannot be accurately described by the local density approximation (LDA). However, LDA implies that the density is constant in the local region around any particular location. The example below shows the expression for  $E_{xc}^{LDA}[n(\vec{r})]$ , which represents the local density approximation (LDA).

$$E_{xc}^{LDA}[n(\vec{r})] = \int E_{xc}^{\text{homo}}[n(\vec{r})]n(\vec{r})d\vec{r} \qquad (2.25)$$

41

The exchange-correlation energy  $E_{xc}^{\text{homo}}$   $[n(\vec{r})]$  can be divided into two parts: This is the result of adding together the exchange energy  $E_x^{\text{homo}}$   $[n(\vec{r})]$  and the correlation energies  $E_c^{\text{homo}}$   $[n(\vec{r})]$ ; this can be found individually. The exchange-correlation energy  $E_{xc}^{\text{homo}}$   $[n(\vec{r})]$  can be calculated in the following manner:

$$E_{xc}^{\text{homo}}\left[n(\vec{r})\right] = E_{x}^{\text{homo}}\left[n(\vec{r})\right] + E_{c}^{\text{homo}}\left[n(\vec{r})\right] \tag{2.26}$$

The exchange term can be obtained analytically and can be found in different academic books:[6,12].

$$E_{\chi}^{\text{homo}}[n(\vec{r})] = -\frac{3}{4} \left(\frac{3n(\vec{r})}{\pi}\right)^{1/3}$$
 (2.27)

The correlation energy for the system, represented as  $(E_c^{\text{homo}}[n(\vec{r})])$  cannot be calculated analytically. However, it can be accurately determined using numerical methods. The most common and accurate method was conducted by Ceperly and Alder (CA) utilising quantum Monte-Carlo simulations. Multiple interpretations of the Monte Carlo data exist. One notable example is the calculation performed by Perdew and Punger (PZ), who fitted the numerical data into an analytical formula and produced [25,26].

$$E_c^{\text{homo}}[n(\vec{r})] = \begin{cases} -0.048 + 0.031 \ln(r_o) - 0.0116r_o + 0.002 \ln(r_o) & \text{if } r_o < 1 \\ -\frac{0.1423}{(1+1.9529\sqrt{r_o}+0.3334r_o)} & \text{if } r_o > 1 \end{cases}$$
(2.28)

The equation above is calculated for values of  $r_0 > 1$  and values of  $r_0 < 1$ . Where the  $r_o$  represents the average radius of the electrons in a homogeneous electron gas.  $r_0$  defined as  $\left(\frac{3}{4\pi n}\right)^{1/3}$ . While it is a well-known and powerful functional, the local density approximation (LDA) is simple to use and accurate for materials like graphite and carbon nanotubes where the electron density won't change rapidly. A significant error is predicted for atoms with d

and f orbitals. The band gap in semiconductors and insulators is often not accurate with a considerable error within the range of 0.5 to 2eV or 10-30%. This is only one example of the many problems with the above functional to a reasonable amount. For the reasons mentioned above, it is highly appropriate to use better functional [25, 27, 28].

### 2.8. Generalized Gradient Approximation (GGA).

Although the systems are in reality non-homogeneous, the local density function (LDA) treats all systems as units of homogeneous systems. To constructively take this into account, one can go beyond the LDA and expand it by including the density derivative into the exchange correlation functional. The gradient and higher spatial derivatives of the total charge density are the most practical ways of achieving this.

I.e. 
$$(|\nabla n(\vec{r})|, |\nabla^2 n(\vec{r})|, ...)$$

Higher spatial derivatives are used to evaluate the total charge density in the approximation layout.

The functional mentioned above is referred to as the generalized gradient approximation (GGA). Since there is a clear formulation for the exchange part of the functional in this case, numerical analytic methods must be employed to determine it along with the correlation contributions. In the generalized gradient approximation (GGA), there are many parameterizations available for the exchange-correlation energies, exactly as there are for the local density function (LDA) [29–32].

In this section, we will look at the proposed functional suggested by (PBE) Perdew, Burke, and Ernzerhof [29]. The parameterization provided has two different expressions, the exchange  $E_x^{GGA}[n(\vec{r})]$  is the first expression and presented by:

$$E_{x}^{GGA}[n(\vec{r})]E_{x}^{GGA}[n(\vec{r})] = \int n(\vec{r})E_{x}^{homo}[n(\vec{r})]F_{x}(s)d\vec{r}$$
 (2.29)

43

Additionally,

$$F_{x}(s) = 1 + \kappa - \frac{\kappa}{(1+\mu s^2)/\kappa}$$

where the enhancement factor can be calculated by  $F_x(s)$ ,  $\kappa = 0.804$ ,  $\mu = 0.21951$ , s =

 $|\nabla n(\vec{r})/2k_S n(\vec{r})|$  indicates the gradient in density that is dimensionless,  $k_S = \sqrt{\frac{4k_{T-F}}{\pi a_o}}$ , and  $k_{T-F} = \frac{(12/\pi)^{1/3}}{\sqrt{r_S}}$ , where  $r_S$  is the local Seitz radius and is the Thomas-Fermi screening wavenumber.

The correlation energy  $E_x^{GGA}[n(\vec{r})]$  is the following expression.

The correlation energy  $E_x^{GGA}[n(\vec{r})]$  can be written as follows:

$$E_c^{GGA}[n(\vec{r})] = \int \left( E_c^{\text{homo}}[n(\vec{r})] + \chi[n(\vec{r})] \right) d\vec{r}$$

$$\chi[n(\vec{r})] = \frac{e^2}{a_o} \gamma \ln \left( 1 + \frac{\beta}{\gamma} t^2 \frac{1 + At^2}{1 + At^2 + A^2 t^4} \right),$$

$$A = \frac{\beta}{\gamma} \left[ e^{\left( \frac{E_C^{\text{homo}}[n(\vec{r})]}{\gamma} \right) - 1} \right]^{-1}$$
(2.30)

Where:  $\gamma = (1 - \ln{(2)}/\pi^2, t = |\nabla n(\vec{r})/2k_{T-F}n(\vec{r})|$  is an additional dimensionless density gradient,

$$\beta = 0.066725$$
, and  $a_0 = \frac{\hbar}{me^2}$ .

LDA and GGA are the two most desirable and often utilised methods for estimating exchange-correlation energies in the DFT. Similarly, there are various more functionals that predominate in LDA and GGA. In the illustration, it is technically accurate that there is no strong theory supporting the validity of these functionals. It is computed by testing the functional for various materials across a wide range of systems and then comparing the findings to provable empirical data for similar situations.

#### **2.9. SIESTA.**

All calculations in this thesis were carried out using the DFT implementation in the SIESTA code. The computations are utilised to obtain a relaxed geometry for the researched structures as well as to investigate their electrical characteristics. The SIESTA acronym, which refers to "Spanish Initiative for Electronic Simulations with Thousands of Analogues," is commonly used. The SIESTA concept is a self-consistent density functional theory (DFT) approach that relies on a Linear Combination of Atomic Orbital Basis set (LCAOB) and norm-conserving pseudo-potentials to produce consistent results for the computations [33–40]. Using SIESTA, there are essentially two ways to carry out density function theory (DFT) simulations. The first involves solving the Kohn-Sham equations using the conventional self-consistent field diagonalization method, while the second involves directly minimising a modified energy functional [36]. This section is meant to describe some of the SIESTA's components and how they are implemented in the provided code.

### 2.10. Bibliography

- [1] N. Argaman and G. Makov, 'Density Functional Theory -- an introduction', *American Journal of Physics*, vol. 68, Jul. 1998, doi: 10.1119/1.19375.
- [2] R. Dronskowski, Computational chemistry of solid state materials a guide for materials scientists, chemists, physicists and others. Weinheim [Germany: Wiley-VCH, 2005.
- [3] H. Eschrig, *The fundamentals of density functional theory*, 2nd ed., rev.Extended. Leipzig: Edition am Gutenbergplatz, 2003.
- [4] W. Kohn, A. D. Becke, and R. G. Parr, 'Density Functional Theory of Electronic Structure', *J. Phys. Chem.*, vol. 100, no. 31, pp. 12974–12980, Jan. 1996, doi: 10.1021/jp9606691.
- [5] R. M. Martin, Electronic Structure: Basic Theory and Practical Methods, 2nd ed. Cambridge: Cambridge University Press, 2020. doi: 10.1017/9781108555586.
- [6] R. G. Parr and Y. Weitao, *Density-Functional Theory of Atoms and Molecules*. Oxford University Press, 1994.
- [7] A. Kumar, 'A Brief Introduction to Thomas-Fermi Model in Partial Differential Equations'.
- [8] E. H. Lieb, 'Erratum: Thomas-Fermi and related theories of atoms and molecules', *Rev. Mod. Phys.*, vol. 54, no. 1, pp. 311–311, Jan. 1982, doi: 10.1103/RevModPhys.54.311.
- [9] E. K. U. Gross and R. M. Dreizler, *Density Functional Theory*. Springer Science & Business Media, 2013.
- [10] P. Hohenberg and W. Kohn, 'Inhomogeneous Electron Gas', *Phys. Rev.*, vol. 136, no.3B, pp. B864–B871, Nov. 1964, doi: 10.1103/PhysRev.136.B864.

- [11] W. Kohn and L. J. Sham, 'Self-Consistent Equations Including Exchange and Correlation Effects', *Phys. Rev.*, vol. 140, no. 4A, pp. A1133–A1138, Nov. 1965, doi: 10.1103/PhysRev.140.A1133.
- [12] W. Koch and M. C. Holthausen, *A Chemist's Guide to Density Functional Theory*, 1st ed. Wiley, 2001. doi: 10.1002/3527600043.
- [13] P. Geerlings, F. De Proft, and W. Langenaeker, 'Conceptual Density Functional Theory', *Chem. Rev.*, vol. 103, no. 5, pp. 1793–1874, May 2003, doi: 10.1021/cr990029p.
- [14] H. Eschrig, K. Koepernik, and I. Chaplygin, 'Density functional application to strongly correlated electron systems', *J. Solid State Chem. Fr.*, vol. 176, pp. 482–495, Dec. 2003, doi: 10.1016/S0022-4596(03)00274-3.
- [15] P. Ziesche and F. Tasnadi, 'Methods for electronic-structure calculations an overview from a reduced-density-matrix point of view'. arXiv, Dec. 19, 2003. doi: 10.48550/arXiv.cond-mat/0312516.
- [16] L. H. Thomas, 'The calculation of atomic fields', *Math. Proc. Camb. Philos. Soc.*, vol. 23, no. 5, pp. 542–548, Jan. 1927, doi: 10.1017/S0305004100011683.
- [17] K. Burke, 'The ABC of DFT', p. 92697, Apr. 2007. Department of Chemistry, University of California
- [18] B. G. Walker, C. Molteni, and N. Marzari, 'Ab initio molecular dynamics of metal surfaces', *J. Phys. Condens. Matter*, vol. 16, no. 26, p. S2575, Jun. 2004, doi: 10.1088/0953-8984/16/26/028.
- [19] W. Kohn, 'Nobel Lecture: Electronic structure of matter---wave functions and density functionals', *Rev. Mod. Phys.*, vol. 71, no. 5, pp. 1253–1266, Oct. 1999, doi: 10.1103/RevModPhys.71.1253.

- [20] M. Levy, 'Electron densities in search of Hamiltonians', *Phys. Rev. A*, vol. 26, no. 3, pp. 1200–1208, Sep. 1982, doi: 10.1103/PhysRevA.26.1200.
- [21] N. A. Lima, L. N. Oliveira, and K. Capelle, 'Density-functional study of the Mott gap in the Hubbard model', *Europhys. Lett.*, vol. 60, no. 4, p. 601, Nov. 2002, doi: 10.1209/epl/i2002-00261-y.
- [22] N. H. March, 'Self-consistent fields in atoms', Pergamon Press, Oxford, Jan. 1975.

  [Online]. Available: https://www.osti.gov/biblio/4081678
- [23] W. Kohn and L. J. Sham, 'Self-Consistent Equations Including Exchange and Correlation Effects', *Phys. Rev.*, vol. 140, no. 4A, pp. A1133–A1138, Nov. 1965, doi: 10.1103/PhysRev.140.A1133.
- [24] D. M. Ceperley and B. J. Alder, 'Ground State of the Electron Gas by a Stochastic Method', *Phys. Rev. Lett.*, vol. 45, no. 7, pp. 566–569, Aug. 1980, doi: 10.1103/PhysRevLett.45.566.
- [25] J. P. Perdew and A. Zunger, 'Self-interaction correction to density-functional approximations for many-electron systems', *Phys. Rev. B*, vol. 23, no. 10, pp. 5048–5079, May 1981, doi: 10.1103/PhysRevB.23.5048.
- [26] S. S. Naghavi, 'Theoretical study of correlated systems using hybrid functionals', Johannes Gutenberg-Universität Mainz, 2011. doi: 10.25358/OPENSCIENCE-3284.
- [27] L. Hedin and S. O. Lundqvist, 'Effects of Electron-Electron and Electron-Phonon Interactions on the One-Electron States of Solids', in *Solid State Physics*, vol. 23, F. Seitz, D. Turnbull, and H. Ehrenreich, Eds., Academic Press, 1969, pp. 1–181. doi: 10.1016/S0081-1947(08)60615-3.

- [28] S. H. Vosko, L. Wilk, and M. Nusair, 'Accurate spin-dependent electron liquid correlation energies for local spin density calculations: a critical analysis', *Can. J. Phys.*, vol. 58, no. 8, pp. 1200–1211, Aug. 1980, doi: 10.1139/p80-159.
- [29] J. P. Perdew, K. Burke, and M. Ernzerhof, 'Generalized Gradient Approximation Made Simple', *Phys. Rev. Lett.*, vol. 77, no. 18, pp. 3865–3868, Oct. 1996, doi: 10.1103/PhysRevLett.77.3865.
- [30] A. D. Becke, 'Density-functional exchange-energy approximation with correct asymptotic behavior', *Phys. Rev. A*, vol. 38, no. 6, pp. 3098–3100, Sep. 1988, doi: 10.1103/PhysRevA.38.3098.
- [31] B. Hammer, L. B. Hansen, and J. K. Nørskov, 'Improved adsorption energetics within density-functional theory using revised Perdew-Burke-Ernzerhof functionals', *Phys. Rev. B*, vol. 59, no. 11, pp. 7413–7421, Mar. 1999, doi: 10.1103/PhysRevB.59.7413.
- [32] J. P. Perdew and Y. Wang, 'Accurate and simple analytic representation of the electrongas correlation energy', *Phys. Rev. B*, vol. 45, no. 23, pp. 13244–13249, Jun. 1992, doi: 10.1103/PhysRevB.45.13244.
- [33] J. M. Soler, E. Artacho, J. D. Gale, A. Garcia, J. Junquera, P. Ordejon, and D. Sanchez-Portal, 'The SIESTA method for ab initio order-N materials simulation', *J. Phys. Condens. Matter*, vol. 14, no. 11, p. 2745, Mar. 2002, doi: 10.1088/0953-8984/14/11/302.
- [34] D. Sanchez-Portal, P. Ordejon, E. Artacho, and J. M. Soler, 'Density-functional method for very large systems with LCAO basis sets', *Int. J. Quantum Chem.*, vol. 65, no. 5, pp. 453–461, 1997, doi: 10.1002/(SICI)1097-461X(1997)65:5<453::AID-QUA9>3.0.CO;2-V.
- [35] E. Artacho, J.D.G., A. Junquera, R. M. Martin, P. Ordejon, D. Sanchez-Portal, and J.M. Soler. SIESTA 3.1 User's Guide. (2011).

- [36] P. Ordejón, D. A. Drabold, M. P. Grumbach, and R. M. Martin, 'Unconstrained minimization approach for electronic computations that scales linearly with system size', *Phys. Rev. B*, vol. 48, no. 19, pp. 14646–14649, Nov. 1993, doi: 10.1103/PhysRevB.48.14646.
- [37] L. Kleinman and D. M. Bylander, 'Efficacious Form for Model Pseudopotentials', *Phys. Rev. Lett.*, vol. 48, no. 20, pp. 1425–1428, May 1982, doi: 10.1103/PhysRevLett.48.1425.
- [38] D. R. Hamann, M. Schlüter, and C. Chiang, 'Norm-Conserving Pseudopotentials', *Phys. Rev. Lett.*, vol. 43, no. 20, pp. 1494–1497, Nov. 1979, doi: 10.1103/PhysRevLett.43.1494.
- [39] N. Troullier and J. L. Martins, 'Efficient pseudopotentials for plane-wave calculations', *Phys. Rev. B*, vol. 43, no. 3, pp. 1993–2006, Jan. 1991, doi: 10.1103/PhysRevB.43.1993.
- [40] N. Troullier and J. Martins, 'A straightforward method for generating soft transferable pseudopotentials', *Solid State Commun.*, vol. 74, no. 7, pp. 613–616, May 1990, doi: 10.1016/0038-1098(90)90686-6.

# Chapter 3

## 3.1 Single Particle Transport Theory

Once the density functional theory notion for the electronic structure of an isolated molecule has been explained, the next step is to connect the isolated molecule to semi-infinite leads and then calculate the probability of transmission through the system from one electrode to the other. The explanation can be expanded by employing the Green's function scattering equation. In this discussion, I will explore the techniques that use scattering theory and Green's function methods. These methods explain the electrical and thermoelectric characteristics of nanoscale systems located between two metallic electrodes.

#### 3.2 Introduction

Single-particle transport theory is the main numerical technique used to explore various molecular geometrics. It involves a thorough examination of electronic characteristics [1]. The primary objective of molecular electronics is to understand the electronic structure of molecular junctions. The molecule is linked between electrodes, and the movement of charge occurs across the molecule in a phase-coherent manner. The interaction between the lead and molecule is fairly weak compared to the binding strengths within an electrode and between molecules. A primary challenge in molecular electronics is the method of attaching the molecule to metallic or other electrodes in order to investigate its electrical characteristics. A scattering process occurs due to the transfer of movement between the electrode and the molecule, as well as between the molecule and the electrode. The scattering mechanism that arises from the electrode and the molecular bridge can be accurately explained by employing a complete formalism based on Green's function. In this chapter, this discussion will focus on the derivation of the Landauer formula, followed by an explanation of the process for a retarded Green's function that is applicable to a one-dimensional tight-binding chain. The

Green's function is directly related to the transmission coefficient by breaking the periodicity of the lattice at a single link, which creates the scattering area.

#### 3.3 The Landauer Formula

To explain transport phenomena, the Landauer formula, [1-4], is utilised. This formula is valid for ballistic mesoscopic systems in which the energy of an electron is preserved and is relevant for phase coherent systems, where a single wave function sufficiently describes the flow of electrons. This leads to a formula that relates the conductance of the system to the S-matrix of a scattering region connected to two semi-infinite leads. This chapter will cover the method used to compute such transmission properties.

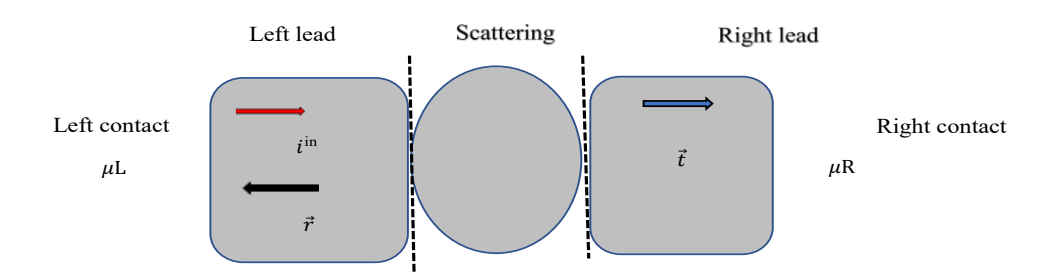


Figure 3.1: A contact-linked mesoscopic scatterer, where  $\mu_L$  and  $\mu_R$  represent the chemical potential in the left and right lead, respectively.

where r is the amplitude of the reflected wave due to an incoming left wave, and t is the amplitude of the transmitted wave. When the temperature is zero (T = 0 K) and there is no scattering region, the current  $\delta I$  due to left travelling electrons in an energy interval  $\delta E = \delta I = e \ vg\delta n$ , where  $\delta n = \frac{\partial n}{\partial E} \delta E$  is the number of left-moving electrons per unit length in the energy interval  $\delta E$ , whereas vg represents their group velocity. If reservoirs emit both left

and right-moving electrons, the net current is transported by electrons in the energy range  $\delta E$ =  $\mu L - \mu R$ .

This schematic shows a conceptual structure of an experimental or measuring system with contacts, leads, and magnetic areas, which is intended to help in the analysis of magnetic and electrical interactions within the device.

For  $\mu$ R and  $\mu$ L are not equal because the current flows from left to right or up, or the opposite. So the potential shouldn't be equal.

In the above structure, a wave will be transmitted to the right with probability  $T = |\vec{t}|^2$  and reflected with probability  $R = |\vec{r}|^2$ , when an incident wave  $i^{\text{in}}$  collides with the scatterer from the left. The incident electrons must either be reflected or transmitted, resulting in the conservation of probability, which for single-channel leads is expressed as T+R=1.

To understand the formula's essential concepts, imagine a mesoscopic scatterer coupled to two contacts that serve as electron reservoirs and are formed by two ideal ballistic leads, as illustrated in Figure 3.1. The reservoirs [3] contain all inelastic relaxation processes. These reservoirs have variable chemical potentials, allowing electrons to move from the left to the right. In the case of a single open channel, the electric current generated by the chemical potential difference at zero temperature:

$$\delta I = e v_g \left(\frac{\partial n}{\partial E}\right) (\mu L - \mu R)$$
(3.1)

where, e is the electronic charge,  $v_g$  is the group velocity, and  $\partial n/\partial E$  is the density of states (DOS). When the system is defined as one-dimensional, we can write:

$$\frac{\partial \mathbf{n}}{\partial \mathbf{E}} = \frac{\partial \mathbf{n}}{\partial \mathbf{k}} \frac{\partial \mathbf{k}}{\partial \mathbf{E}} = \frac{\partial \mathbf{n}}{\partial \mathbf{k}} \frac{1}{v\hbar}$$
 (3.2)

$$\frac{\partial \mathbf{n}}{\partial \mathbf{k}} = \frac{1}{\pi}, \frac{\partial \mathbf{n}}{\partial \mathbf{k}} = \frac{1}{v\hbar} \tag{3.3}$$

Equation 3.3 is one-dimensional since it defines the group velocity as  $v = \frac{1}{\hbar} \frac{\partial k}{\partial E}$ , the equation can be expressed as follows, where a spin factor of two is added.

$$\delta I = \frac{2e}{h}(\mu_L - \mu_R) = \frac{2e^2}{h}\delta V \tag{3.4}$$

The voltage in this case,  $\delta V$ , represents the potential chemical difference. From equation 3.4, it is obvious that in the absence of a scattering region, the conductance of a single open channel is equal to  $\frac{2e^2}{h}$ , which is about  $77\mu S$  and the corresponding resistance is  $\frac{h}{e^2}$ , is approximately 12.9k $\Omega$ . When the system includes a scattering area, a part of the current is reflected with a probability  $R = |\vec{r}|^2$ , while another part is transmitted with a probability  $T = |\vec{t}|^2$ . The current that will move to the scatterer on the right side of the lead is:

$$\delta I = \frac{2e^2}{h}T\delta V \to \frac{\delta I}{\delta V} = \frac{2e^2}{h}T$$
 (3.5)

Equation 3.5 is the Landauer formula for conductance,  $G = \left(\frac{2e^2}{h}\right)T(E_F)$ , in which the transmission coefficient is evaluated at the Fermi energy  $E_F[5]$ . Then, in 1985, Buttiker extended the Landauer formula to include more than one open channel. In this case, the transmission coefficient can be substituted by the total of all transmission amplitudes representing electrons that travel from the left to the right contact. Equation 3.5 of the Landauer formula for several open channels becomes:

$$\frac{\delta I}{\delta V} = G = \frac{2e^2}{h} \sum_{i,j} \left| t_{i,j} \right|^2 = \frac{2e^2}{h} \operatorname{Trace} \left( tt^{\dagger} \right)$$
 (3.6)

Here, G is the electrical conductance and  $t_{i,j}$  is the amplitude of transmission representing scattering from the  $j^{th}$  channel of the left lead to the  $i^{th}$  channel of the right lead. By

combining the transmission and reflection amplitudes, the scattering S matrix involving the electron from the left lead and the right lead can be represented as follows:

$$S = \begin{pmatrix} r & t' \\ t & r' \end{pmatrix} \tag{3.7}$$

where, r and t describe electrons arriving from the left, whereas r'and t' indicate electrons coming from the right. In equation 3.8 r, t, r' and t' are considered as complex matrices that satisfy  $SS^+ = I$  for many open channels due to conservation.

### 3.4 Thermoelectric Coefficients

The Seebeck, Peltier, and Thompson effects established connections between heat, current, temperature, and voltage around the turn of the nineteenth century [1]. The Seebeck effect is the creation of electrical current due to a temperature difference, whereas the Thompson and Peltier effects describe the cooling or heating of a current-carrying conductor [6]. A more general mechanism involves a temperature difference ( $\Delta T$ ) and a theoretical voltage drop ( $\Delta V$ ) in the system, resulting in the flow of heat currents and charge. The generalised Landauer-Büttiker equations for heat (Q), charge (I), and currents within the linear basis and temperature regimes will be used to derive expressions for the thermoelectric coefficients of a device with two terminals. The system consists of a scattering zone that connects to two leads, which in turn connect to a pair of electron reservoirs. These reservoirs are generated using the chemical potential  $\mu_L$  and  $\mu_R$ , temperature  $T_L$  and  $T_R$ , and the Fermi distribution function [6]:

$$f_i(E) = \left(1 + e^{\frac{E - \mu_i}{k_B T_i}}\right)^{-1} \tag{3.8}$$

Assuming that the reservoirs and leads are connected so that scattering does not occur at their interface, it may be stated that the central scattering area is the source of all scattering effects. The right moving charge current of a single k-state issuing from the left reservoir can be defined in terms of the number of electrons per unit length n, the Fermi distribution  $f_L$ , the group velocity  $v_q$ , and the scattering zone's transmission coefficient T(E).

$$I_k^+ = nev_a(E(k))T(E(k))f_L(E(k))$$
 (3.9)

Thus, the total charge current can be calculated from the right moving states by summing all positive k states and then converting the result into the integral form, where n=1/L for the electron density and  $v_g=\frac{1}{\hbar}\frac{\partial E(k)}{\partial k}$ .

$$I_k^+ = \sum_k e^{\frac{1}{L}} \frac{1}{\hbar} \frac{\partial E(k)}{\partial k} T(E(k)) f_L(E(k)) = \int_{-\infty}^{+\infty} \frac{2e}{h} T(E) f_L(E) dE$$
 (3.10)

Similarly, we get the following for left moving states:

$$I_k^- = \int_{-\infty}^{+\infty} \frac{2e}{h} T(E) f_R(E) dE \tag{3.11}$$

Thus, the total current can be expressed as follows:

$$I = I^{+} - I^{-} = \frac{2e}{h} \int_{-\infty}^{+\infty} T(E)(f_{L}(E) - f_{R}(E)) dE$$
 (3.12)

The above equation is Landauer-Bttiker formula at finite temperatures.

A comparable derivation for the identical system's heat current (alternatively, energy current) can be provided by beginning with the relation  $Q = Env_g$  rather than  $= nev_g$ . The final result is similar to the previous results, but it includes two more energy terms:

$$Q = Q^{+} - Q^{-} = \frac{2}{h} \int_{-\infty}^{+\infty} T(E) ((E - \mu_{L}) f_{L}(E) - (E - \mu_{R}) f_{R}(E)) dE$$

Where,

$$f_L(E) = \left[1 + e^{\frac{E - \mu - \frac{\Delta \mu}{2}}{k_B \left(T + \frac{\Delta T}{2}\right)}}\right]^{-1}, f_L(E) = \left[1 + e^{\frac{E - \mu - \frac{\Delta \mu}{2}}{k_B \left(T + \frac{\Delta T}{2}\right)}}\right]^{-1},$$

$$\mu_L = \mu + \frac{\Delta \mu}{2}, \ \mu_R = \mu - \frac{\Delta \mu}{2}$$

Buttiker, Imry, Landauer, and others [7-10] establish a relationship between the electric current (I) and heat current (Q) in a system, and the voltage difference ( $\Delta V$ ) and temperature difference ( $\Delta T$ ) in the linear response regime. The thermoelectric coefficients G, L, M, and K are related to both electric currents, temperature, and potential differences [1 and 11-12].

$$\begin{pmatrix} I \\ \dot{Q} \end{pmatrix} = \begin{pmatrix} G & L \\ M & K \end{pmatrix} \begin{pmatrix} \Delta V \\ \Delta T \end{pmatrix} \tag{3.13}$$

The Onsager relation describes the relationship between the thermoelectric coefficients L and M in the absence of a magnetic field:

$$M = -LT \tag{3.14}$$

In equation 3.14, T represents temperature. The following relations can be expressed by rearranging these equations and using the measurable thermoelectric coefficients, electrical resistance R = 1/G, thermopower  $S = -\Delta V/\Delta T$ , Peltier coefficient, and thermal constant k:

$$\begin{pmatrix} \Delta V \\ \dot{Q} \end{pmatrix} = \begin{pmatrix} \frac{1}{G} & -\frac{L}{G} \\ \frac{M}{G} & K - \frac{LM}{G} \end{pmatrix} \begin{pmatrix} 1 \\ \Delta T \end{pmatrix} = \begin{pmatrix} R & S \\ \Pi & -K \end{pmatrix} \begin{pmatrix} 1 \\ \Delta T \end{pmatrix}$$
 (3.15)

The thermopower S can be defined in terms of the voltage  $\Delta V$  caused by a temperature differential  $\Delta T$  in the absence of an electrical current.

$$S = -\binom{\Delta V}{\Delta T}_{I=0} = \frac{L}{G'} \tag{3.16}$$

In the absence of a temperature differential, the Peltier coefficient  $\Pi$  refers to the heat transported purely by the charge current.

$$\Pi = \left(\frac{\dot{Q}}{I}\right)_{\Lambda T = 0} = \frac{M}{G} = -ST \tag{3.17}$$

Finally, in the absence of an electric current, thermal conductance k is defined as the heat current due to temperature drop:

$$k = -\left(\frac{\dot{Q}}{\Delta T}\right)_{I=0} = -\left(1 + \frac{S^2 GT}{k}\right)$$
 (3.18)

Therefore, assessing the values of S or  $\Pi$  offers valuable information about the system's capacity to function as a heat-driven current generator or a current-driven cooling device.

In addition, the thermoelectric figure of merit, ZT[13,14], can be defined based on these measurable thermoelectric coefficients:

$$ZT = \frac{S^2GT}{k} \tag{3.19}$$

In classical electronics, the ZT is determined by computing the highest induced temperature difference created by an applied electric current in the presence of Joule heating. Consider a current-carrying conductor that is located between two heat baths  $T_L$  and  $T_R$ , as well as electrical potentials  $V_L$  and  $V_R$ .

The thermoelectric figure of merit is obtained by calculating the conductor's greatest induced temperature differential caused by an electrical current. We can obtain the following from equation (3.13) by defining  $(\dot{Q})$  as the gain in heat from bath L to bath R:

$$\dot{Q} = \Pi I - k\Delta T \tag{3.20}$$

The left bath cools while the right bath heats as a result of this heat transfer, increasing  $\Delta T$ .

The sum of Joule heating can be computed with the proportional formula  $\dot{Q}_J = RI^2$ , which takes into account both the electrical resistance and the square of current. This Joule heating influences the temperature differential created by heat transfer, therefore in the steady state case:

$$\Pi I - k\Delta T = \frac{RI^2}{2} \tag{3.21}$$

where R/2 represents the total of the internal and external resistances that are parallel.

The difference in temperature becomes:

$$\Delta T = \frac{1}{k} \left( \Pi I - \frac{RI^2}{2} \right) \tag{3.22}$$

The temperature difference-current relationship is represented by equation 3.15.

The derivative of equation 3.16 can determine the maximum temperature ( $\Delta T$ ):

$$\frac{\partial \Delta T}{\partial I} = \frac{\Pi - IR}{k} = 0 \tag{3.23}$$

To determine the greatest  $\Delta T$ , we place  $I = \Pi/R$  and substitute equation 3.17 into the equation 3.23.

$$(\Delta T)_{\text{max}} = \frac{\Pi^2}{2kR} = \frac{S^2 T^2 G}{2k}$$
 (3.24)

$$\frac{(\Delta T)_{\text{max}}}{T} = \frac{S^2 GT}{2k} = \frac{1}{2}ZT \tag{3.25}$$

This shows that ZT is a dimensionless number which describes the 'efficiency' of a molecular device.

### 3.5 Theory of electron transport

To study electron transport, it is necessary to understand the transmission probability, which is related to the conductance G at the Fermi energy E using the Landauer formula [15,16].

$$G = G_0 T(E_F) \tag{3.26}$$

The electric conductance is shown by equation 3.26. G is described as a function of the Fermi energy and quantum conductance as  $G_0 = \frac{2e^2}{h}$ , where e is the electron charge and h is the Planck's constant. T(E) is also known as the transmission coefficient as a function of energy, and it can be defined as the probability that an electron with energy E will transfer

from one electrode to the other. This refers to the scattering formalism shown in the graphic below.

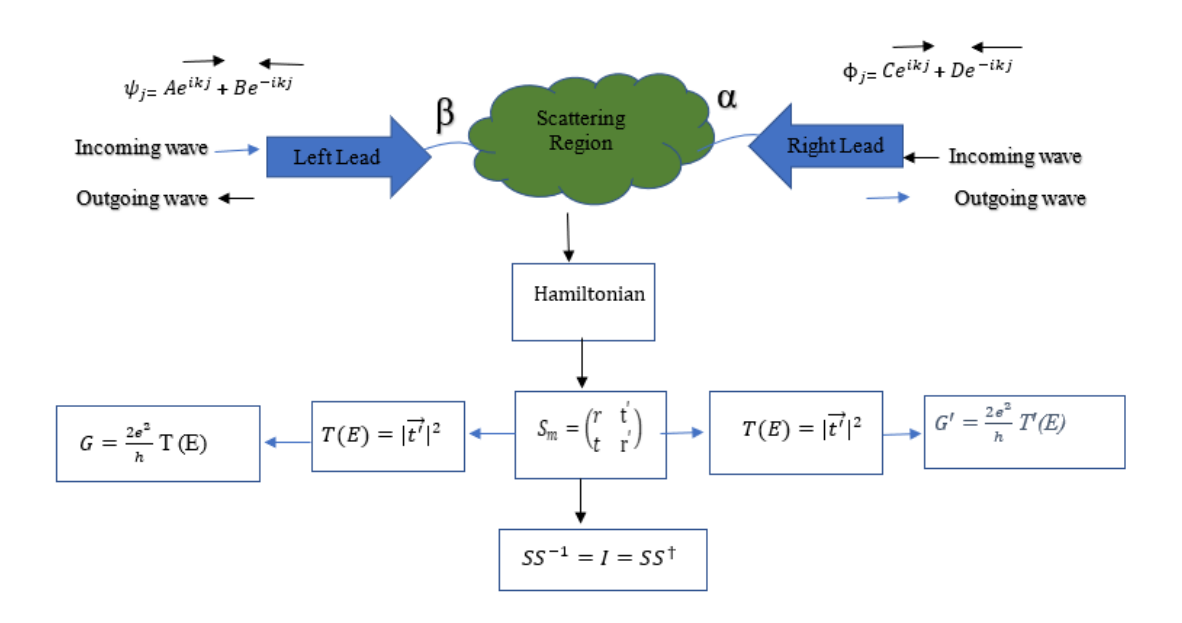


Figure 3.2 shows a representation of the transport mechanism. It shows the combination of mathematical structures. This mechanism has two categories of probability, R and T.

This schematic shows wave scattering in a system that consists of a core scattering zone connected to two leads—left and right. The incoming waves (t' on the left and outgoing waves on the right) approach the scattering zone, where they interact and are partly reflected and transmitted. The outgoing waves (r' on the left and transmitted on the right) leave from the scattering zone, carrying information about the encounter.

The fundamental idea shown here is the scattering matrix Sm, which connects the incoming and outgoing waves mathematically. In particular, it describes the way the scattering zone reflects and transmits waves, with parameters and possibly denoting things like transmission and reflection coefficients. This setting is crucial in quantum physics and wave mechanics,

and it is used to study how particles or waves behave when they encounter localised disturbances or barriers. It has applications in electronic transmission, optics, and other wavebased systems.

$$|\vec{t}|^2 + |\vec{r}|^2 = 1 T + R = 1$$

### 3.6 Scattering Theory

### 3.6.1 A one dimensional (1-D) linear crystalline lattice

To illustrate the calculation of the scattering matrix for a simple one-dimensional structure, I now provide a simple and straightforward overview of the method that used prior to presenting a generalized methodology [1]. A basic tight-binding model in periodic systems is proposed to provide a qualitative perspective on electronic system calculations. Each atom has a single atomic orbital of energy  $\epsilon_0$  and a inearest neighbour coupling or hopping element  $-\gamma$ , as shown in Figure 3.3.

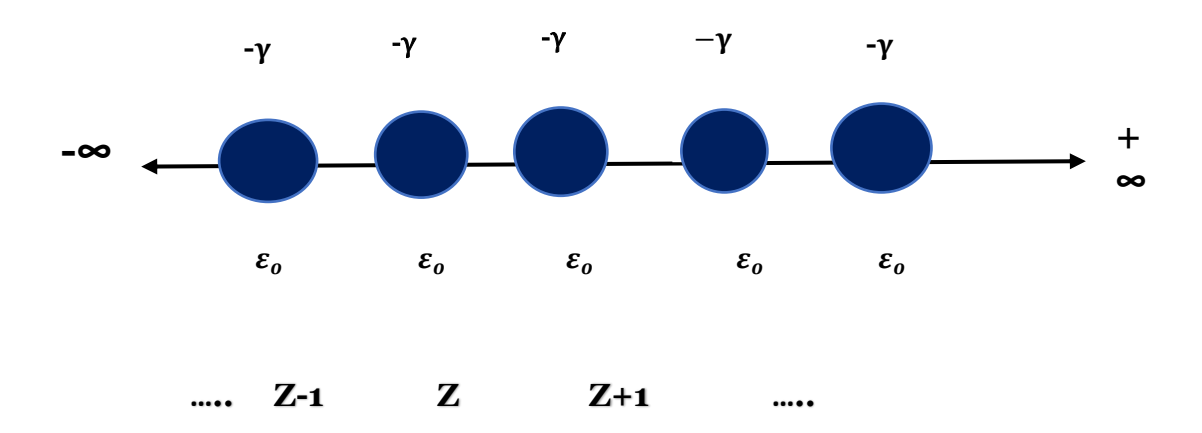


Figure 3.3: A tight-binding model of a (1-D) periodic lattice with energy sites and hopping elements is used to label our atoms.

This figure represents a range extending from negative infinity to positive infinity, with specific points at Z-1, Z, and Z+1 on a number line or axis. This suggests an emphasis on

discrete states or places within a system, which are most often related to transitions, differences, or interactions between neighbouring states at these points.

The notation and arrangement imply an examination of how qualities or quantities change or relate between these discrete points, which is frequent in models involving summations, probabilities, or physical states in domains such as quantum physics, statistical mechanics, and signal processing.

 $-\gamma$  represents a negative boundary or limit, while  $\epsilon$  is a small quantity used to analyse minor changes or mistakes in the system.

The Hamiltonian H describes the system as follows:

Then, the Schrodinger equation is utilised to obtain Z row of the Hamiltonian.

$$\varepsilon_0 \psi_z - \gamma \psi_{Z+1} - \gamma \psi_{Z-1} = E \psi_Z \tag{3.27}$$

$$\psi_z = e^{ikZ} \tag{3.28}$$

where  $\psi_z$  represents the wave function of this system on site z, which satisfies the Schrodinger equation 3.27.

By substituting a plane wave in equation 3.28 into equation 3.27, we obtain the dispersion relation stated in equation 3.30. We assume that  $\gamma = \gamma^*$ .

$$E = \varepsilon_0 - 2\gamma \cos(k) \tag{3.29}$$

In this context, the wave number is represented by the quantum number (k), while the wave function is related to the retarded Greens function, which is denoted g(z, z') and satisfies the following equation:

$$(E - H)g(z, z') = \delta_{(z, z')} -\gamma g(z - 1, z') + (E - \varepsilon_0)g(z, z') - \gamma g(z + 1, z') = \delta_{z, z'}$$
(3.30)

where  $\delta_{z,z'}=1$ , if z=z', and  $\delta_{z,z'}=0$ , if  $z\neq z'$ .

The Green's function g(z, z') of a system is defined to be the amplitude at the position z created by an an incoming wave at point z'. This excitation would generate two waves that pass across the locations of excitation. Figure 3.3 displays the values of their amplitudes B and D.

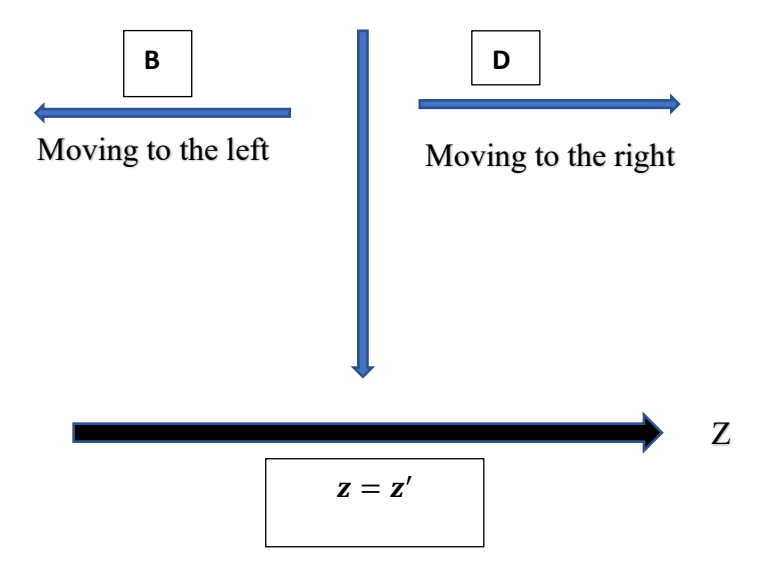


Figure 3.4. A representation of the retarded Green's function of an infinite lattice in one dimension. By exciting the point at z = z', the outgoing wave propagates in both the left and right directions. The amplitudes of these waves are B and D, respectively.

The outgoing waves with amplitudes B and D are shown in Figure 3.4 as they move away from the excitation point. Thus, the two waves can be expressed as follows:

$$g(z,z') = \begin{cases} De^{ikz}, & z \ge z' \\ Be^{-ikz}, & z \le z' \end{cases}$$
 (3.31)

The fact that the equation 3.31 match the equation 3.30 at all positions, except at point z = z' are not met, where the Green's function must be continuous.

$$[g(z,z')]_{\text{Left}} = [g(z,z')]_{\text{Right}}$$
 (3.32)

$$Be^{-ikz'} = De^{ikz'} (3.33)$$

$$B = e^{2ikz'} (3.34)$$

Now, we get the following:

$$g(z, z') \tag{3.35}$$

$$= \begin{cases} De^{ikz} = De^{ikz'}e^{ik(z-z')} & z \ge z' \\ De^{2ikz'}De^{2ikz'} = De^{ikz'}e^{ik(z'-z)} = De^{ikz'}e^{ik(z'-z)} & z \ge z' \end{cases}$$
(3.35)

It is obvious that the exponent of the complex number is consistently positive, so the simpler expression can be defined as:

$$g(z, z') = De^{ikz'}e^{ik|z'-z|}$$
 (3.36)

Furthermore, this equation must satisfy the Green's function,  $(E-H)g(z-z')=\delta_{(z,z')}$ :

$$\delta_{z,z'} = Eg(z,z') - \varepsilon_0 g(z-z') + \gamma g(z+1,z') + \gamma g(z-1,z')$$
 (3.37)

Therefore, the solution at z=z' is obtained as follows:

$$1 = (E - \varepsilon_0)g(z, z) + \gamma g(z + 1, z') + \gamma g(z - 1, z')$$
(3.38)

$$= De^{ikz'}[(E - \varepsilon_0)]e^{ik|z-z|} + \gamma e^{ik|z+1z|} + \gamma e^{ik|z-1z|}$$
(3.38)

When we solve it for  $De^{ikz'}$ , we obtain:

$$\frac{1}{De^{ikz'}} = (E - \varepsilon_0) + \gamma e^{ik} + \gamma e^{ik}$$
$$= (E - \varepsilon_0) + \gamma e^{ik} + \gamma e^{ik} + \gamma e^{-ik} + \gamma e^{-ik}$$
$$= \gamma e^{ik} - \gamma e^{-ik}$$

Using the group velocity  $hv_g=2\gamma\sin(k)$  , we may express the Green's function for a one-dimensional chain as:

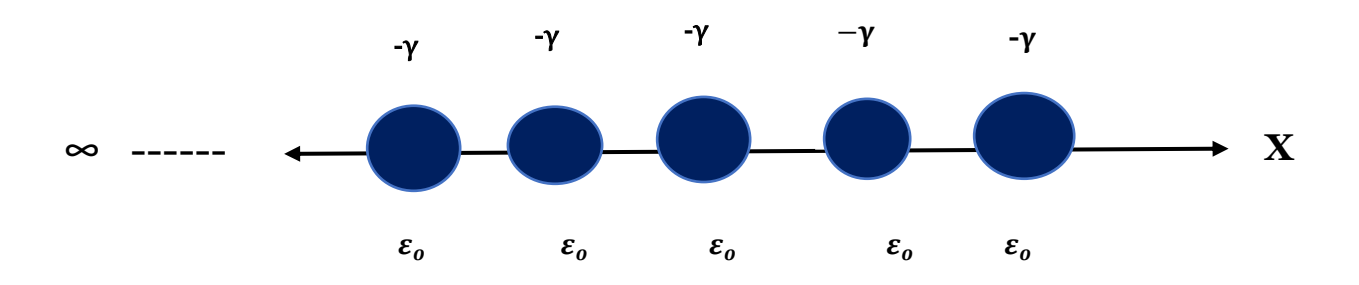
$$g^{R}(z,z') = \frac{1}{ih\nu_{g}} e^{ik|z-z'|}$$
 (3.40)

Several solutions to this problem have been presented in the literature [4, 17, 19]. We used the retarded Green's function  $g^R(z, z')$  to solve the problem in the equation above. However, the advanced Green's function  $g^A(z, z')$  provides an alternative answer.

$$g^{A}(z,z') = \frac{-1}{i\hbar v_{g}} e^{-ik|z-z'|} = \frac{i}{\hbar v_{g}} e^{-ik|z-z'|}$$
(3.41)

We can state that the retarded Green function represents the outgoing waves from an excitation point (z = z'), while the advanced Greens' function represents the two entering waves that disappear at the excitation point. Thus, the retarded Green's function will be employed for simplicity. We then remove the R from the formula, which becomes  $g(z, z') = g^R(z, z')$ , [1].

### 3.6.2 Semi-infinite one-dimensional lattice



.... 
$$z_0 - 3$$
  $z_0 - 2$   $z_0 - 1$   $z_0$ 

Figure 3.5 shows a tight-binding model for a semi-infinite one-dimensional lattice. This system consists of energy site  $\varepsilon_0$  and hopping elements (- $\gamma$ ). Sites labelled  $z_0$ ,  $z_0$ -1,  $z_0$ -2, $z_0$ -3, In this figure shows the function's behaviour or transformation over multiple z regimes, particularly at large magnitudes ( $\pm \infty$ ), showing asymptotic tendencies and probable singularities or unique points.  $Z_0$  may represent a particular point of interest (a pole, zero, or region where the function's behaviour is examined).

Shifts or translations along the complex plane or real line ( $z_0$ ,  $z_0$ -1,  $z_0$ -2, $z_0$ ,  $z_0$ -3...) demonstrate the function's behaviour at nearby places.

Gamma ( $\gamma$ ) is a fixed value or parameter in mathematical models that has a specific purpose. Epsilon ( $\epsilon$ ) is a small positive value that measures how close a function is to a specific limit or value.

First, we want to satisfy the boundary condition. This will be achieved by introducing an additional plane wave component with a new amplitude [1]:

$$g(z,z') = \frac{1}{ihv_q} e^{ik|z-z'|} + Ae^{-ik|z-z'|}$$
(3.42)

By applying the condition  $g(z, z_0) = 0, z \le z'$ , wehere

$$g(z, z_0) = \frac{1}{ihv_g} e^{ik(z_0 - z)} + Ae^{-ik(z_0 - z)}$$

yields

$$A = \frac{-1}{ihv_g} e^{2ik(z_0 - z)}$$
 (3.43)

Putting this back into Green's function allows us to find:

$$g(z,z') = \frac{1}{ihv_q} e^{ik(z'-z)} - \frac{1}{ihv_q} e^{2ik(z-z_0)} e^{-ik(z'-z)}$$

Next, we consider the second condition, which states that any point beyond  $(z_0 - 1)$  is not influenced by a source in the chain. Therefore, if  $z \ge z'$  and  $z = z_0$ , it is predicted that  $g(z_0, z) = 0$ . Based on this condition, we get:

$$g(z_0, z) = \frac{1}{ihv_g} e^{ik(z_0 - z')} - Ae^{-ik(z_0 - z')}$$
(3.44)

$$A = -\frac{1}{ihv_q} e^{2ik(z_0 - z')} \tag{3.45}$$

When we substitute this back into Green's function, we get:

$$g(z,z') = \frac{1}{ihv_g} e^{ik(z-z')} - \frac{1}{ihv_g} e^{2ik(z_0-z')} e^{-ik(z-z')}$$
 (3.46)

The following is written to summarize these two equations:

$$g(z,z') = \begin{cases} \frac{1}{ihv_g} \left[ e^{ik(z-z')} - e^{ik(2z_0 - z - z')} \right], z \ge z' \\ \frac{1}{ihv_g} \left[ e^{ik(z'-z)} - e^{ik(2z_0 - z - z')} \right], z \le z' \end{cases}$$
(3.47)

Additionally, it is possible to express the previous equation as:

$$g(z,z') = \frac{1}{ih\nu_a} \left[ e^{ik|z-z'|} - e^{ik(2z_0 - z - z')} \right] = g_{z,z'}^{\infty} + \Psi_{z,z'}^{z_0}$$
(3.48)

### 3.6.3 Scattering in one dimension (1-D)

In this section, we will provide a simple example, the surface Green's function is computed at the point  $z = z_0 - 1$ . Therefore, the surface Green's function can be stated as follows [1]:

$$g(z_0 - 1, z_0 - 1) (3.49)$$

$$= \frac{1}{ihv_g} \left[ e^{ik|z_0 - 1, z_0 - 1|} - e^{ik(2z_0 - z_0 + 1 - z_{0+1})} \right]$$
(3.49)

Now, we simplified this form to obtain:

$$g(z_0 - 1, z_0 - 1) = \frac{1}{ihv_g} - 2i\sin(k)e^{ik}$$
(3.50)

$$g(z_0 - 1, z_0 - 1) = \frac{2i\sin(k)}{2i\gamma\sin(k)}e^{ik} = -\frac{e^{ik}}{\gamma}$$
 (3.51)

## 3.6.4 One-dimensional (1-D) Scattering Using Green's Functions

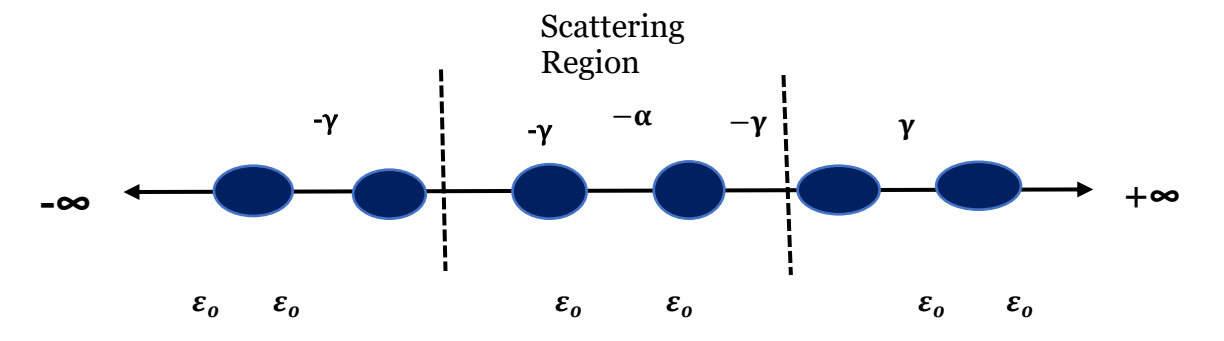


Figure 3.6: shows a tight binding model of two semi-infinite leads with site energy  $\varepsilon_0$  and couplings  $-\gamma$  connected through a hopping element  $-\alpha$ .

The scattering region is restricted between  $-\gamma$  and  $+\gamma$ , while the regions outside stretch to infinity. In the core region between  $-\gamma$  and  $+\gamma$ , the scattering interaction takes place, whilst the propagation zones unaffected by scattering are represented by the area between  $-\infty$  and  $-\gamma$  and between  $+\gamma$  and  $+\infty$ .

Scattering Region: The area where particles or waves are scattered.

The left region  $(-\infty \text{ to } -\gamma)$  represents the domain where particles or waves originate

or transit before reaching the scattering centre.

The scattering zone, located between  $-\gamma$  and  $+\gamma$ , is where scattering interactions occur.

The right region ranges from  $+\gamma$  to  $+\infty$ , and represents the area where particles or waves emerge after scattering.

In this case, we have two semi-infinite one-dimensional leads, both equal with  $\varepsilon_0$  on-site potential and  $-\gamma$  hopping elements. When the leads are decoupled ( $\alpha = 0$ ), the total Green function is obtained, which is defined as [1];

$$g = \begin{pmatrix} \frac{e^{ik}}{\gamma} & 0\\ 0 & -\frac{e^{ik}}{\gamma} \end{pmatrix}$$
 (3.52)

Given that we possess two semi-infinite leads that are not connected, we may express Green's function as  $g = (E - h_1)^{-1}$  where  $h_1$  is the Hamiltonian of these two leads. Thus, we have generated an infinite matrix for finding this Hamiltonian  $h_1$ , as follows:

$$h_{1} = \begin{pmatrix} \cdot & \cdot & 0 & 0 & 0 \\ \cdot & \varepsilon_{0} & -\gamma & 0 & 0 \\ 0 & -\gamma & \varepsilon_{0} & -\gamma & 0 \\ 0 & 0 & -\gamma & \varepsilon_{0} & -\gamma \\ 0 & 0 & 0 & 0 & \cdot \end{pmatrix}$$
(3.53)

By linking the two leads with a hopping element, the Hamiltonian for the complete system is  $H = h_1 + h_0$ , where  $h_0$  denotes the coupling parameters.

$$h_0 = \begin{pmatrix} 0 & \alpha \\ \alpha & 0 \end{pmatrix} \tag{3.54}$$

We now apply Dyson's equation to generate the Green's function for the coupled system:

$$G = (E - H)^{-1} = (E - h_1 - h_0)^{-1}$$
(3.55)

$$G = (g^{-1} - h_0)^{-1} (3.56)$$

The solution would be the following:

$$G = \left( \begin{pmatrix} -\frac{e^{ik}}{\gamma} & 0\\ 0 & -\frac{e^{ik}}{\gamma} \end{pmatrix}^{-1} - \begin{pmatrix} 0 & \alpha\\ \alpha & 0 \end{pmatrix} \right)^{-1}$$
(3.57)

$$G = \frac{1}{\gamma^2 e^{-2ik} - \alpha} \begin{pmatrix} -\gamma e^{-ik} & \alpha \\ \alpha^* & -\gamma e^{-ik} \end{pmatrix}$$
(3.58)

We will now compute the Greens' function as defined in equation (3.58) and use it in the Fisher Lee relation to get the transmission amplitude ( $t^*$ ) and reflection amplitude ( $r^*$ ). The scattering amplitudes of the scattering problem are determined by the Fisher Lee relation, which is related to the Green's function of the same issue.

The components of Green's function can be determined from equation (3.58), which allows for the definition of transmission and reflection coefficients. When two waves with amplitudes B and D are sent outward from the source (the excitation point), one wave is directed away from the scatter while the other is directed towards the scatter. Thus, two waves are represented by Green's function: one is a reflected wave or left wave  $(De^{-ik|z-z'|} + Bre^{ik|z-z'|})$  and the other is a transmitted wave or right wave  $(Bre^{ik|z-z'|})$ . In this example,  $\vec{t}$  represents the transmitted right wave and  $\vec{r}$  represents the reflected left wave, with arrows pointing in the amplitude directions.

$$1 + r = -ihv_g \frac{\gamma e^{-ik}}{\gamma^2 e^{-2ik} - \alpha^2}$$
 (3.59)

$$t = ihv_g \frac{\alpha e^{ik}}{\gamma^2 e^{-2ik} - \alpha^2} \tag{3.60}$$

Now, we compute the transmission and reflection probability as follows:

$$T = |\mathbf{t}|^2$$
 and  $R = |\mathbf{r}|^2$ 

Finally, the conductance of the system can be computed using the Landauer formula  $G = G_0T(E_F)$ .

# 3.7 Bibliography

- [1] C. J. Lambert, *Quantum Transport in Nanostructures and Molecules*. Institute of Physics Publishing, 2021. https://store.ioppublishing.org/page/detail/Quantum-Transport-in-Nanostructures-and-Molecules//?k=9780750336376
- [2] M. Büttiker, Y. Imry, R. Landauer, and S. Pinhas, 'Generalized many-channel conductance formula with application to small rings', *Phys. Rev. B*, vol. 31, no. 10, pp. 6207–6215, May 1985, doi: 10.1103/PhysRevB.31.6207.
- [3] M. Büttiker, Y. Imry, R. Landauer, and S. Pinhas, 'Generalized many-channel conductance formula with application to small rings', *Phys. Rev. B*, vol. 31, no. 10, pp. 6207–6215, May 1985, doi: 10.1103/PhysRevB.31.6207.
- [4] S. Datta, *Electronic Transport in Mesoscopic Systems*. Cambridge University Press, 1997.
- [5] J. C. Cuevas and E. Scheer, *Molecular Electronics: An Introduction to Theory and Experiment*. World Scientific, 2010.
  - [6] Finch, C. M. (2008). An understanding of the electrical characteristics of organic molecular devices (Doctoral dissertation, Lancaster University).
- [7] M. Büttiker, Y. Imry, R. Landauer, and S. Pinhas, 'Generalized many-channel conductance formula with application to small rings', *Phys. Rev. B*, vol. 31, no. 10, pp. 6207–6215, May 1985, doi: 10.1103/PhysRevB.31.6207.
- [8] V. V. Maslyuk, S. Achilles, and I. Mertig, 'Spin-polarized transport and thermopower of organometallic nanocontacts', *Solid State Communications*, vol. 150, no. 11–12, pp. 505–509, Mar. 2010, doi: 10.1016/j.ssc.2009.11.011.

- [9] V. M. García-Suárez, R. Ferradás, and J. Ferrer, 'Impact of Fano and Breit-Wigner resonances in the thermoelectric properties of nanoscale junctions', *Phys. Rev. B*, vol. 88, no. 23, p. 235417, Dec. 2013, doi: 10.1103/PhysRevB.88.235417.
- [10] N. R. Claughton and C. J. Lambert, 'Thermoelectric properties of mesoscopic superconductors', *Phys. Rev. B*, vol. 53, no. 10, pp. 6605–6612, Mar. 1996, doi: 10.1103/PhysRevB.53.6605.
- [11] U. Sivan and Y. Imry, 'Multichannel Landauer formula for thermoelectric transport with application to thermopower near the mobility edge', *Phys. Rev. B*, vol. 33, no. 1, pp. 551–558, Jan. 1986, doi: 10.1103/PhysRevB.33.551.
- [12] L. D. Hicks and M. S. Dresselhaus, 'Effect of quantum-well structures on the thermoelectric figure of merit', *Phys. Rev. B*, vol. 47, no. 19, pp. 12727–12731, May 1993, doi: 10.1103/PhysRevB.47.12727.
- [13] H. J. Goldsmid, *Thermoelectric Refrigeration*. Boston, MA: Springer US, 1964. doi: 10.1007/978-1-4899-5723-8.
- [14] Dissertations / Theses: "Carbon Electronic Properties" Grafiati'. https://www.grafiati.com/en/literature-selections/carbon-electronic-properties/dissertation/
- [15] Feng Duan-Introduction to Condensed Matter Physics-World Scientific Publishing Company (2005) 5 | PDF | Phase Transition | Group (Mathematics).
- [16] Gordey L, 'Electronic Transport in Meso- and Nano-Scale Conductors'https://www.yumpu.com/en/document/view/4775607/electronic-transport-in-meso-and-nano-scale-conductors

- [17] E. Economou, *Green's Function in Quantum Physics*, 1983. doi: 10.1007/3-540-28841-4.
- [18] P. A. Mello and N. Kumar, *Quantum Transport in Mesoscopic Systems: Complexity* and Statistical Fluctuations, a Maximum-entropy Viewpoint. Oxford University Press, 2004.
- [19] S. Sanvito, C. J. Lambert, J. H. Jefferson, and A. M. Bratkovsky, 'General Green's-function formalism for transport calculations with \$\mathrm{spd}\$ Hamiltonians and giant magnetoresistance in Co- and Ni-based magnetic multilayers', *Phys. Rev. B*, vol. 59, no. 18, pp. 11936–11948, May 1999, doi: 10.1103/PhysRevB.59.11936.

# **Chapter 4**

# Exploring Quantum Interference in Hexaazatrinaphthylene (HATNA) Molecules

### 4.1 Motivation

To achieve molecular-scale electrical processes beyond the von Neumann bottleneck, new forms of multi-functional switches are required that imitate self-learning or neuromorphic computing by dynamically switching between different operations based on their history. This chapter is motivated by the experimental work of ref. [1], in which hexaazatrinaphthylene (HATNA) molecules were reported to show memristive behaviors. However, the mechanism behind is unclear and no theory of transport through such molecules has been presented in the literature. Furthermore, the experiments of [1] were performed on self-assembled monolayers (SAMs) and it is not clear if their observed behaviour can be replicated in a single-molecule junction. I therefore investigated the transport properties of a HATNA series of singlemolecule junctions, which at least in the SAMs [1] includes molecules that switch between high and low conductance states upon reduction by hydrogen. Because of its time-domain and voltage-dependent plasticity, this dynamic molecular switch mimics synaptic behavior and Pavlovian learning and can supply all of the basic logic gates. This multifunctional switch could form a basis for molecular-scale hardware that can be used in solid-state devices, opening the way for dynamic complicated electrical actions contained within a single ultra-compact component.

### 4.2 Introduction

Motivated by brain energy efficiency and the growing demand for miniaturized electronics, there is a push to create devices that mimic the dynamic character of neurons and synapses in order to create trainable, adaptive computing networks or new hardware for deep learning for many kinds of applications such as pattern recognition, classification, or non-von Neumann neuromorphic computation [2-5]. Neuromorphic computing simulates synaptic plasticity in

electronic devices. Such processes are currently carried out utilizing advanced, energy-inefficient silicon-based circuits with enormous footprints, or mesoscale permissive devices based on ferroelectric [6] or phase change materials [7], filaments, or dopant migration [1, 3, 8]. In this context, molecular switches are interesting because to their intrinsic small size; but molecular switches are currently static, which means they switch between fixed on and off states (e.g., magnetic, redox, or conformational states) [9-11]. We present a dynamic molecular switch at a tunnel junction that remembers its history, with the switching probability and on/off state values changing on a continuous basis. This dynamic switch successfully simulates synaptic behavior and Pavlovian learning, as well as all two-terminal logic gates required for deep learning by using the junctions' time-domain plasticity. These functions are given inside a single molecular layer (2.4 nm thick), which is smaller than a neuron synapse ( $\sim 1-10\mu m$ ) by at least three orders of magnitude and thinner even than the synaptic gap (20-40 nm) by an order of magnitude. This dynamic nature represents a new kind of molecular switches that operate far outside of equilibrium, opening the way for molecular-scale neuromorphic computing.

One of the goals of neuromorphic electronics is to create computing systems in which training occurs at the hardware level. There is currently no molecular hardware available for this purpose. Unlike chemical switches previously investigated, biological switches, such as synapses, are dynamic and operate far outside of thermodynamic equilibrium [12,13], allowing them to be trained. Synapses transmit information in the form of an action potential from a presynaptic neuron to a postsynaptic neuron through the synaptic gap, which is regulated by a combination of excitatory and inhibitory neuronal inputs. Synapses can be strengthened or weakened based on their activity by combining different processes with different time constants, such as fast depolarization and slow diffusion of Ca<sup>2+</sup> and neurotransmitters [15]. This results in synaptic plasticity, enabling pulse pair facilitation and

depression with spike rate and timing dependent plasticity. To simulate synapses at the molecular level, we combined quick electron transfer (similar to action potentials and depolarization processes) with slow proton coupling limited by diffusion (similar to the role of Ca<sup>2+</sup> or neurotransmitters).

# 4.3. Studied Molecules

As discussed in [1], the HS-C10-HATNA molecules are made up of a 5,6,11,12,17,18-hexaazatrinaphthylene (HATNA) terminal that passes through six successive proton-coupled electron transfer (PCET) stages to generate a dynamic covalent N–H bond. Within a SAM, molecules can exist in a range of oxidation and protonation states, showed as Hn-HATNA, where n ranges from 0 to 6.

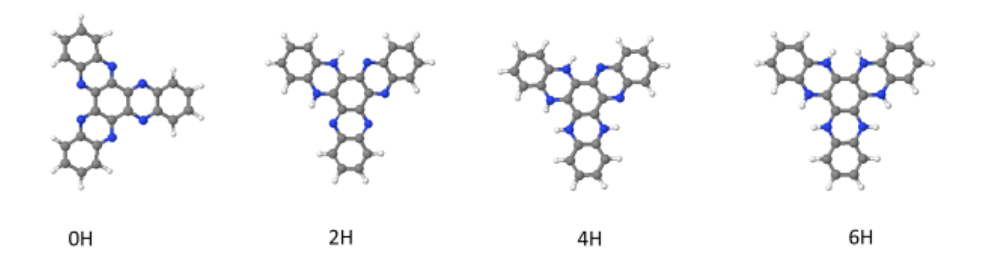


Figure 4.1. Molecules studied in this chapter, with zero Hs, two Hs, four Hs and six Hs attached to the nitrogen atoms (shown in blue).

### 4.4. Transmission coefficient T(E)

As noted in chapter 3, the transmission coefficient T(E) is an important measure for determining the electron transport properties of molecular junctions generated by HS-C10-HATNA molecules on gold substrates. T(E) represents the probability that an electron with energy E will pass through the molecular junction. The energy-dependent behavior of T(E) gives information on the junction's conductance characteristics at various bias voltages, including negative differential resistance (NDR) and hysteresis. The transmission coefficient T(E)) in dynamic molecular switches based on HS-C10-HATNA is impacted by factors such as the molecule structure, oxidation state, protonation state, and the presence of certain electronic states within the molecular energy levels. Changes in T(E) can be connected with the switching behavior of molecular junctions, where transitions between multiple states (e.g., 0H, 2H-1, 2H-2, 4H-1, 4H-2, 6H) lead to differences in the electron transport characteristics. We can learn more about the mechanisms driving the conductance switching and hysteresis seen in the molecular junctions by examining the energy-dependent transmission coefficient T(E) in conjunction with other parameters like the density of states and molecular orbitals. This understanding is critical for creating and optimizing moleculescale devices with specific electronic functions, as well as for future applications in nanoelectronics and molecular computing.

### 4.5. Frontier orbitals

The frontier orbitals of isolated HS-C10-HATNA molecules in different protonation states are critical in influencing their electronic characteristics and reactivity. These frontier orbitals, which include the highest occupied molecular orbital (HOMO) and the lowest unoccupied molecular orbital (LUMO), control the molecule's ability to take or donate electrons, engage in charge transfer reactions, and interact with other molecules or surfaces. Understanding the distribution and energy levels of these frontier orbitals is critical for

predicting the molecule's behavior in many settings and applications, including molecular electronics, catalysis, and sensing. Computational approaches such as density functional theory (DFT) can be used to investigate the frontier orbitals of HS-C10-HATNA molecules, providing information about their electronic structure and reactivity.

### 4.6. DFT calculations.

Note that when adding two hydrogens to the nitrogens, they can either be added to a branch connected to an anchor group, as in the molecule denoted 2H-1 in Figure 4.3, or to a branch which is not connected to a pendant group, as in the molecule denoted 2H-2 in figure 4.6.

Therefore in what follows, I shall examine the properties of six molecules, denoted 0H, 2H-1, 2H-2, 4H-1, 4H-2, and 6H. Clearly the junctions formed from 0H, 2H-2, 4H-2, and 6H are symmetric, whereas junctions formed from 2H-1, and 4H-1 are asymmetric. According to Breit-Wigner formula, for a symmetric molecular junction we will expect the transmission coefficient on resonance to equal 1, whereas for an asymmetric molecular junction, we expect the transmission coefficient on resonance to be less than one. In what follows, we shall see that this behaviour indeed is found within DFT calculations.

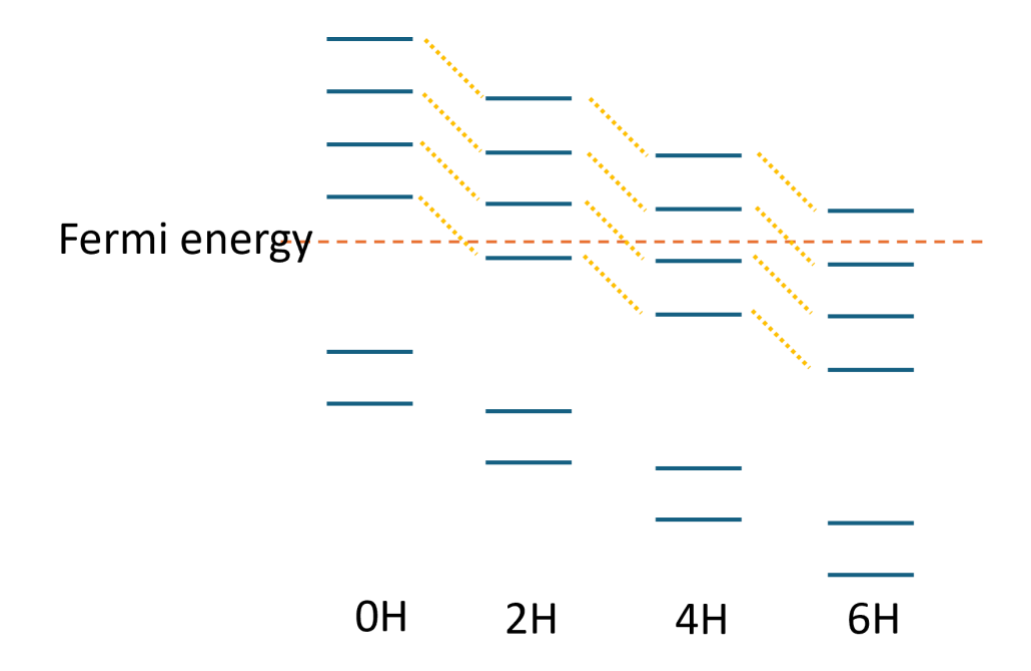


Figure 4.2 Schematic of energy level change after reducing by adding two H, four H and six H.

First, I compared the transport property of 0H and 2H to investigate the influence of reduction by two hydrogen atoms in two positions.

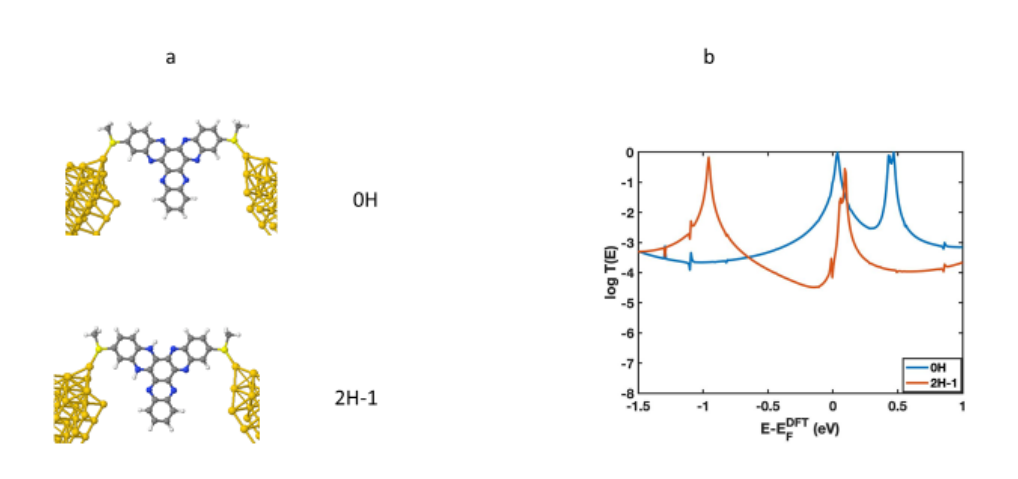


Figure 4.3. (a) the geometries of 0H and 2H-1 within a junction. (b) Transmission curves of 0H and 2H-1.

These show how distinct elements of the molecule or system are linked or interact with one another across different energies. They depict the system's electrical structure as well as the pathways that electrons can take inside it. Essentially, they help in our understanding of bonding, potential electronic states, and how the molecule's structure effects its conductive qualities. These represent the probability or efficiency of electrons moving through the system at certain energies. They are critical for knowing how well a molecule or device conducts electrons, showing high transmission (efficient conduction) and low transmission (barriers or resistance). These curves are critical for assessing electronic transport qualities and prospective performance in electronic applications. In the transmission curve that

introducing these two hydrogens and I'm pointing at the hydrogens gives the red curve that decreases the transmission coefficient of the Fermi energy. Introducing the two hydrogens definitely decreases the electrical conductance in a couple of orders of magnitude, which is a clear memristive effect. And then I'll also notice that the transmission resonances of the blue curve go to one, whereas the transmission resonance of the red curve does not go to one.

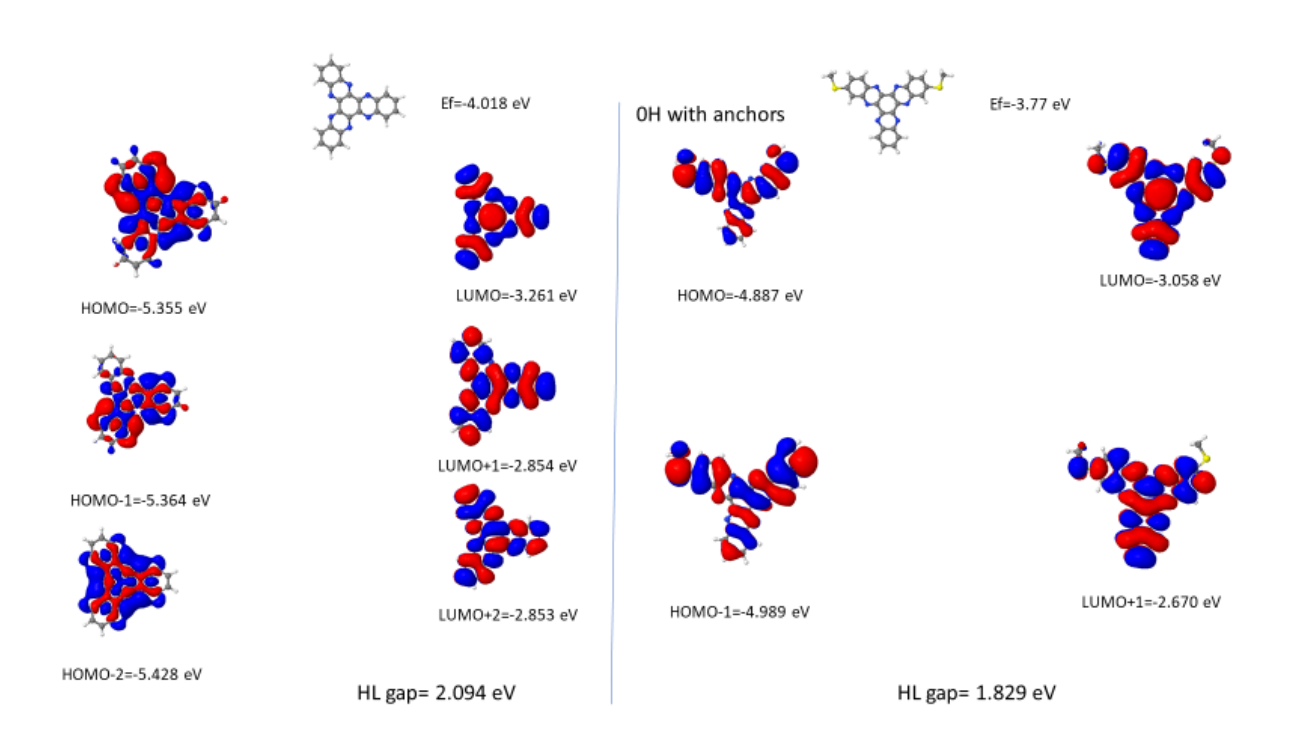


Figure 4.4. Wavefunctions of 0H without and with anchors.

The molecular orbitals are investigated, with a particular emphasis on the highest occupied molecular orbital (HOMO), the lowest unoccupied molecular orbital (LUMO), and related orbitals. different wavefunctions represent the probability distributions of electrons in various orbitals, which are critical for understanding the molecules' electrical characteristics, reactivity, and optical behaviour. The energies of these orbitals; the wavefunctions themselves are not shown or described in detail. In general, wavefunctions can be represented as spatial distributions that show the most probable locations for electrons. These

wavefunctions' symmetry and form have an impact on how molecules interact and take part in chemical reactions. Results indicate that the type of anchoring group has a substantial impact on the electrical structure of the molecule, as well as its potential uses in domains such as photovoltaics and catalysis.

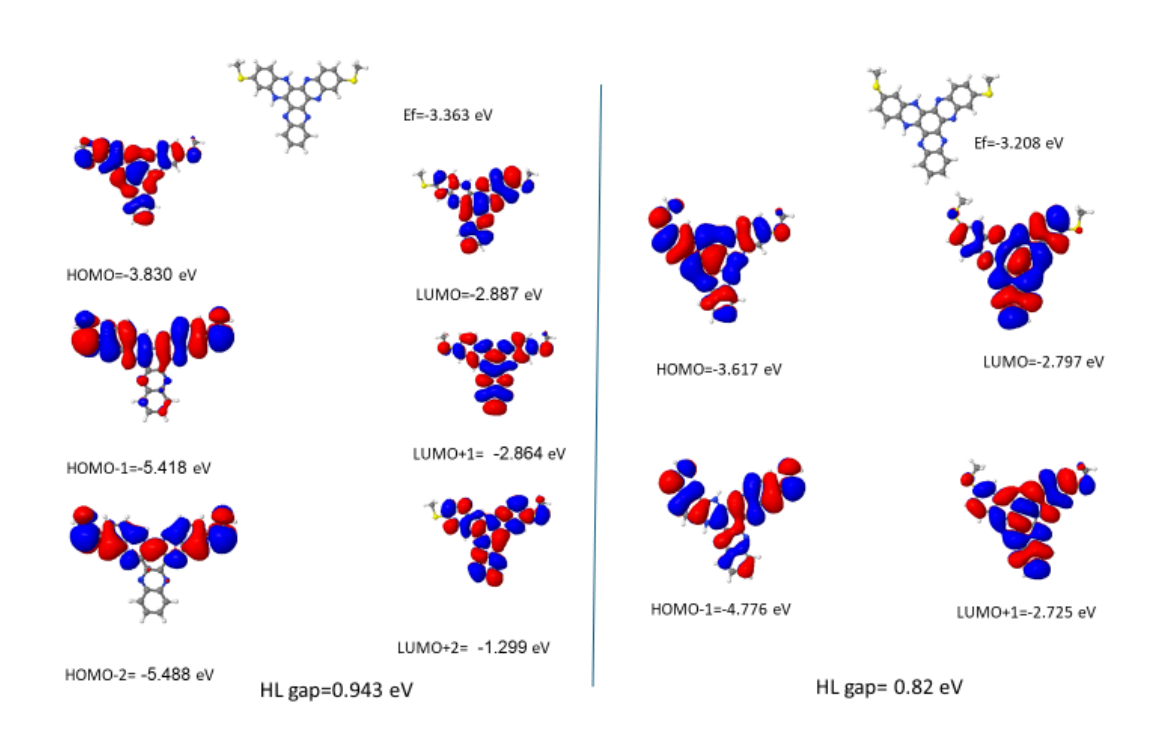


Figure 4.5: wavefunctions of 2H-1 with anchors

The transmission function in Figure 4.3 shows that making a transition from 0H to 2H-1 by adding the hydrogen reduces the conductance. Also, comparing the HOMO-LUMO gaps in figures 4.4 and 4.5 shows that HOMO -LUMO gap shrunk upon adding the hydrogen. Note that 0H is symmetric, since it is unchanged if rotated by 180° about the vertical axis. That means that the HOMO and LUMO resonances of the transmission curve should equal to 1 unless there's a degeneracy. However, 2H-1 is not symmetric and therefore as mentioned earlier, one expects that the transmission resonance will not equal 1 for the red curve. Consequently, as shown in Figure 4.3, even though the HOMO-LUMO gap of 2H-1 is

smaller than that of 0H, which normally increases the conductance, the conductance of 2H-1 goes down compared to that of 0H. As shown in Figure 4.4 and 4.5, this is also partly due to the decreased magnitude of the LUMO and LUMO+1 on the two anchors after reduction.

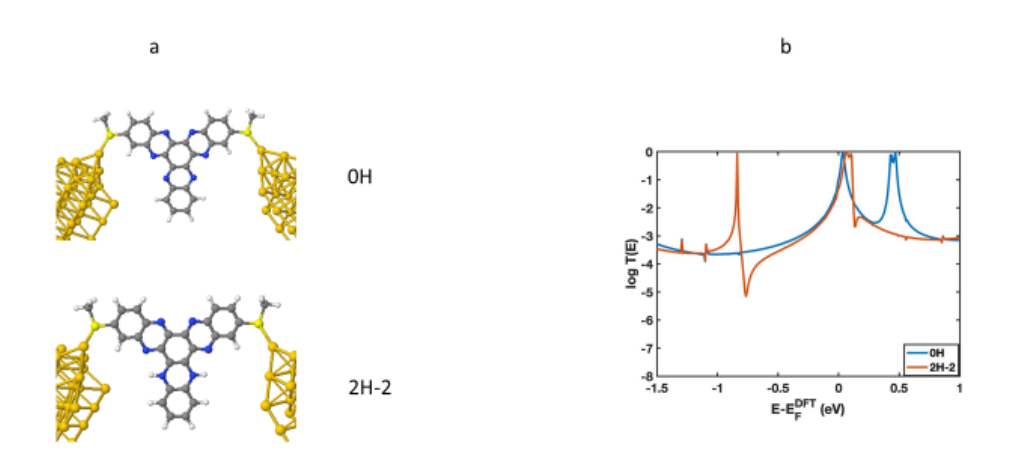


Figure 4.6. (a) the geometries of 0H and 2H-2 within junction. (b) Transmission curves of 0H and 2H-2.

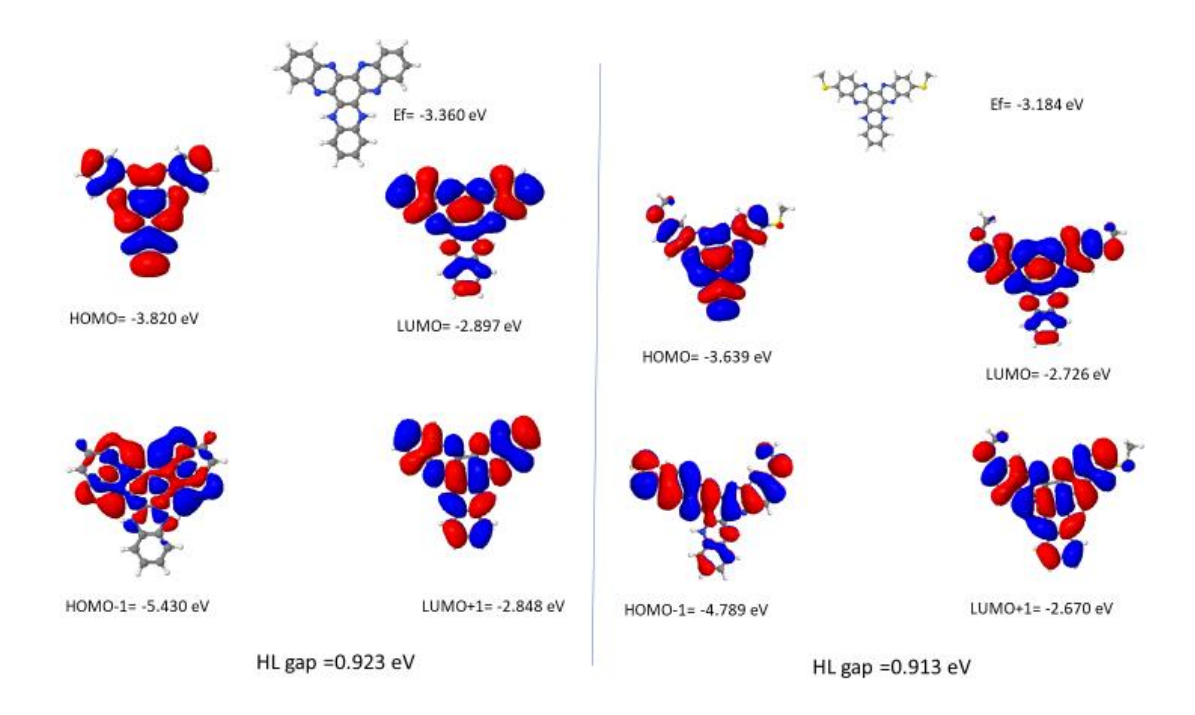


Figure 4.7. Wavefunctions of 2H-2 with and without anchors.

The molecule of 2H-2 with anchors is symmetric, so as shown in Figure 4.6, the transmission coefficient of the red curve on resonance is equal to one. Again we find that the HOMO-LUMO gap is reduced by introducing hydrogens. This may be expected, because typically, if we increase the size of a system, then the gap between the energy levels is decreased. In other words, if the orbitals are more delocalized then I will expect that decrease in the gap between energy levels.

According to the orbital product rule since the HOMO and the LUMO products have the same sign, DQI is predicted. This is evident in the red curve of Figure 4.6, but not the blue curve. For the latter, the LUMO is almost degenerate with the LUMO+1 and therefore the product rule cannot be applied.

I compare the transport properties of 0H and 4H to investigate the influence of reduction by four hydrogen atoms in two positions.

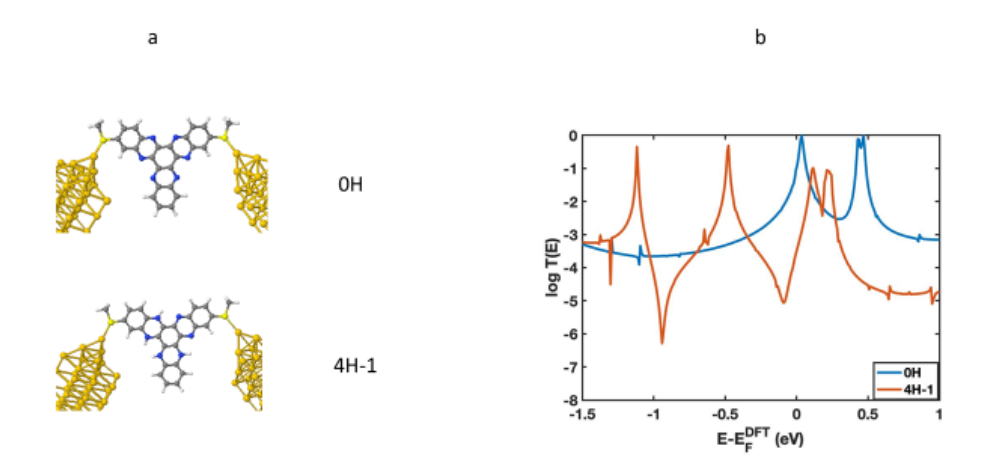


Figure 4.8. (a) the geometries of 0H and 4H-1 within junction. (b) Transmission curves of 0H and 4H-1.

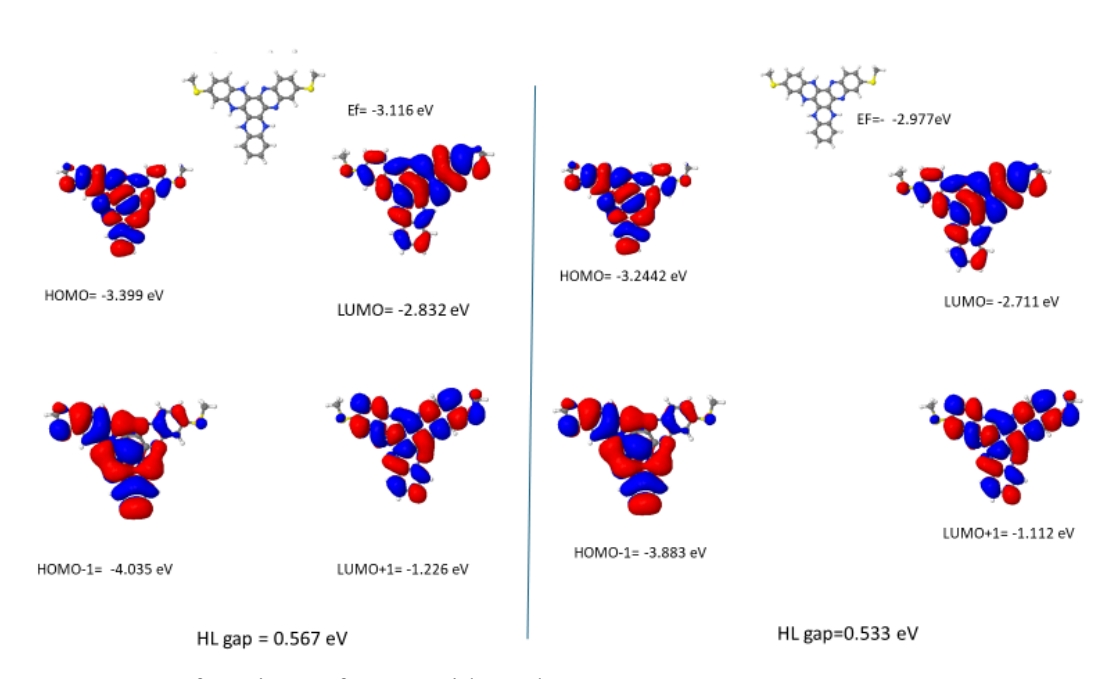


Figure 4.9. Wavefunctions of 4H-1 with anchors.

From Figure 4.8, the red curve in the transmission coefficient on resonance is not equal to 1 because 4H-1 is not a symmetric molecule. In contrast, 0H, is symmetric as mentioned above and therefore its transmission function is equal to 1 on resonance.

Upon adding two hydrogens to OH, the LUMO becomes the HOMO, because two electrons have been added. Similarly for 4H-1, since 4 electrons have been added to the molecular orbitals, the LUMO +1 of OH becomes the HOMO of 4H-1.

Since the HOMO and LUMO products on the left side of Figure 4.9, have the same sign, DQI is predicted. For the right side of this Figure which is with the anchor group, the HOMO and LUMO also have the same signs and DQI is predicted, as is evident in the red curve of Figure 4.8.

I shall now examine the properties of 4H-2, which is shown in Figure 4.10 below.

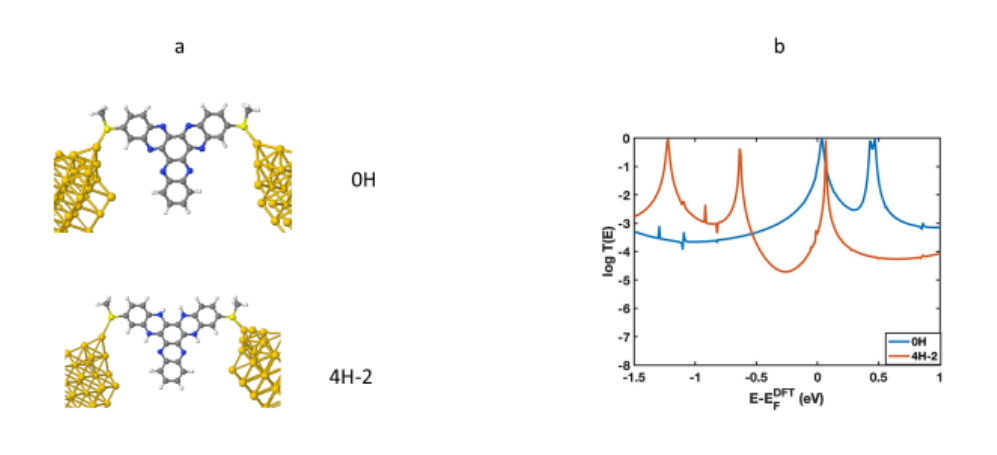


Figure 4.10. (a) the geometries of 0H and 4H-2 within junction. (b) Transmission curves of 0H and 4H-2.

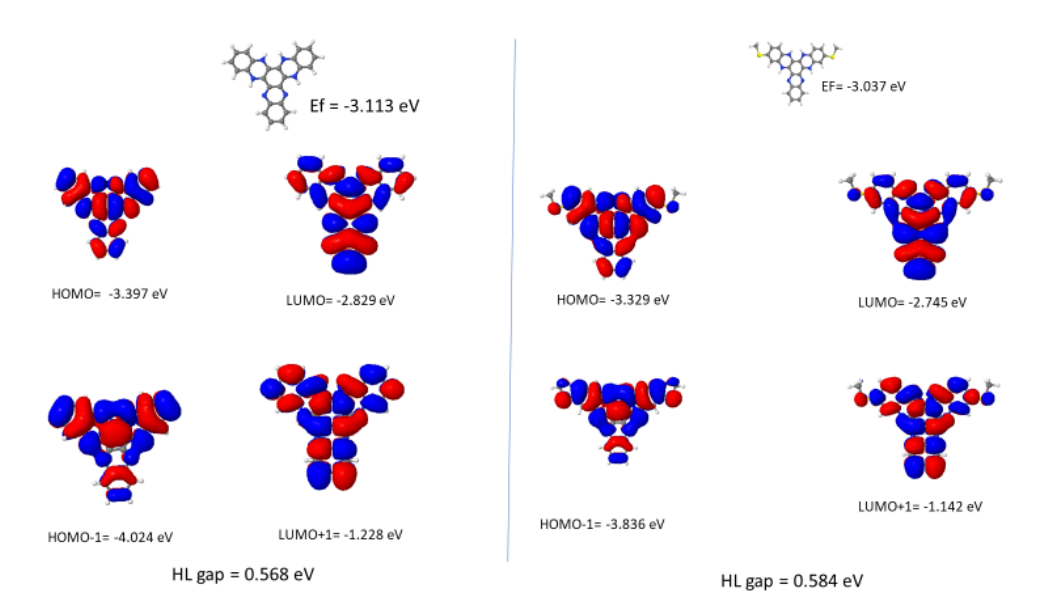


Figure 4.11. Wavefunctions of 4H-2, without and with anchors.

Since both 0H and 4H-2 are symmetric molecules, the red and blue curves in Figure 4.10 reveal that, as expected, the transmission coefficients of both molecules on resonance are equal to 1. Again since 4 electrons are added to the molecular orbitals, so I would expect the LUMO +1 of 0H to become the HOMO of 4H-2.

From Figure 4.11, HOMO and LUMO products have different signs, so the orbital product rule predicts CQI.

Finally, I compared the transport properties of 0H and 6H to investigate the influence of reduction by six hydrogen atoms in two positions.

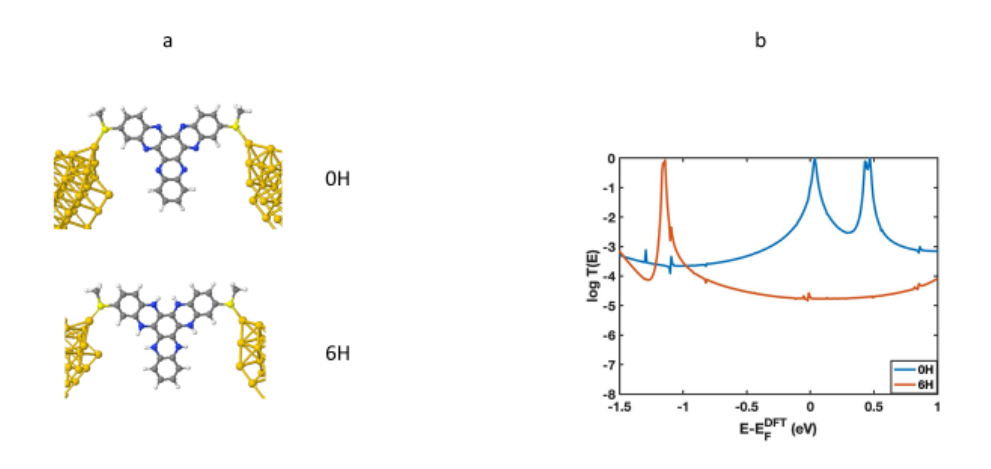


Figure 4.12. (a) the geometries of 0H and 6H within junction. (b) Transmission curves of 0H and 6H.

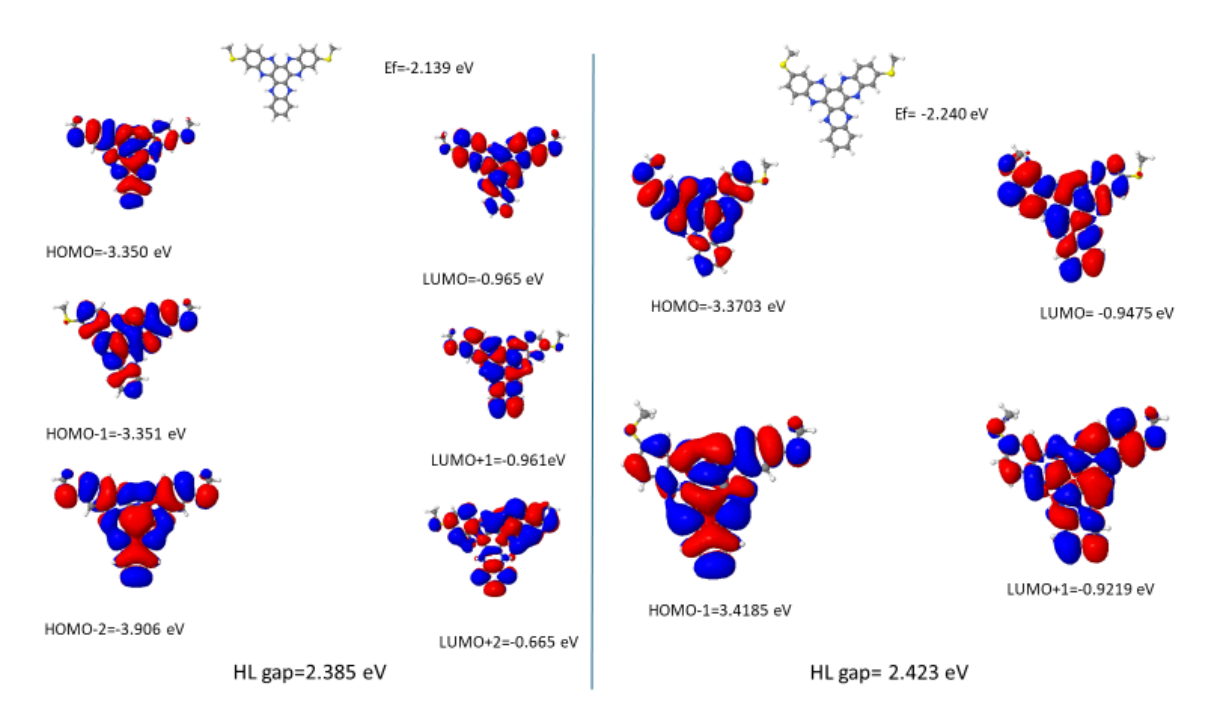


Figure 4.13. wavefunctions of 6H with anchors.

In Figure 4.12, since both molecules are symmetric, both curves possess transmission coefficients reaching 1 on resonance. Furthermore, the orbital products of the HOMO and LUMO have the opposite signs and therefore CQI is predicted. Since 6 electrons have been added, the LUMO

+2 of 0H becomes the HOMO of 6H, the LUMO+1 of 0H becomes the HOMO -1 of 6H, and the LUMO of 0H becomes HOMO -2 of 6H.

Molecular names	Molecules without anchor			Molecules with anchor		
	номо	LUMO	HL gap	номо	LUMO	HL gap
ОН	-5.355	-3.261	2.094	-4.887	-3.058	1.829
2H-1	-3.830	-2.887	0.943	-3.617	-2.797	0.82
2H-2	-3.820	-2.897	0.923	-3.639	-2.726	0.913
4H-1	-3.399	-2.832	0.567	-3.244	-2.711	0.533
4H-2	-3.397	-2.829	0.568	-3.329	-2.745	0.584
6H	-3.350	-0.965	2.385	-3.370	-0.947	2.423

Table 4.1. HOMO LUMO gaps for the molecules mentioned before.

#### 4.7. Conclusions

Ref [1] presented a dynamic molecular switch measuring only 2.4 nm that easily simulate synaptic plasticity, Pavlovian learning, and can be set to perform all logic gates. It was claimed that the dynamic creation of N-H bonds driven by PC-ET drives the switching probability between high and low conduction states. It was suggested that the high conductance state for 2H-1 or 2H-2 was promoted by the presence of a mid-gap state in the middle of the HOMO-LUMO gap of the 0H molecule. Such a state is clearly present in the red curves of Figures 4.6 and 4.3, as indicated by the presence of additional transmission resonances near  $E - E_F = -1eV$ , which are not present in the blue curves. In their description, it is suggested that this state mediates electron hopping through the HATNA core. However, in the single molecule junctions modelled here, symmetry plays a role, which causes the conductance of 2H-1 to be lower than that of 0H, while the conductance of 2H-2 is found to be comparable to that of 0H. In other words, the conductance jump seen in the SAMs of [1] upon adding two hydrogens is not predicted to occur in a single molecule junction. In the SAM-based experiments of [1], the conductance is decreased upon adding 4 or 6 hydrogens and this same behaviour is found in Figures 4.10 and 4.12, where the red curve at the Fermi energy is much lower than the blue curve. This suggests that the strategy of adding or removing hydrogen atoms can lead to large on-off ratios in single-molecule junctions, although up to 6 hydrogens may be needed to achieve attractive on-off ratios. For the future, it would be of interest to see if these predictions for the contrasting behaviour of single molecule junctions can be observed experimentally.

# 4.8. Bibliography

- [1] Y. Wang, Q. Zhang, H. P. A. G. Astier, C. Nickle, S. Soni, F. A. Alami, A. Borrini, Z. Zhang, C. Honnigfort, B. Braunschweig, A. Leocini, D. Cheng Qi, Y, Han, E. del Barco D. Thompson, and C. A. Nijhuis, 'Dynamic molecular switches with hysteretic negative differential conductance emulating synaptic behaviour,' Nature Materials vol. 21, pp. 1403-1411, Dec. 2022
- [2] Y. van de Burgt, A. Melianas, S. T. Keene, G. Malliaras, and A. Salleo, 'Organic electronics for neuromorphic computing', *Nat Electron*, vol. 1, no. 7, pp. 386–397, Jul. 2018, doi: 10.1038/s41928-018-0103-3.
- [3] J. Zhu, T. Zhang, Y. Yang, and R. Huang, 'A comprehensive review on emerging artificial neuromorphic devices', *Applied Physics Reviews*, vol. 7, no. 1, p. 011312, Feb. 2020, doi: 10.1063/1.5118217.
- [4] N. K. Upadhyay, H. Jiang, Z. Wang, S. Asapu, Q. Xia, and J. Joshua Yang, 'Emerging Memory Devices for Neuromorphic Computing', *Advanced Materials Technologies*, vol. 4, no. 4, p. 1800589, Apr. 2019, doi: 10.1002/admt.201800589.
- [5] S. T. Keene, C. Lubrano, S. Kazemzadeh, A. Melianas, Y. Tuchman, G. Polino, P. Scognamiglio, L.Cina, A. Salleo, Y. van de Burgt, and F. Santoro, 'A biohybrid synapse with neurotransmitter-mediated plasticity', *Nat. Mater.*, vol. 19, no. 9, pp. 969–973, Sep. 2020, doi: 10.1038/s41563-020-0703-y.
- [6] S. Oh, H. Hwang, and I. K. Yoo, 'Ferroelectric materials for neuromorphic computing', *APL Materials*, vol. 7, p. 091109, Sep. 2019, doi: 10.1063/1.5108562.

- [7] L. Wang, S.-R. Lu, and J. Wen, 'Recent Advances on Neuromorphic Systems Using Phase-Change Materials', *Nanoscale Res Lett*, vol. 12, no. 1, p. 347, May 2017, doi: 10.1186/s11671-017-2114-9.
- [8] Q. Wan, M. T. Sharbati, J. R. Erickson, Y. Du, and F. Xiong, 'Emerging Artificial Synaptic Devices for Neuromorphic Computing', *Advanced Materials Technologies*, vol. 4, no. 4, p. 1900037, Apr. 2019, doi: 10.1002/admt.201900037.
- [9] W. Xu, S.-Y. Min, H. Hwang, and T.-W. Lee, 'Organic core-sheath nanowire artificial synapses with femtojoule energy consumption', *Sci Adv*, vol. 2, no. 6, p. e1501326, Jun. 2016, doi: 10.1126/sciadv.1501326.
- [10] I. Ratera and J. Veciana, 'Playing with organic radicals as building blocks for functional molecular materials', *Chem. Soc. Rev.*, vol. 41, no. 1, pp. 303–349, 2012, doi: 10.1039/C1CS15165G.
- [11] R. Klajn, 'Spiropyran-based dynamic materials', *Chemical Society Reviews*, vol. 43, no. 1, pp. 148–184, 2014, doi: 10.1039/C3CS60181A.
- [12] D. Bléger and S. Hecht, 'Visible-Light-Activated Molecular Switches', *Angew Chem Int Ed Engl*, vol. 54, no. 39, pp. 11338–11349, Sep. 2015, doi: 10.1002/anie.201500628.
- [13] A. Sorrenti, J. Leira-Iglesias, A. J. Markvoort, T. F. A. de Greef, and T. M. Hermans, 'Non-equilibrium supramolecular polymerization', *Chem. Soc. Rev.*, vol. 46, no. 18, pp. 5476–5490, Sep. 2017, doi: 10.1039/C7CS00121E.
- [14] S. A. P. van Rossum, M. Tena-Solsona, J. H. van Esch, R. Eelkema, and J. Boekhoven, 'Dissipative out-of-equilibrium assembly of man-made supramolecular materials', *Chem. Soc. Rev.*, vol. 46, no. 18, pp. 5519–5535, Sep. 2017, doi: 10.1039/C7CS00246G.
- [15] M. F. Bear, B. W. Connors, and M. A. Paradiso, *Neuroscience: Exploring the Brain*. Wolters Kluwer, 2016.

- [16] J. C. Eccles and A. K. McIntyre, 'Plasticity of Mammalian Monosynaptic Reflexes', *Nature*, vol. 167, no. 4247, pp. 466–468, Mar. 1951, doi: 10.1038/167466a0.
- [17] J. L. Segura, R. Juárez, M. Ramos, and C. Seoane, 'Hexaazatriphenylene (HAT) derivatives: from synthesis to molecular design, self-organization and device applications', *Chem. Soc. Rev.*, vol. 44, no. 19, pp. 6850–6885, Sep. 2015, doi: 10.1039/C5CS00181A.
- [18] R. Wang, T. Okajima, F. Kitamura, N. Matsumoto, T. Thiemann, S. Mataka, and T. Ohsaka 'Cyclic and normal pulse voltammetric studies of 2,3,6,7,10,11-hexaphenylhexazatriphenylene using a benzonitrile thin layer-coated glassy carbon electrode', *Journal of Physical Chemistry B*, vol. 107, no. 35, pp. 9452–9458, Sep. 2003, doi: 10.1021/jp0305281.
- [19] M. L. Perrin, R. Frisenda, M. Koole, J. S. Seldenthuis, J. A. Celis Gil, H.Valkenier, J. C. Hummelen, N. Renaud, F. C. Grozema, J. M. Thijssen, D. Dulic, and H. S. J. van der Zant, 'Large negative differential conductance in single-molecule break junctions', *Nat Nanotechnol*, vol. 9, no. 10, pp. 830–834, Oct. 2014, doi: 10.1038/nnano.2014.177.
- [20] A. Migliore and A. Nitzan, 'Irreversibility and Hysteresis in Redox Molecular Conduction Junctions', *J. Am. Chem. Soc.*, vol. 135, no. 25, pp. 9420–9432, Jun. 2013, doi: 10.1021/ja401336u.
- [21] F. Schwarz, G. Kastlunger, F. Lissel, C. Egler-Lucas, S. N. Semenov, K. Venkatesan, H. Berke, R. Stadler, and E. Lortscher, 'Field-induced conductance switching by charge-state alternation in organometallic single-molecule junctions', *Nature Nanotech*, vol. 11, no. 2, pp. 170–176, Feb. 2016, doi: 10.1038/nnano.2015.255.
- [22] A. R. Garrigues, L. Yuan, L. Wang, E. R. Mucciolo, D. Thompon, E. Del Barco, and C.A. Nijhuis, 'A Single-Level Tunnel Model to Account for Electrical Transport through

- Single Molecule- and Self-Assembled Monolayer-based Junctions', *Sci Rep*, vol. 6, no. 1, p. 26517, May 2016, doi: 10.1038/srep26517.
- [23] A. Aukauloo, 'Proton-Coupled Electron Transfer. A Carrefour of Chemical Reactivity Traditions. RSC Catalysis Series. Edited by Sebastião Formosinho and Mónica Barroso.', *Angewandte Chemie International Edition*, vol. 51, Sep. 2012, doi: 10.1002/anie.201205397.
- [24] A. Migliore, N. F. Polizzi, M. J. Therien, and D. N. Beratan, 'Biochemistry and Theory of Proton-Coupled Electron Transfer', *Chem. Rev.*, vol. 114, no. 7, pp. 3381–3465, Apr. 2014, doi: 10.1021/cr4006654.
- [25] J. M. Mayer, 'Understanding hydrogen atom transfer: from bond strengths to Marcus theory', *Acc Chem Res*, vol. 44, no. 1, pp. 36–46, Jan. 2011, doi: 10.1021/ar100093z.
- [26] S. Kim, C. Du, P. Sheridan, W. Ma, S. Choi, and W. D. Lu, 'Experimental Demonstration of a Second-Order Memristor and Its Ability to Biorealistically Implement Synaptic Plasticity', *Nano Lett.*, vol. 15, no. 3, pp. 2203–2211, Mar. 2015, doi: 10.1021/acs.nanolett.5b00697.
- [27] Z. Wang, S. Joshi, S. E. Savel'ev, H. Jiang, R.Midya, P. Lin, M. Hu, N. Ge, J. Paul Strachan, Z. Li, Q,Wu, M. Barnell, G. Lin Li, H. L. Xin, R. Stanley Williams, Q. Xia, and J. Joshua Yang, 'Memristors with diffusive dynamics as synaptic emulators for neuromorphic computing', *Nature Mater*, vol. 16, no. 1, pp. 101–108, Jan. 2017, doi: 10.1038/nmat4756.
- [28] N. J. Smelser and P. B. Baltes, Eds., *International Encyclopedia of the Social and Behavioral Sciences*. Elsevier, 2001.
- [29] Y. van de Burgt, E. Lubberman, E. J. Fuller, S. T. Keene, G. C. Faria, S. Agarwal, M. J. Marinella, A. A. Talin, and A. Salleo, 'A non-volatile organic electrochemical device as a low-voltage artificial synapse for neuromorphic computing', *Nature Mater*, vol. 16, no. 4, pp. 414–418, Apr. 2017, doi: 10.1038/nmat4856.

- [30] H.-C. Ruiz Euler, M. N. Boon, J. T. Wildeboer, B. van de Ven, T. Chen, H. Broersma, P. A. Bobbert, and W. G. van der Wiel, 'A deep-learning approach to realizing functionality in nanoelectronic devices', *Nat. Nanotechnol.*, vol. 15, no. 12, pp. 992–998, Dec. 2020, doi: 10.1038/s41565-020-00779-y.
- [31] M. Kathan, F. Eisenreich, C. Jurissek, A. Dallmann, J. Gurke, and S. Hecht, 'Light-driven molecular trap enables bidirectional manipulation of dynamic covalent systems', *Nat Chem*, vol. 10, no. 10, pp. 1031–1036, Oct. 2018, doi: 10.1038/s41557-018-0106-8.
- [32] P. Chakma and D. Konkolewicz, 'Dynamic Covalent Bonds in Polymeric Materials', *Angew Chem Int Ed Engl*, vol. 58, no. 29, pp. 9682–9695, Jul. 2019, doi: 10.1002/anie.201813525.
- [33] B. J. Cafferty, A. S. Y. Wong, S. N. Semenov, L. Belding, S. Gmur, W. T. S. Huck, and G. Whitesides, 'Robustness, Entrainment, and Hybridization in Dissipative Molecular Networks, and the Origin of Life', *J Am Chem Soc*, vol. 141, no. 20, pp. 8289–8295, May 2019, doi: 10.1021/jacs.9b02554.
- [34] G. Ashkenasy, T. M. Hermans, S. Otto, and A. F. Taylor, 'Systems chemistry', *Chem. Soc. Rev.*, vol. 46, no. 9, pp. 2543–2554, May 2017, doi: 10.1039/C7CS00117G.

# Chapter 5

### Single-Molecule Conductance Enhancement in Stable Diradical Molecules

#### 5.1. Introduction

In this chapter, I further pursue the strategy of using the attachment or detachment of hydrogen atoms to switch the electrical conductance of single molecule. However, in contrast with the molecules of chapter 4, I consider molecules which form diradicals when hydrogen atoms are removed. Stable organic radicals are gaining attention, because of their special electrical features, especially their half-filled orbitals that are near the Fermi energy. These features make them attractive options for electronic device applications, because organic radicals can increase electrical conductivity. The thiophene fused dimer core, which has a skeleton with many substituent sites that can be tuned for optical, electrical, and spin properties, provides a perfect platform to make stable radicals. The following study aims to examine the charge transport features of a series of such thiophene dimer derivatives, with a special emphasis on stable radicals. The potential of radicals in single-molecule electronics and other functional devices is being realized, and this research is seen as a major step in that direction. Quantum interference provides an additional dimension to manipulate electron transport through molecules, including constructive quantum interference (CQI) and destructive quantum interference (DQI). As highlighted by magic number theory, depending on connectivity, CQI can lead to difference conductances within one molecule. In this chapter, two difference CQIs are discussed based on the thiophene dimers shown in Figures 5.1 and 5.2, denoted CQI-H and CQI-L, corresponding to displays of CQI with higher conductance and lower conductance respectively. In what follows, the effect of diradicals on the conductance of CQI-H and CQI-L is studied using DFT combined with GOLLUM.

# 5.2. Studied molecules

The following molecules will be investigated. As indicated in the figures, these form series of related molecules, which may exhibit either CQI-L and CQI-H and which may be either neutral molecules or neutral radicals. The latter are created by removing two hydrogen atoms from the two OH groups shown below.

Figure 5.1: Studied diradical molecules and their corresponding neutral molecules. (CQI-H-radical -CQI-H-singlet-CQI-H-triplet).

When the above molecules are placed between gold electrodes to form a single-molecule junction, they attach to the electrodes via the thio-methyl groups (coloured blue as a guide to the eye). In what follows, their transport properties will be compared with those of the molecules below, which have

alternative connectivities to electrodes.

The CQI-H radical is a very unstable chemical that has an unpaired electron. There are two states in which it can exist:

Singlet molecules: There is no net spin in the molecule and all of the electrons are coupled.

Triplet molecules: The molecule has a net spin of one due to the parallel spins of two unpaired electrons.

These conditions have an impact on the radical's actions and responses. Triplet states, particularly in processes involving light, can result in distinct reactions, although singlet states often have lower energies.

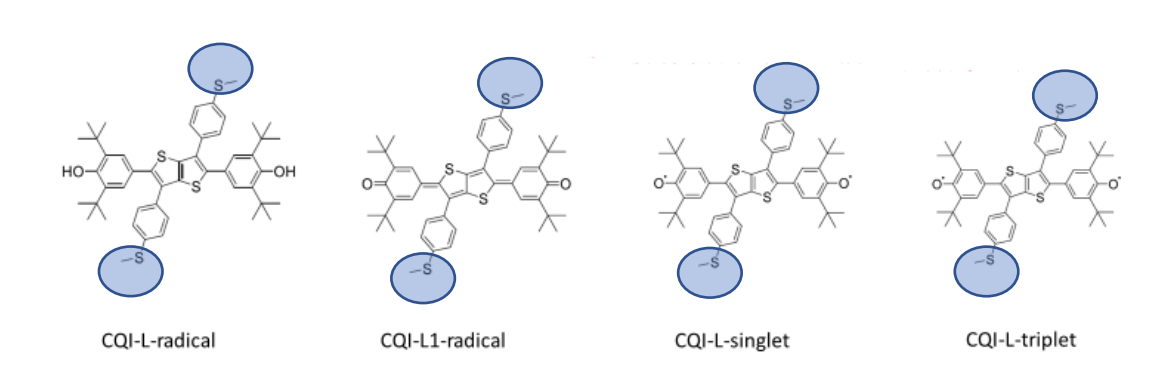


Figure 5.2: Studied diradical molecules and their corresponding neutral molecules. (CQI-L-radical-CQI-L1-radical-CQI-L-triplet).

For both sets of molecules, they could adopt singlet or triplet spins configurations. The potential spin occupancies for the diradicals are shown below.

These compounds contain hydroxyl and sulphur groups in various electronic states:

They include radical forms, which are typically very reactive and have unpaired electrons.

The singlet state has paired electrons, which increases the molecule's stability.

The triplet state contains unpaired electrons, which makes the molecule more reactive.

In general, the figure shows different forms of comparable sulfur-containing compounds in a range of energy states.

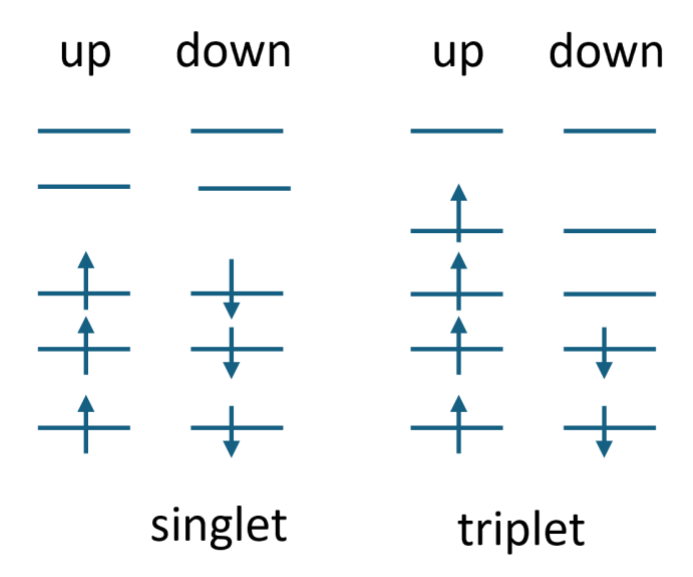


Figure 5.3: Schematic shows two spin states for diradical molecules.

According to this graphic, an atom or molecular system's energy levels and state transitions are represented.

The notations "down" and "up" are likely to correspond to electron spin orientations (spin-down and spin-up), whereas "singlet" and "triplet" indicate specific spin states determined by electron pairing.

This graphic shows the energy hierarchy and potential transitions between singlet and triplet states, emphasising the ways in which electrons might change between these states according on energy considerations and spin orientations.

#### 5.3. Results and discussion

# Case 1: CQI-H

As shown in Figure 5.9, the HOMO and LUMO products of CQI-neutral have t different signs and therefore CQI is predicted. This is further confirmed by the transmission function indicated by the blue curve in Figure 5.4b, where no dip appears inside the HOMO-LUMO gap as. In terms of its diradical counterpart, the two unpaired electrons sitting on the two oxygen atoms can have the same spin or different spins, namely, they can be singlets or triplets as shown in Figure 5.3. These two cases are therefore considered in this chapter. The transmission coefficient of the singlet case is also plotted in Figure 5.4b, with spin up and spin down channels almost identical due to the symmetric character of this molecule. The two peaks near the Fermi level correspond to the SOMO (singly occupied molecular orbital) and the SUMO (singly unoccupied molecular orbital) respectively. The room temperature conductance is plotted in Figure 5.5, which shows an increased conductance compared with its neutral counterpart near the Fermi energy. I further carried on the calculation with a triplet spin state and plot the transmission curves in Figure 5.6. The two unpaired electrons on oxygens occupy the two energy levels indicated by the two red peak below Fermi energy. Figure 5.7 shows that a bigger conductance enhancement is observed, due to the presence of more resonances near the Fermi energy. The spin densities of the singlet and triplet diradicals within junctions are displayed in Figure 5.8, where the spin up and spin down are indicated by red and blue respectively.

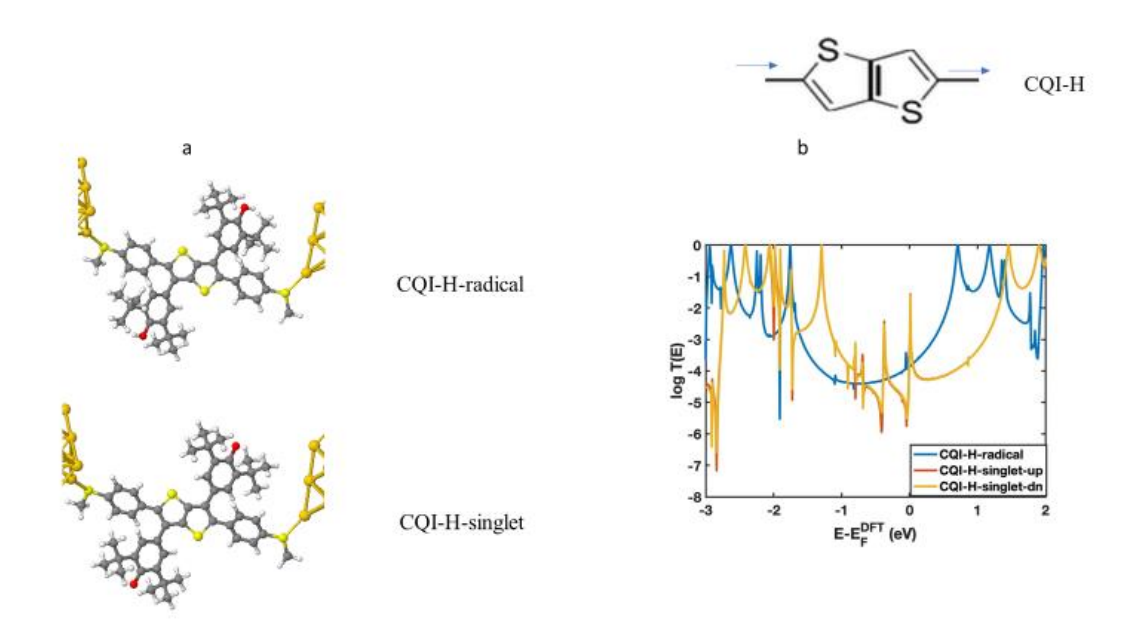
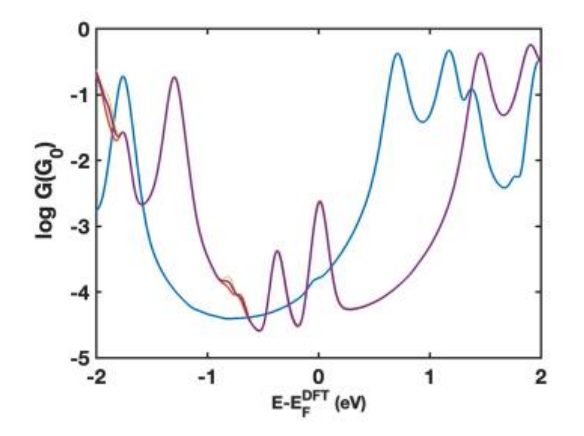


Figure 5.4: (a) the geometries of CQI-H-radical and CQI-H-singlet within junction. (b)their transmission curves.

The Figure shows how different energy levels in the system are related and how easily electrons can travel through at various energies. The transmission curves indicate the areas where electrons can move easily, while the connection curves show the relationships between states. They work together to help understand the electronic behaviour of the system.



Comparison of conductance $\text{Log } G/G_0$				
CQI-H-radical	CQI-H-singlet			
-3.7	-2.6			

Figure 5.5: CQI-H-radical and CQI-H-singlet room temperature conductance for stable radical where the purple one is the average of spin up and spin down transmission.

This figure compares the logarithmic conductance (log G/Go) of various molecule structures, particularly through molecular mechanics and E-DFT (Density Functional Theory extended) computations. This graphic shows the simplicity of the electrical conductivity of several substances. It demonstrates that the energy state and structure of the molecule determine its conductance, with radicals and singlet states showing different conductance values.

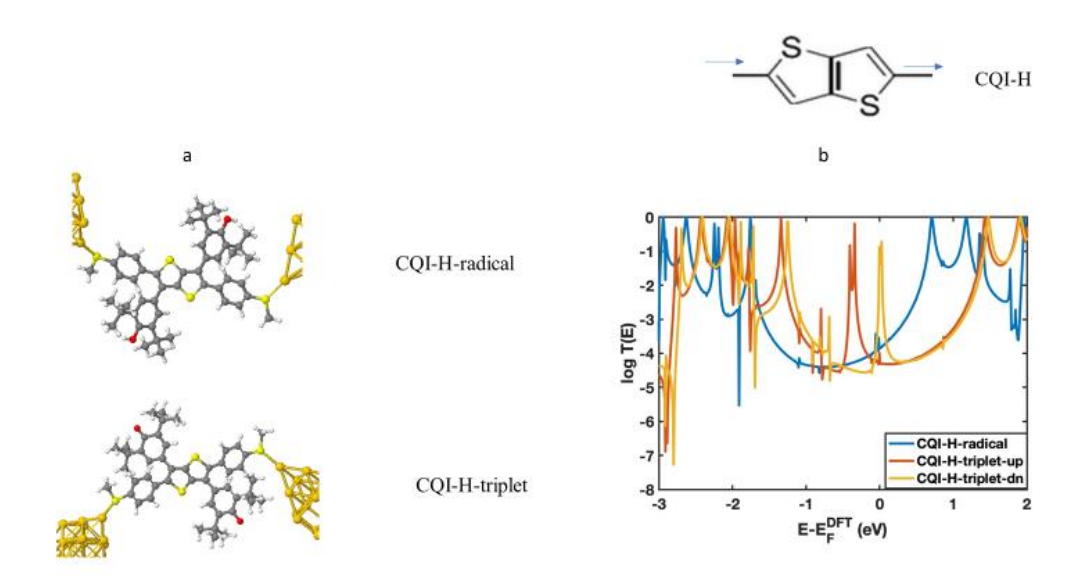
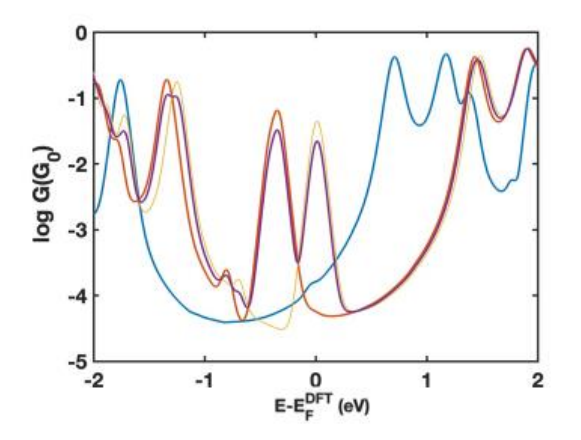


Figure 5.6: (a) the geometries of CQI-H-radical and CQI-H-triplet within junction. (b) their transmission curves.

This graphic shows how the different spin and radical configurations occupy distinct places across the energy spectrum, as well as the relative energies of these states.

It helps in understanding the stability, electronic transitions, and excited-state characteristics of CQI-H.



1.00	of conductance $g G/G_0$
CQI-H-radical	CQI-H-triplet
-3.7	-1.5

Figure 5.7: CQI-H-radical and CQI-H-triplet room temperature conductance for stable radical which the purple one is the average of spin-up and spin-down transmission.

This chart compares the electrical conductance (log G/Go) of various molecular states or configurations. The horizontal axis indicates energy in electron volts (eV), while the vertical axis shows the logarithm of the conductance ratio (log G/Go).

The CQI-H-radical has a significantly lower conductance value (about -3.7) than the CQI-H-triplet (around -1.5). Negative values indicate that the conductance is lower relative to the reference conductance (Go), with considerable changes depending on whether the molecule is in a radical or triplet state.

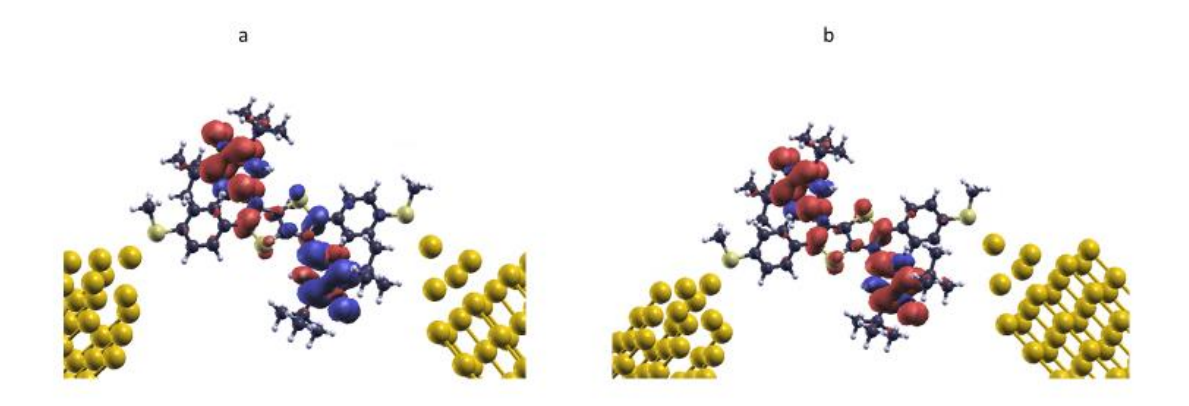


Figure 5.8: (a) the spin density for CQI-H-singlet within a junction. (b) the spin density for CQI-H-triplet within a junction.

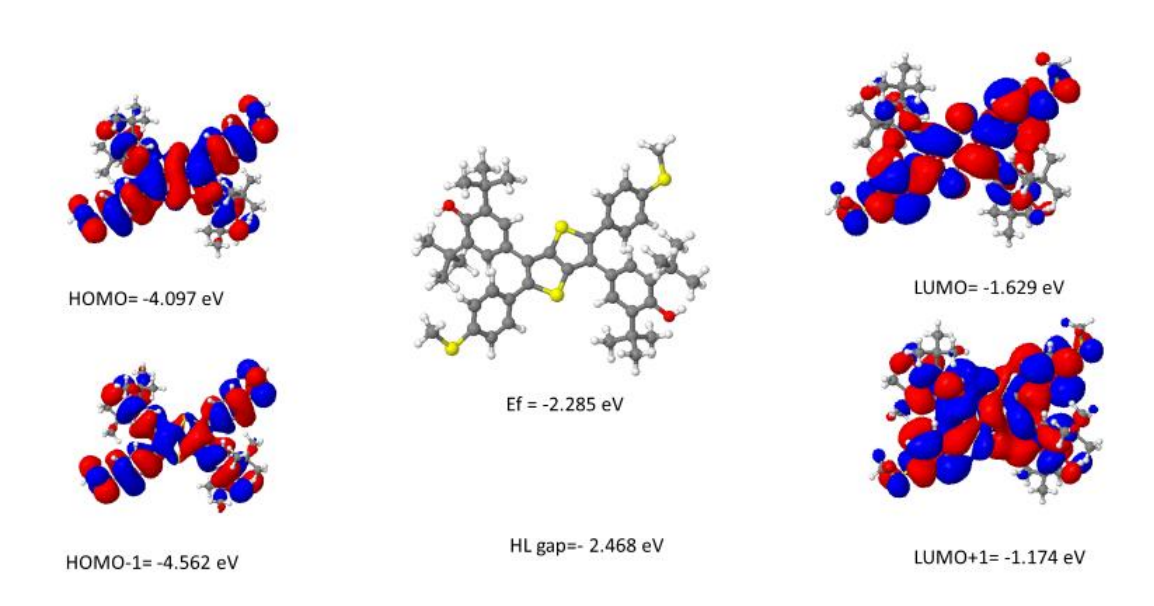


Figure 5.9: Frontier molecular orbitals of CQI-H-radical studied molecule with its eigenvalues obtained from DFT, where red represents positive and blue indicates negative regions of the wave functions.

Figure 5.9 shows that the orbital products of the HOMO and LUMO of CQI-H-radical have opposite signs and so the CQI is predicted.

The spatial distribution of electrons is defined by wavefunctions that correspond to HOMO, LUMO, and other orbitals. These distributions affect the molecule's interactions with light, other compounds, and electric fields. Indicating the energy of the highest occupied electrons is the HOMO level at -4.097 eV. The energy at which electrons can be excited is indicated by the LUMO at -1.629 eV. The HOMO-LUMO gap of 2.468 eV represents the energy required for electronic excitation.

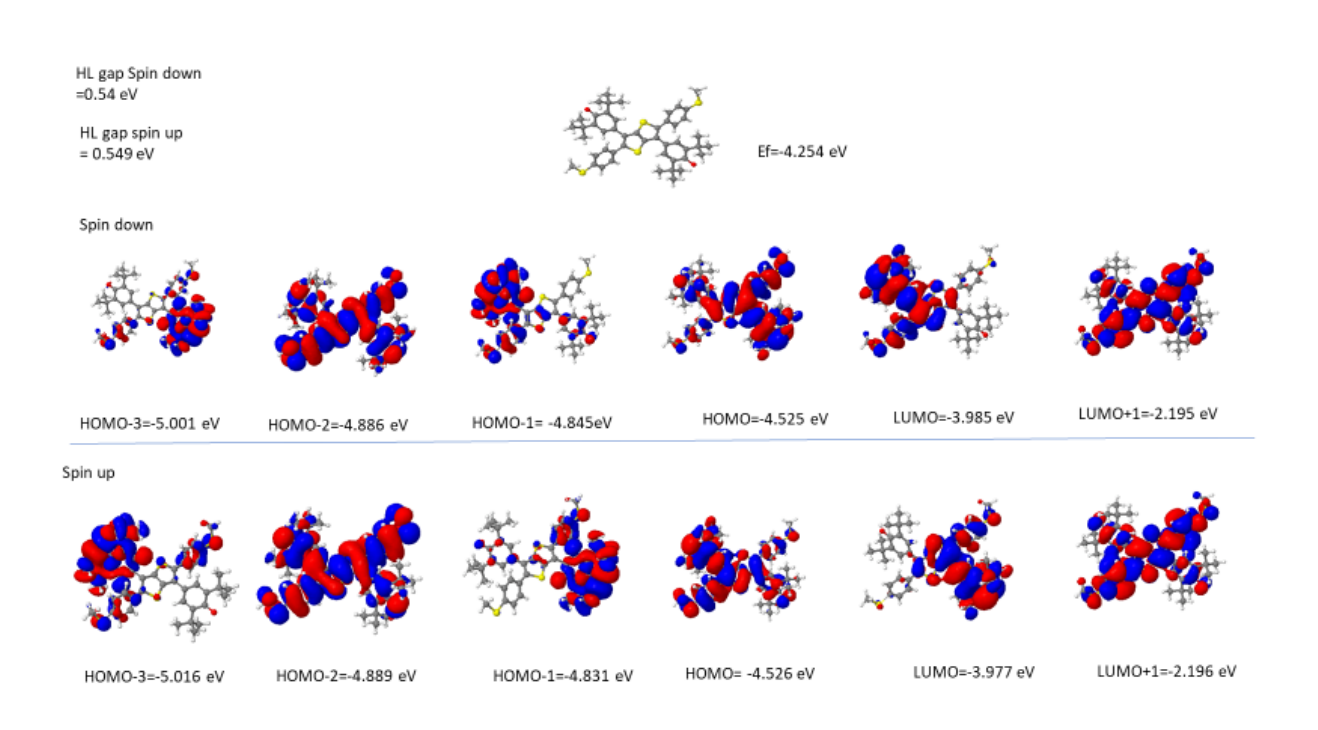


Figure 5.10: Frontier molecular orbitals of CQI-H-singlet studied molecule with its eigenvalues.

Figure 5.10 shows the frontier molecular orbitals of the CQI-H-singlet diradical molecule, along with its eigenvalues. In this case, the amplitude of the spin up and spin down LUMOs are negligibly small on at least one end of the molecule, and therefore, the product rule cannot be applied.

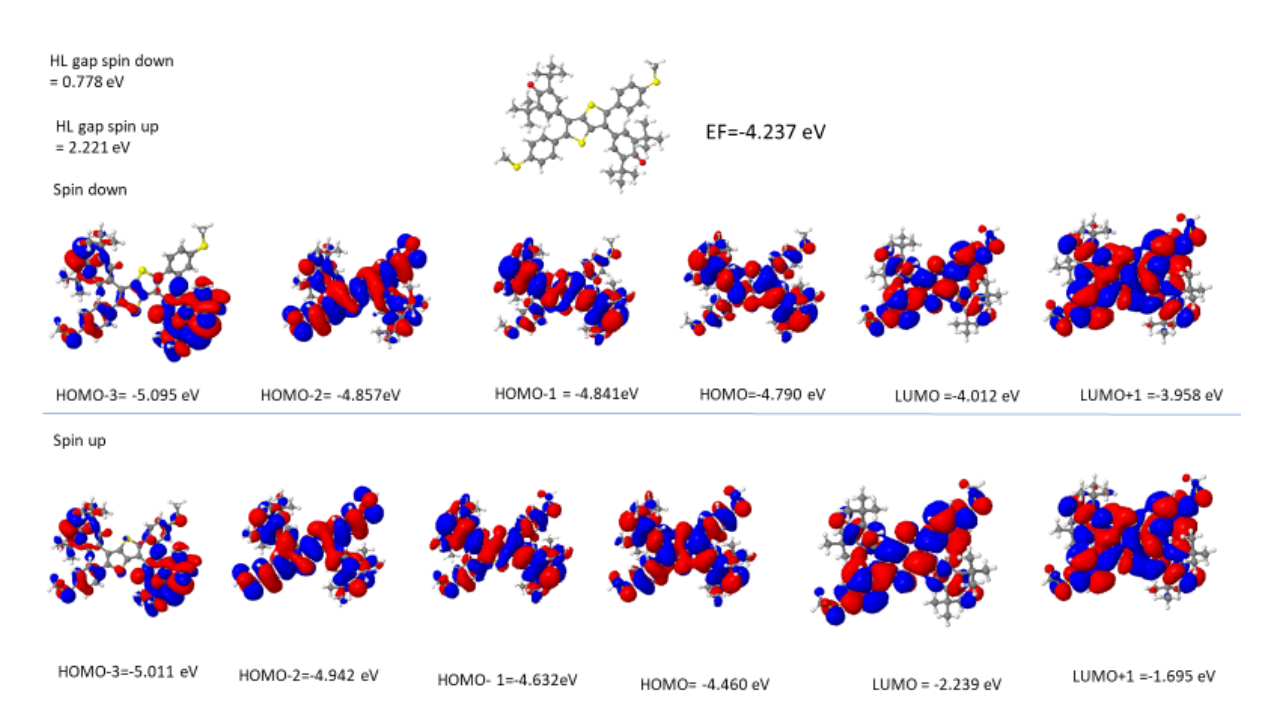


Figure 5.11: Frontier molecular orbitals of the CQI-H-triplet studied molecule with its eigenvalues

Figure 5.11 shows the frontier molecular orbitals of the CQI-H-triplet diradical, along with its eigenvalues. In this case, the orbital products of the HOMOs and LUMOs of both the up and down spins have opposite signs and therefore the product rule predicts CQI for the spin-up and down transmission functions.

# Case 2: CQI-L

In this section, the molecules with alternative connectivities shown in Figure 5.2 are studied. For CQI-L, as shown in Figure 5.18, the HOMO and LUMO products have different signs and therefore the product rule predicts CQI. The transmission functions for this molecule and for the non-radical CQI-L1-radical are plotted as the blue and brown curves in Figure 5.12(b). Clearly CQI-L1-radical is predicted to have a significantly higher conductance than CQI-H-radical. In the case of the diradical counterpart, the two unpaired electrons sitting on the two oxygen atoms can have the same spin or different spins, namely, they can be singlets or triplets as shown in Figure 5.3. The transmission coefficient of the singlet case is plotted in Figure 5.14b, with spin up and spin down channels almost identical due to the symmetric character of this molecule. The room temperature conductance is plotted in Figure 5.15, which shows an increased conductance compared with its radical counterpart near the Fermi energy. I carried out the calculation for a triplet spin state and plotted the transmission curves in Figure 5.16(b). The two unpaired electrons on oxygens occupy the two energy levels indicated by the two red peaks around Fermi energy. A bigger conductance enhancement is observed due to more resonances near Fermi energy.

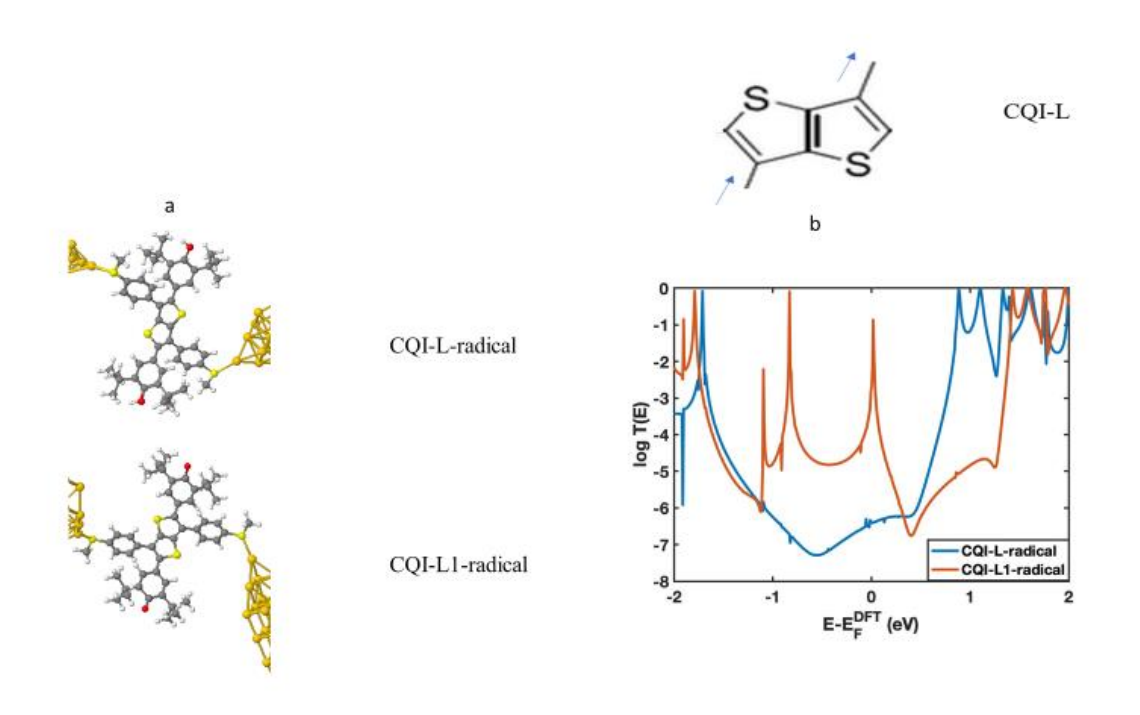


Figure 5.12:(a) the geometries of CQI-L-radical and CQI-L1-radical within junction. (b) their transmission curves.

This Figure shows a comparison of the electronic energy levels and characteristics of two radicals, CQI-L and CQI-L1. The energy values are displayed in electron volts (eV) to demonstrate the changes in electronic states. The data contains particular energy points for each radical, demonstrating how their electronic structures change, which might affect their chemical reactivity and stability. The figure probably highlights the impact of various computational techniques, such E-EDFT, in determining these energy levels, offering information about the electrical properties of these radical species.

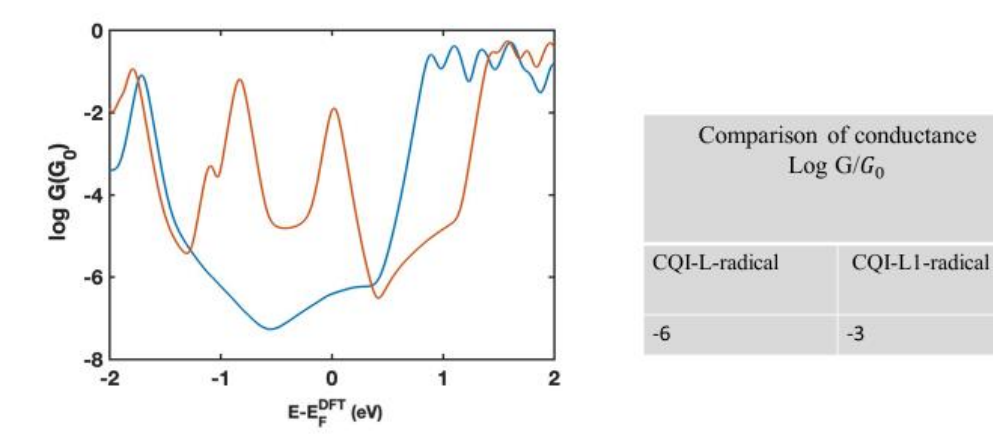


Figure 5.13: CQI-L-radical (blue curve) and CQI-L1-radical (red curve) room temperature conductance for stable radical.

This Figure shows how the conductance (ability to conduct electricity) of various radical molecules changes according to their energy level. As energy increases, conductance decreases, implying that particular molecules conduct better at specific energies. It utilises a particular calculating approach known as E-EDFT to compare various radicals and how their electronic structures affect their capacity to conduct electricity.

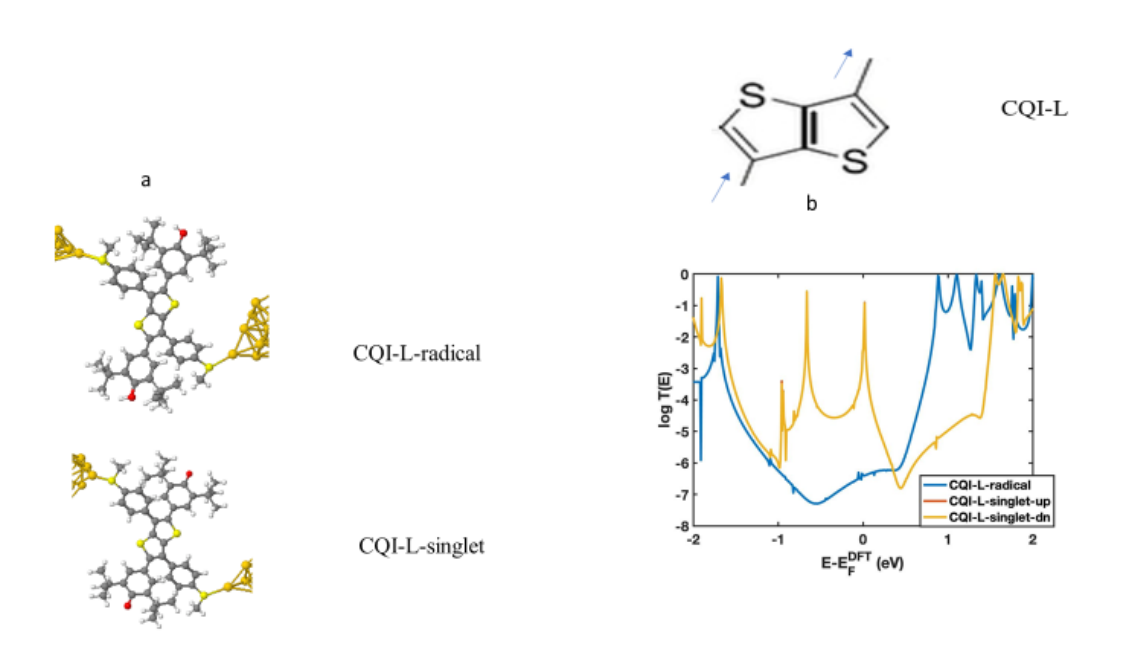
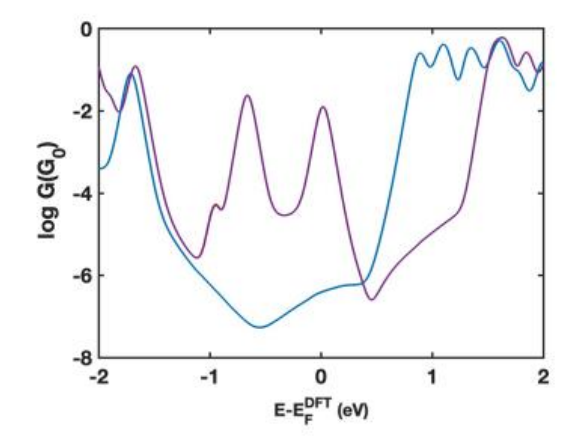


Figure 5.14:(a) the geometries of CQI-L-radical and CQI-L-singlet within junction. (b) their transmission curves.

Increased conductance occurs when molecular states become energetically suitable for electron tunnelling, such as when energy levels approach the Fermi level.

Conductance decreases occur as these states move away or energy gaps expand, restricting electron movement.



Comparison of conductance $\operatorname{Log} G/G_0$	
CQI-L-radical	CQI-L -singlet
-6	-4

Figure 5.15: CQI-L-radical (blue curve) and CQI-L-singlet (purple curve) room temperature conductance.

This Figure compares the conductance (measured as log G/Go) for two different states: the radical state and the singlet state. The graph shows how conductance increases with energy (in eV). It indicates that conductance changes depending on the state, with significant differences between the radical and singlet states over the energy range.

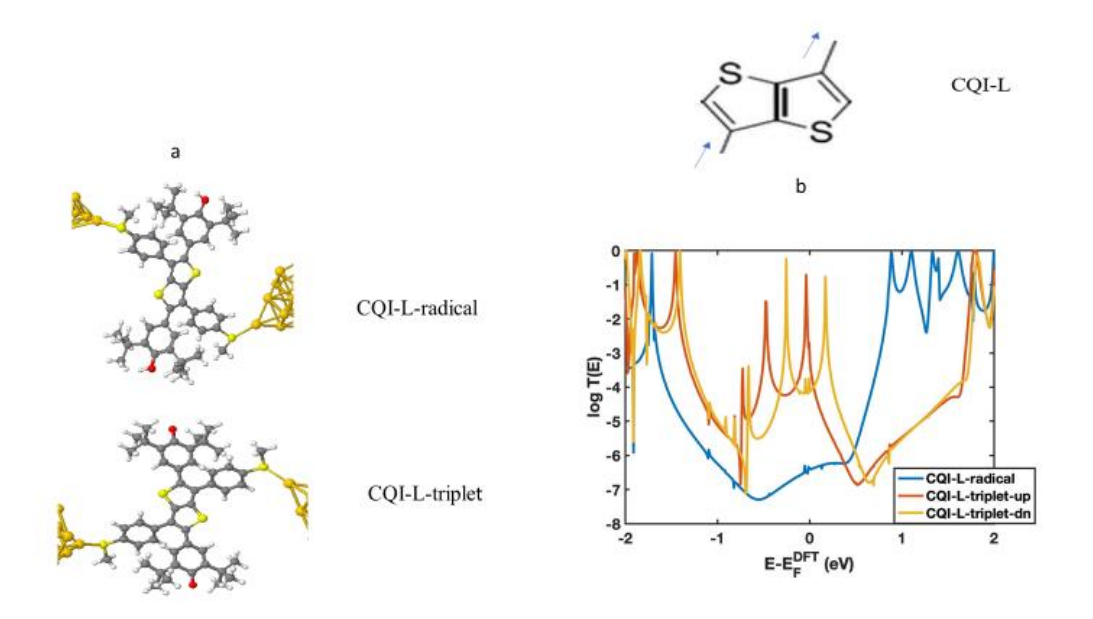
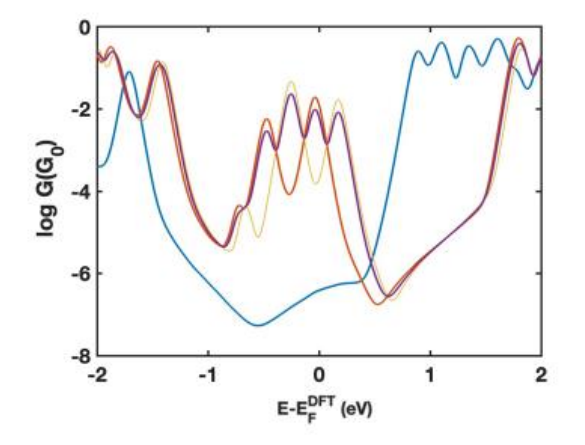


Figure 5.16:(a) the geometries of CQI-L-radical and CQI-L-triplet within junction. (b) their transmission curves.

CQI-L-radical: A radical state that often has an unpaired electron, making it reactive and important in electron transfer activities. CQI-L-triplet-up and CQI-L-triplet-down are triplet states with two unpaired electrons and parallel spins ("up" and "down" states).

The transition between different states (such as from CQI-L-radical to triplet states) and their corresponding energies affect the conductance in the figure. When building molecular electronic components, the system's conductance—whether high or low—is determined by its arrangement and energy alignment.



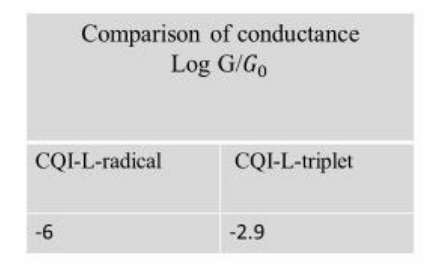
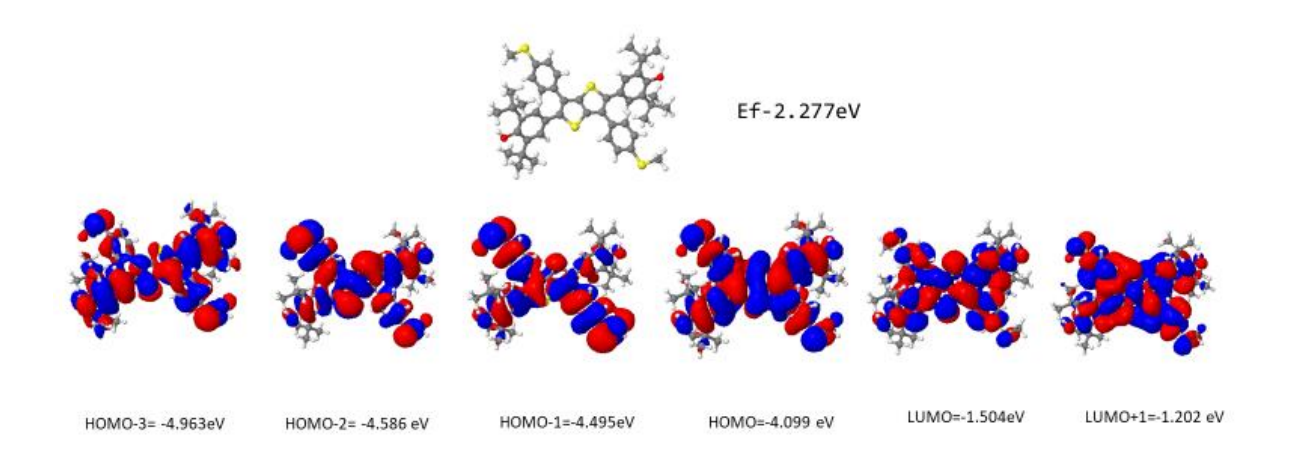


Figure 5.17: CQI-L-radical and CQI-L-triplet room temperature conductance for the stable diradical.

The purple curve of the diradical is an average of spin-up and spin-down conductance.

The electrical conductance, represented by the log of G divided by G<sub>0</sub> (log G/G<sub>0</sub>), is compared for different states or configurations in this Figure. The conductance value of the CQI-L-radical is about -6, and the conductance value of the CQI-L-triplet is about -2.9. This shows that the conductivity in the radical state is much lower than that in the triplet state. The difference indicates that the radical reduces conductance, most likely due to shifts in spin or electrical structure between the radical and triplet forms.



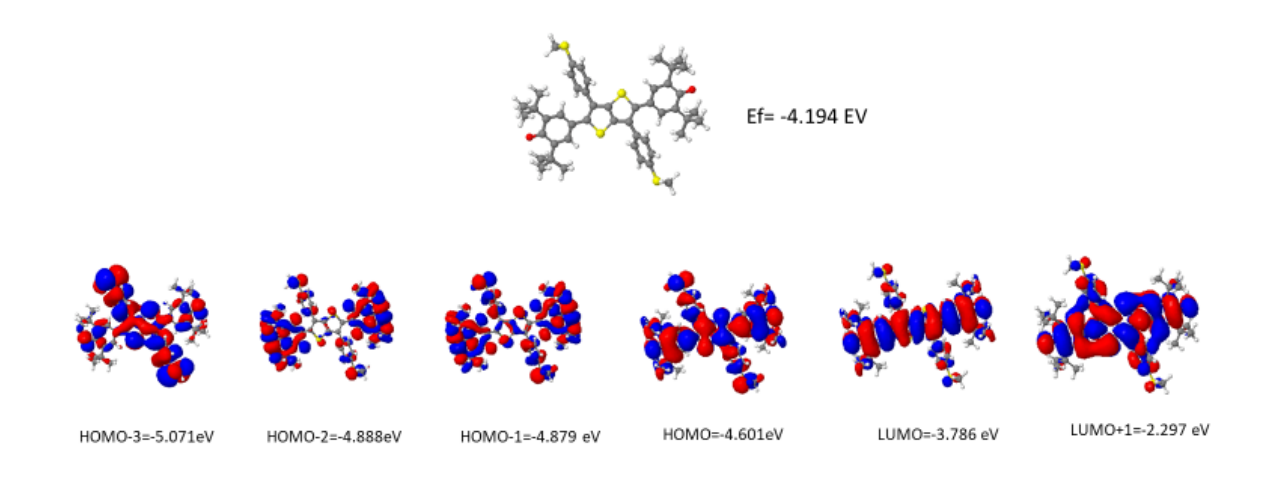
HL gap =2.5 eV

Figure 5.18: Frontier molecular orbitals of CQI-L-radical studied molecule with its eigenvalues.

The orbital ends of HOMO and LUMO have the opposite signs as shown in Figure 5.18, so CQI is predicted.

HOMO The wavefunction represents the highest energy molecular orbital containing electrons at ground state. Its wavefunction has a certain symmetry and distribution of electron density, which determines how the molecule contributes electrons during chemical reactions.

The LUMO wavefunction represents the lowest energy, unoccupied molecular orbital. Its wavefunction tells where the molecule is most likely to take electrons, which influences its ability to perform specific reactions or excitations.



HL gap= 0.815 eV

Figure 5.19: Frontier molecular orbitals of CQI-L1- radical studied molecule with its eigenvalues.

The two ends of the above HOMOs and LUMOs have different signs and therefore the product rule predicts CQI.

The HOMO and LUMO wavefunctions represent the spatial distribution of electrons in those orbitals, providing information about the molecule's electrical behaviour, reactivity, and optical features.

The HOMO wavefunction indicates the location of electrons with the maximum energy.

The LUMO wavefunction indicates where electrons would travel if they were stimulated.

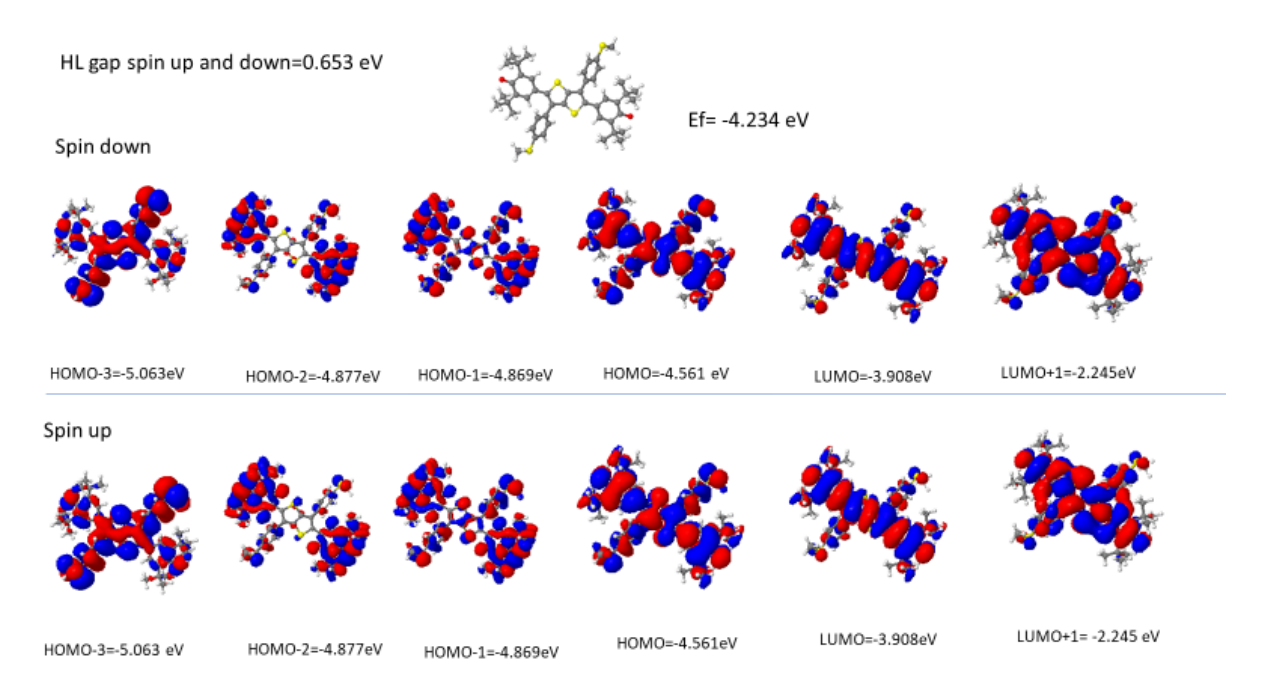


Figure 5.20: Frontier molecular orbitals of CQI-L-singlet studied molecule with its eigenvalues.

In both spin-up and down of the orbital ends the HOMOs and LUMOs have the opposite signs as shown in Figure 5.20, so the CQI is again predicted.

This Figure describes the electrical structure, focusing on the spin-dependent energy levels.

Spin splitting affects the distribution of electrons across energy levels, which affects material properties such as magnetism and conductivity.

The 0.653 eV gap between the spin-up and spin-down states suggests strong spin polarisation, which can influence electrical features such as magnetic moments and spintronic behaviour.

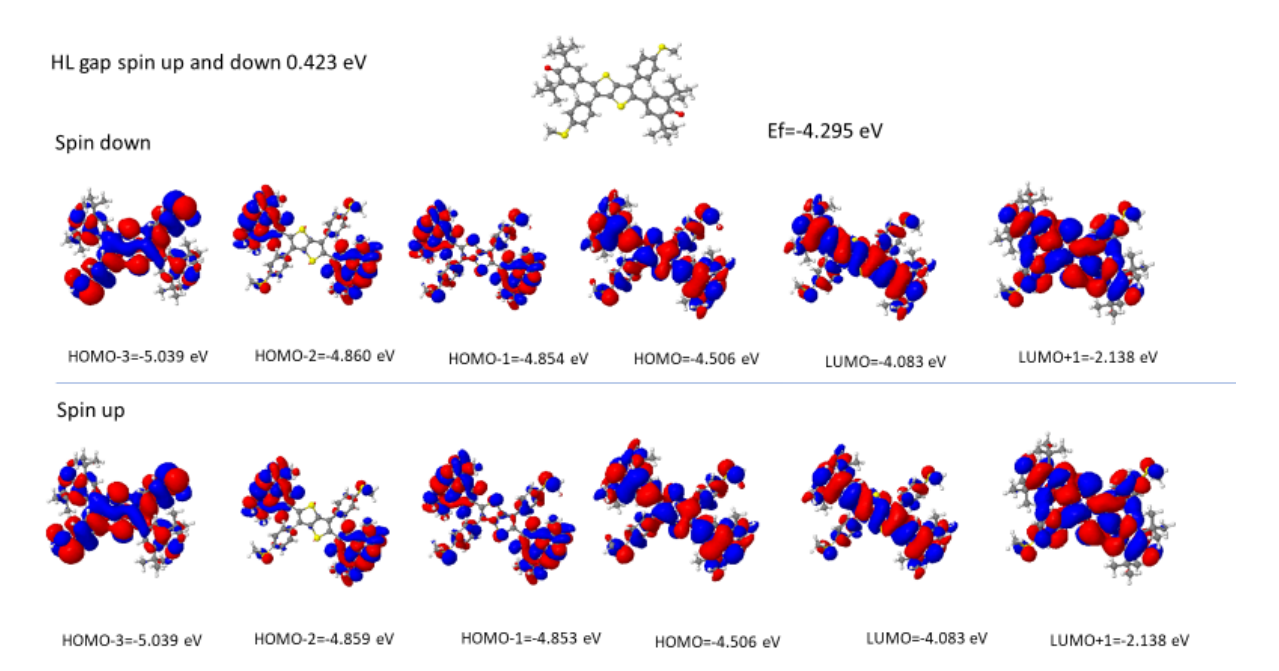


Figure 5.21: Frontier molecular orbitals of CQI-L-triplet studied molecule with its eigenvalues.

The orbital products of both spin-up and spin-down HOMOs and LUMOs have opposite signs as shown in Figure 5.21, so the CQI is predicted.

The figure shows the energy levels that correspond to the system's spin-up and spin-down states. It provides the energies of several molecular orbitals, particularly the HOMO (highest occupied molecular orbital) and LUMO (lowest unoccupied molecule orbital).

For spin-up, the LUMO is at -4.083 eV, and orbitals such as HOMO-1 and HOMO have energies of about -4.854 eV and -4.506 eV, respectively.

For spin-down, the energies of the corresponding orbitals, HOMO-3 and HOMO-2, are around -5.039 eV and -4.860 eV, respectively. The HL gap (~0.423 eV) between spin-up and spin-down states indicates spin polarisation in the system. This gap indicates that the two spin states are energetically separated, which influences the material's electrical and magnetic properties.

#### 5.5 Conclusion

In conclusion, the study shows that the creation of stable organic diradicals can lead to a large conductance enhancement in single-molecule junctions. As shown in Figures, 5.13, 5.15 and 5.17 a conductance increase of between 2 and 3 orders of magnitude can be expected upon removal of two hydrogen atoms. These results indicate that the ability to attach and detach hydrogen atoms leads to new strategy for high performance single-molecule switches with attractive on-off ratios. This gives new options for the development of advanced electrical devices, particularly in spintronics and molecular electronics, where distinctive features of radicals can be used for new applications. The stability of these radicals under ambient situations contributes to their potential for practical application in future electrical systems.

### 5.6. Bibliography

- [1] R. Frisenda, R. Gaudenzi, C. Franco, M. Mas-Torrent, C. Rovira, J. Veciana, I. Alcon, S. T. Bromley, E. Burzuri, and H. S. J. van der Zant, 'Kondo effect in a neutral and stable all organic radical single molecule break junction', Nano Lett, vol. 15, no. 5, pp. 3109–3114, May 2015, doi: 10.1021/acs.nanolett.5b00155.
- [2] F. Bejarano, I. J. Olavarria-Contreras, A. Droghetti, I. Rungger, A. Rudnev, D. Gutierrez M. Mas-Torrent, J. Veciana, H. S. J. van der Zant, C. Rovira, E. Burzuri, and N. Crivillers, 'Robust Organic Radical Molecular Junctions Using Acetylene Terminated Groups for C–Au Bond Formation', *J. Am. Chem. Soc.*, vol. 140, no. 5, pp. 1691–1696, Feb. 2018, doi: 10.1021/jacs.7b10019.
- [3] R. Hayakawa *M. Amin Karimi, J. Wolf, T. Huhn, M. Sebastian Zollner, C. Herrmann, and E. Scheer.*, 'Large Magnetoresistance in Single-Radical Molecular Junctions', *Nano Lett.*, vol. 16, no. 8, pp. 4960–4967, Aug. 2016, doi: 10.1021/acs.nanolett.6b01595.
- [4] S. Naghibi, S.Sangtarash, V. J. Kumar, J. Zhong Wu, M. M. Judd, X. Qiao, E. Gorenskaia, S. J. Higgins, N. Cox, R. J. Nichols, H. Sadeghi, P. J. Low, and A. Vezzoli, 'Redox-Addressable Single-Molecule Junctions Incorporating a Persistent Organic Radical', *Angew Chem Int Ed Engl*, vol. 61, no. 23, p. e202116985, Jun. 2022, doi: 10.1002/anie.202116985.
- [5] J. Liu, X. Zhao, Q. Al-Galiby, X. Huang, J. Zheng, J.Zheng, R. Li, C. Huang, Y.Yang, J. Shi, D. Zsolt Manrique, C. J. Lambert, M. R. Bryce, and W. Hong, 'Radical-Enhanced Charge Transport in Single-Molecule Phenothiazine Electrical Junctions', Angew Chem Int Ed Engl, vol. 56, no. 42, pp. 13061–13065, Oct. 2017, doi: 10.1002/anie.201707710.
- [6] N. Xin, J. Guan, C. Zhou, X. Chen, C. Gu, Y. Li, M. A. Ratner, A. Nitzan, J. Fraser Stoddart, and X. Guo, 'Concepts in the design and engineering of single-molecule electronic devices', Nature Reviews Physics, vol. 1, no. 3, pp. 211–230, Mar. 2019, doi: 10.1038/s42254-019-0022-x.
- [7] S. Zhen, J. Chuan Mao, L. Chen, S. Ding, W. Luo, X. Shun Zhou, A. Qin, Z. Zhao, and B. Zhong Tang, 'Remarkable Multichannel Conductance of Novel Single-Molecule Wires Built on Through-

- Space Conjugated Hexaphenylbenzene', *Nano Lett*, vol. 18, no. 7, pp. 4200–4205, Jul. 2018, doi: 10.1021/acs.nanolett.8b01082.
- [8] T. Hines, I. Díez-Pérez, H. Nakamura, T. Shimazaki, Y. Asai, and N. Tao, 'Controlling formation of single-molecule junctions by electrochemical reduction of diazonium terminal groups', *J Am Chem Soc*, vol. 135, no. 9, pp. 3319–3322, Mar. 2013, doi: 10.1021/ja3106434.
- [9] P. Shen, M. Huang, J. Qian, J. Li, S. Ding, X. Shun Zhou, B. Xu, Z. Zhao, B. Zhong Tang, ., 'Achieving Efficient Multichannel Conductance in Through-Space Conjugated Single-Molecule Parallel Circuits', *Angew Chem Int Ed Engl*, vol. 59, no. 11, pp. 4581–4588, Mar. 2020, doi: 10.1002/anie.202000061.
- [10] A. R. Rocha, V. M. García-Suárez, S. W. Bailey, C. J. Lambert, J. Ferrer, and S. Sanvito, 'Towards molecular spintronics', *Nat Mater*, vol. 4, no. 4, pp. 335–339, Apr. 2005, doi: 10.1038/nmat1349.
- [11] P. Gehring, J. K. Sowa, C. Hsu, and J. de Bruijckere, 'Complete mapping of the thermoelectric properties of a single molecule', *Nat Nanotechnol*, vol. 16, no. 4, pp. 426–430, Apr. 2021, doi: 10.1038/s41565-021-00859-7.
- [12] Y. Shen, G. Xue, Y. Dai, S. M. Quintero, H. Chen, D. Wang, F. Miao, F. Negri, Y. Zheng, and J. Casado, 'Normal & reversed spin mobility in a diradical by electron-vibration coupling', *Nat Commun*, vol. 12, no. 1, p. 6262, Oct. 2021, doi: 10.1038/s41467-021-26368-8.
- [13] 'Single-molecule calorimeter and free energy landscape | PNAS'. Accessed: Dec. 31, 2024. [Online]. Available: https://www.pnas.org/doi/10.1073/pnas.2104598118
- [14] J. Hurtado-Gallego, S. Sangtarash, R. Davidson, L. Rincon- Garcia, A. Daaoud, G. Rubio-Bollinger, C. J. Lambert, V. S. Oganesyan, M. R. bryce, N. Agrait, and H. Sadeghi, 'Thermoelectric Enhancement in Single Organic Radical Molecules', *Nano Lett*, vol. 22, no. 3, pp. 948–953, Feb. 2022, doi: 10.1021/acs.nanolett.1c03698.
- [15] G. Yzambart, L. Rincon-Garcia, A. A. Al-Jobory, A. K. Ismael, G. Rubio-Bollinger, C. J. Lambert, N. Agrait, and M. R. Bryce, 'Thermoelectric Properties of 2,7-Dipyridylfluorene

Derivatives in Single-Molecule Junctions', *J Phys Chem C Nanomater Interfaces*, vol. 122, no. 48, pp. 27198–27204, Dec. 2018, doi: 10.1021/acs.jpcc.8b08488.

[16] M. Baghernejad, C. Van Dyck, J. Bergfield, D. R. Levine, A. Gubicza, J. D. Tovar, M. Calame, P. Broekmann, and W. Hong, 'Quantum Interference Enhanced Chemical Responsivity in Single-Molecule Dithienoborepin Junctions', *Chemistry*, vol. 25, no. 66, pp. 15141–15146, Nov. 2019, doi: 10.1002/chem.201903315.

[17] C. Jia, A. Migliore, N. Xin, S. Huang, J. Wang, Q. Yang, S. Wang, H. Chen, D. Wang, B. feng, Z. Liu, G. Zhang, Da-Hui Qu, H. Tian, M. A. Ratner, H. Q. Xu, A. Nitzan, and X. Guo, 'Covalently bonded single-molecule junctions with stable and reversible photoswitched conductivity', *Science*, vol. 352, no. 6292, pp. 1443–1445, Jun. 2016, doi: 10.1126/science.aaf6298.

[18] J. Guan, C. Jia, Y. Li, Z. Liu, J. Wang, Z. Yang, C. gu, D. Su, K. N. Houk, D. Zhang, and X. Guo, 'Direct single-molecule dynamic detection of chemical reactions', *Sci Adv*, vol. 4, no. 2, p. eaar2177, Feb. 2018, doi: 10.1126/sciadv.aar2177.

[19] Z. Li, M. Smeu, M. A. Ratner, and E. Borguet, 'Effect of Anchoring Groups on Single Molecule Charge Transport through Porphyrins', *J. Phys. Chem. C*, vol. 117, no. 29, pp. 14890–14898, Jul. 2013, doi: 10.1021/jp309871d.

[20] Z. Yan, X. Li, Y. Li, C. Jia, Na. Xin, P. Li, L. Meng, M. Zhang, L. Chen, J. Yang, R. Wang, and X. Guo, 'Single-molecule field effect and conductance switching driven by electric field and proton transfer', *Sci Adv*, vol. 8, no. 12, p. eabm3541, Mar. 2022, doi: 10.1126/sciadv.abm3541.

[21] Y. Zang, E. Dean Fung, T. Fu, S. Ray, M. H. Garner, A. Borges, M. L. Steigerwald, S. Patil, G. Solomon, and L. Venkatarman, 'Voltage-Induced Single-Molecule Junction Planarization', *Nano Lett*, vol. 21, no. 1, pp. 673–679, Jan. 2021, doi: 10.1021/acs.nanolett.0c04260.

[22] L. Yuan, L. Jiang, and C. A. Nijhuis, 'The Drive Force of Electrical Breakdown of Large-Area Molecular Tunnel Junctions', *Advanced Functional Materials*, vol. 28, no. 28, p. 1801710, 2018, doi: 10.1002/adfm.201801710.

- [23] Y. Guo, S. Ding, N. Zhang, Z. Xu, S. Wu, J. Hu, Q. Xiang, Z. Yang Li, X. Chen, S. Sato, J. Wu, and Z. Sun, 'π-Extended Doublet Open-Shell Graphene Fragments Exhibiting One-Dimensional Chain Stacking', *J Am Chem Soc*, vol. 144, no. 5, pp. 2095–2100, Feb. 2022, doi: 10.1021/jacs.1c12854.
- [24] Y. Ji, L. Long, and Y. Zheng, 'Recent advances of stable Blatter radicals: synthesis, properties and applications', *Mater. Chem. Front.*, vol. 4, no. 12, pp. 3433–3443, Nov. 2020, doi: 10.1039/D0QM00122H.
- [25] X. Hu, W. Wang, D. Wang, and Y. Zheng, 'The electronic applications of stable diradicaloids: present and future', *J. Mater. Chem. C*, vol. 6, no. 42, pp. 11232–11242, Nov. 2018, doi: 10.1039/C8TC04484H.
- [26] H. Zhang, F. Miao, X. Liu, D. Wang, and Y. Zheng, 'Recent Advances of Stable Phenoxyl Diradicals', *Chemical Research in Chinese Universities*, vol. 39, no. 2, pp. 170–175, Apr. 2023, doi: 10.1007/s40242-023-3012-6.
- [27] J. Z. Low, G. Kladnik, L. L. Patera, S. Sokolov, G. Lovat, E. Kumarasamy, J. Repp, L. M. Campos, D. Cvetko, A. Morgante, and L. Venkataraman, 'The Environment-Dependent Behavior of the Blatter Radical at the Metal-Molecule Interface', *Nano Lett*, vol. 19, no. 4, pp. 2543–2548, Apr. 2019, doi: 10.1021/acs.nanolett.9b00275.
- [28] M. Mas-Torrent, N. Crivillers, C. Rovira, and J. Veciana, 'Attaching persistent organic free radicals to surfaces: how and why', *Chem Rev*, vol. 112, no. 4, pp. 2506–2527, Apr. 2012, doi: 10.1021/cr200233g.
- [29] X. Guo, M. Baumgarten, and K. Müllen, 'Designing π-conjugated polymers for organic electronics', *Progress in Polymer Science*, vol. 38, no. 12, pp. 1832–1908, Dec. 2013, doi: 10.1016/j.progpolymsci.2013.09.005.
- [30] W. Y. Wong 'Metallated molecular materials of fluorene derivatives and their analogues', *Coordination Chemistry Reviews*, vol. 249, no. 9–10, pp. 971–997, May 2005, doi: 10.1016/j.ccr.2004.10.007.

- [31] Y. Tian, K. Uchida, H. Kurata, Y. Hirao, T. Nishiuchi, and T. Kubo, 'Design and synthesis of new stable fluorenyl-based radicals', *J Am Chem Soc*, vol. 136, no. 36, pp. 12784–12793, Sep. 2014, doi: 10.1021/ja507005c.
- [32] X. Lu, S. Lee, J. Oh. Kim, T. Y. Gopalakrishna, H. Phan, T. Seng Herng, Z. Lim, Z. Zeng, J. Ding, D. Kim, and J. Wu, 'Stable 3,6-Linked Fluorenyl Radical Oligomers with Intramolecular Antiferromagnetic Coupling and Polyradical Characters', *J Am Chem Soc*, vol. 138, no. 39, pp. 13048–13058, Oct. 2016, doi: 10.1021/jacs.6b08138.
- [33] Z. Zeng Y. Mo Sung N. Bao, D. Tan, R. Lee, J. L. Zafra, B. Sun Lee, M. Ishida, J. Ding, J. T. Lopez, Navarrete, Y. Li, W. Zeng, D. Kim, K. Wei Huang, R. D. Webster, J. Casado, and J. Wu, 'Stable tetrabenzo-Chichibabin's hydrocarbons: tunable ground state and unusual transition between their closed-shell and open-shell resonance forms', J Am Chem Soc, vol. 134, no. 35, pp. 14513–14525, Sep. 2012, doi: 10.1021/ja3050579.
- [34] A. Alanazy, E. Leary, T. Kobatake, S. Sangtarash, M. T. Gonzalez, H. W. Jiang, G. R. Bollinger, N. Agrait, H. Sadeghi, I. Grace, S. J. Higgins, H. L. Anderson, R. J. Nichols, and C. J. Lambert, 'Cross-conjugation increases the conductance of meta-connected fluorenones', *Nanoscale*, vol. 11, no. 29, pp. 13720–13724, Jul. 2019, doi: 10.1039/C9NR01235D.
- [35] N. R. Claughton, M. Leadbeater, and C. J. Lambert, 'Theory of Andreev resonances in quantum dots', *J. Phys.: Condens. Matter*, vol. 7, no. 46, p. 8757, Nov. 1995, doi: 10.1088/0953-8984/7/46/007.

# Chapter 6

## **Conclusion and Future Work**

#### 6.1 Conclusion

This thesis has focused on the following chapters:

Chapter 1 provides a general overview of molecular electronics, thermoelectricity, and the thesis outline. Chapter 2 provides general ideas of DFT code SIESTA, which is employed to all the electronic structure computations in this thesis. In the stimulation study, I extracted and relaxed the Hamiltonian of an isolated molecule before connecting it to metallic electrodes to calculate transport properties. Chapter 3 covers single-particle transport theory, which includes the Landau formula, thermoelectric coefficients, and scattering theory. Chapter 4 This research describes a dynamic molecular switch capable of simulating synaptic behavior and completing complicated computational tasks, paving the path for future advances in neuromorphic computing and adaptive electronics.

Chapter 5 in this study indicates that stable organic radicals improve single-molecule conductivity. The results show that the unique properties of diradicals can be exploited to create new electrical switches with attractive on-off conductance ratio of between 2 and 3 orders of magnitude. These radicals are stable under ambient conditions, making them suitable for future electrical systems.

#### **6.2 Future Work**

The research in chapter 4 suggests several recommendations for future work, one of which is to investigate the possibility of incorporating these dynamic molecular switches into more sophisticated circuits and systems to explore their potential in neuromorphic computing further. Additionally, I can focus on improving the performance and stability of these switches, along with examining their scalability for actual applications in electronic devices. Future studies could include the creation of new substances or configurations to improve the efficiency and efficacy of molecular switches in replicating synaptic behaviour. Chapter 5: The suggested future work in this chapter includes additional research on the stability and performance of stable organic radicals in diverse environments, especially under ambient circumstances. Develop stable radicals that can keep their properties outside of controlled laboratory environments. The possibility of investigating various molecular configurations and substituents to maximise charge transport characteristics and improve the performance of single-molecule electrical devices, including spintronics and thermoelectric applications. For both the HATNA molecule in chapter 4 and the diradicals in chapter 5, the on-off conductance ratio is sensitive to the position of the Fermi energy and therefore it would be of interest to vary  $E_F$ , either by change the anchor groups, (to eg thiol) or by varying the electrode materials. In the literature, a wide range of electrode materials have been explored, including graphene [12], silicene [13] and platinum [14]. For the purpose of increasing on/off conductance ratios, it may also be of interest to consider using one superconducting and one normal-metal electrode, so that charge transport is mediated by Andreev reflection [15-17]. This may be particularly fruitful, because recent studies have shown that CQ and DQI features persist and on-off ratios are enhanced by the presence of a superconducting electrode [18,19]. Finally, as well as studying the role of hydrogenation on Seebeck coefficients, it would be of interest to determine if such changes modify the thermal

conductance of diradical and easily reduced molecules such as HATNA. Recently, single-molecule thermal conductances have been computed by adapting techniques used to model phonon transport in disordered wires [20] and shown to be in excellent agreement with experimental thermal conductance measurements [21]. Investigating the effects of external stimuli such as light or magnetic fields on the molecules, creating molecules with various conductance states to improve data storage, evaluating the molecules' long-term stability, and researching the effects of environment and temperature on performance. Additionally, studying spin and thermoelectric properties, enhancing production techniques for scalability, and investigating integration with materials like graphene can all contribute to the advancement of useful applications.

## 6.3. Bibliography

- [1] Y. van de Burgt, A. Melianas, S. T. Keene, G. Malliaras, and A. Salleo, 'Organic electronics for neuromorphic computing', *Nat Electron*, vol. 1, no. 7, pp. 386–397, Jul. 2018, doi: 10.1038/s41928-018-0103-3.
- [2] J. Zhu, T. Zhang, Y. Yang, and R. Huang, 'A comprehensive review on emerging artificial neuromorphic devices', *Applied Physics Reviews*, vol. 7, no. 1, p. 011312, Feb. 2020, doi: 10.1063/1.5118217.
- [3] N. K. Upadhyay, H. Jiang, Z. Wang, S. Asapu, Q. Xia, and J. Joshua Yang, 'Emerging Memory Devices for Neuromorphic Computing', *Advanced Materials Technologies*, vol. 4, no. 4, p. 1800589, Apr. 2019, doi: 10.1002/admt.201800589.
- [4] T. Chen, J. Van Gelder, B. Van de Ven, S. V. Amitonov, B. de Wilde, H. C. Ruiz Euler, H. Broersma, P. A. Bobbert, F. A. Zwanenburg, and W. G. Van der Wiel, 'Classification with a disordered dopant-atom network in silicon', *Nature*, vol. 577, no. 7790, pp. 341–345, Jan. 2020, doi: 10.1038/s41586-019-1901-0.
- [5] S. T. Keene, C. Lubrano, S. Kazemzadeh, A. Melianas, Y. Tuchman, G. Polino, P. Scognamiglio, L. Cina, A. Salleo, Y. B. van de Burgt, and F. Santoro, 'A biohybrid synapse with neurotransmitter-mediated plasticity', *Nat. Mater.*, vol. 19, no. 9, pp. 969–973, Sep. 2020, doi: 10.1038/s41563-020-0703-y.
- [6] R. Frisenda, R. Gaudenzi, C. Franco, M. Mas-Torrent, C. Rovira, J. Veciana, I Alcon, S. T. Bromley, E. Burzuri, and H. S. J. van der Zant, 'Kondo effect in a neutral and stable all organic radical single molecule break junction', *Nano Lett*, vol. 15, no. 5, pp. 3109–3114, May 2015, doi: 10.1021/acs.nanolett.5b00155.
- [7] F. Bejarano, I. J. Olavarria,-Contreras, A. Droghetti, I. Rungger, A. Rudnev, D. Gutierrez, M. Mas-Torrent, J. Veciana, H. S. J. Zant, and C. Rovira, 'Robust Organic Radical Molecular Junctions

- Using Acetylene Terminated Groups for C-Au Bond Formation', *J. Am. Chem. Soc.*, vol. 140, no. 5, pp. 1691–1696, Feb. 2018, doi: 10.1021/jacs.7b10019.
- [8] R. Hayakawa, M. A. Karimi, J. Wolf, T. Huhn, M. S. Zollner, C. herrmann, and E. Scheer, 'Large Magnetoresistance in Single-Radical Molecular Junctions', *Nano Lett.*, vol. 16, no. 8, pp. 4960–4967, Aug. 2016, doi: 10.1021/acs.nanolett.6b01595.
- [9] S. Naghibi, S. Sangtarash, V. J. Kumar, J. Z.Wu, M. M. Judd, X. Qiao, E. Gorenskaia, S. J. Higgins, N. Cox, and R. J. Nichols, 'Redox-Addressable Single-Molecule Junctions Incorporating a Persistent Organic Radical', *Angew Chem Int Ed Engl*, vol. 61, no. 23, p. e202116985, Jun. 2022, doi: 10.1002/anie.202116985.
- [10] J. Liu, X. Zhao, Q. Al-Galiby, X. Huang, J. Zheng, R. Li, C. Huang, Y, Yang, J. Shi, and D. Z. Manrique 'Radical-Enhanced Charge Transport in Single-Molecule Phenothiazine Electrical Junctions', *Angew Chem Int Ed Engl*, vol. 56, no. 42, pp. 13061–13065, Oct. 2017, doi: 10.1002/anie.201707710.
- [11] N. Xin, J. Guan, C. Zhou, X.Chen, C.Gu, Y. Li, M. A. Ratner, A. Nitzan, J. F.Stoddart, and X. Guo, 'Concepts in the design and engineering of single-molecule electronic devices', *Nature Reviews Physics*, vol. 1, no. 3, pp. 211–230, Mar. 2019, doi: 10.1038/s42254-019-0022-x.
- [12] X.H. Zheng, G.R. Zhang, Z. Zeng, V.M. García-Suárez, C.J. Lambert, 'Effects of antidots on the transport properties of graphene nanoribbons,' Physical Review B—Condensed Matter and Materials Physics 80 (7), 075413, 2009
- [13] H. Sadeghi, S. Bailey, C.J. Lambert, 'Silicene-based DNA nucleobase sensing,' Applied Physics Letters 104 (10) 67, 2014
- [14] V.M. García-Suárez, A.R. Rocha, S.W. Bailey, C.J. Lambert, S. Sanvito, J. Ferrer, 'Conductance oscillations in zigzag platinum chains,' Physical Review Letters 95 (25), 256804, 2005
- [15] N.R. Claughton, M. Leadbeater, C.J. Lambert, 'Theory of Andreev resonances in quantum dots.' Journal of Physics: Condensed Matter 7 (46), 8757, 1995

- [16] C.J. Lambert, 'Quantum Interference from superconducting islands in a mesoscopic solid,' J. Phys. Condens. Matter 5, 707, 1993
- [17] C.J. Lambert, R. Raimondi, V. Sweeney, A.F. Volkov, 'Boundary conditions for quasiclassical equations in the theory of superconductivity,' Physical Review B 55 (9), 6015, 1997
- [18] N.L. Plaszkó, P. Rakyta, J. Cserti, A. Kormányos and C.J. Lambert, 'Quantum interference and non-equilibrium Josephson current in molecular Andreev interferometers,' Nanomaterials 10 1033, 2020
- [19] P. Rakyta, A. Alanazy, A. Kormányos, Z. Tajkov, G. Kukucska, J. Koltai, S. Sangtarash, H. Sadeghi, J. Cserti, and C.J. Lambert, 'Magic number theory of superconducting proximity effects and Wigner delay times in graphene-like molecules,' J. Phys. Chem C. 123 6812, 2019
- [20] G. Fagas, A.G. Kozorezov, C.J. Lambert, J.K. Wigmore, A. Peacock, A. Poelaert, R. den Hartog, 'Lattice dynamics of a disordered solid-solid interface,' Physical Review B 60 (9), 6459, 1999
- [21] N. Mosso, H. Sadeghi, A. Gemma, S. Sangtarash, U. Drechsler, C.J. Lambert, B. Gotsmann, 'Thermal transport through single-molecule junctions,' Nano letters 19 (11), 7614-7622, 2019